Eur. Phys. J. A (2024) 60:193
https://doi.org/10.1140/epja/s10050-024-01403-6

THE EUROPEAN PHYSICAL JOURNAL A

Review

Total reaction cross section of light stable and exotic nuclei on lead at energies around the Coulomb barrier

Peter Mohr[a]

HUN-REN Institute for Nuclear Research (ATOMKI), P.O.Box 51, Debrecen 4001, Hungary

Received: 26 April 2024 / Accepted: 6 August 2024

Communicated by Maria Borge

Abstract The present review studies total reaction cross sections from elastic scattering angular distributions of light stable and exotic projectiles ($2 \le Z_P \le 10$, $4 \le A_P \le 24$) on ^{208}Pb at energies around the Coulomb barrier. From the overall about 200 data it is found that the widely accepted simple grouping of the derived reduced cross sections into three categories—tightly bound, weakly bound, and exotic halo projectiles—is too simplistic and does not fully reflect the range of the experimental data. Furthermore, the energy dependence of the reduced cross sections shows unexpected properties which were hitherto only sparsely considered.

1 Introduction

The total reaction cross section $\sigma_{\rm reac}$ is an essential quantity in the interaction of nuclei. At energies above the Coulomb barrier, $\sigma_{\rm reac}$ is governed by the sizes of the projectile and the target nucleus; their radii scale approximately with the cubic root of their mass numbers $A_P^{1/3}$ and $A_T^{1/3}$. Towards lower energies, $\sigma_{\rm reac}$ decreases dramatically for charged projectiles and targets because of the decreasing tunneling probability through the Coulomb barrier.

A comparison of $\sigma_{\rm reac}$ for various combinations of projectiles and targets at different energies requires a proper scaling procedure. The present study applies the simple reduction procedure using reduced cross sections $\sigma_{\rm red}$ vs. reduced energies $E_{\rm red}$ which was first suggested by Gomes et al. [1] and later used in many subsequent papers. This choice will be motivated in Sect. 2.

Several experimental techniques have been established to measure the total reaction cross section $\sigma_{\rm reac}$. At higher energies $\sigma_{\rm reac}$ can be derived directly from the transmission through relatively thick targets, see e.g. [2]. For relatively light projectiles and moderate energies, $\sigma_{\rm reac}$ can be determined by summing all partial cross sections. This technique was recently applied to ^{64}Zn + α for energies below 20 MeV where $\sigma_{\rm reac}$ was essentially given by the sum of the (α,n), (α,p), (α,γ), and (α,α') cross sections [3,4]. However, a huge number of open channels contributes to $\sigma_{\rm reac}$ for heavier projectiles and targets which are complete and incomplete fusion, one- or few-nucleon transfer (often two-neutron transfer), breakup, and inelastic scattering. In this case it is at least very difficult or practically almost impossible to measure and sum up all partial cross sections to obtain $\sigma_{\rm reac}$. For this case, $\sigma_{\rm reac}$ is usually derived from elastic scattering. Here the angular distribution depends on the reflexion coefficients η_L and the phase shifts δ_L; the total reaction cross section $\sigma_{\rm reac}$ depends only on the η_L, but is independent of the δ_L.

The latter technique will be applied in the following for the determination of $\sigma_{\rm reac}$ for the interaction of ^{4,6,8}He, ^{6,7,8,9,11}Li, ^{7,9,10,11}Be, ^{8,11}B, ^{10,12,13,15}C, ^{14}N, ^{16,17,18}O, ^{17,19}F, and ^{17,20,22,24}Ne projectiles with ^{208}Pb as target at energies around the Coulomb barrier. Overall, more than 200 values for $\sigma_{\rm reac}$ were determined. The presentation of the data as reduced cross sections $\sigma_{\rm red}$ vs. reduced energies $E_{\rm red}$ will show that larger $\sigma_{\rm red}$ are found for weakly bound systems. In addition to this well-known general phenomenon, further details on the energy dependence of $\sigma_{\rm red}$ can be found from this systematic study. Finally, unexpected differences between the $\sigma_{\rm red}$ for different tightly bound projectiles like the α-particle, ^{12}C, and ^{16}O are identified for the first time.

It is generally accepted that the data for $\sigma_{\rm red}$ are grouped into three categories, namely tightly bound projectiles, weakly bound projectiles, and exotic projectiles with halo properties, see e.g. [5–7]. The present study shows that such a simple grouping does not fully reflect the wide range of observed $\sigma_{\rm red}$, and in particular the energy dependence of $\sigma_{\rm red}$ towards low energies deserves special attention.

The present study focuses on data for the target nucleus ^{208}Pb. From the experimental side, a huge number of angular

[a] e-mail: mohr@atomki.hu (corresponding author)

Published online: 23 September 2024

distributions is available for stable and also unstable projectiles which is a basic prerequisite for a systematic analysis. The study of total reaction cross sections for various projectiles on the the same ^{208}Pb target facilitates the discussion of the results because the target properties are identical in all cases under study. At the end of the present work, a brief comparison to results from a light target nucleus (^{12}C) is added. Future work should complement the present analysis with data for intermediate mass targets like ^{64}Ni, ^{64}Zn, and ^{90}Zr. This should shed further light on the underlying reaction mechanisms where larger contributions from Coulomb breakup of exotic projectiles should be found for high-Z targets like ^{208}Pb whereas nuclear contributions should dominate for low-Z targets.

The paper is organized as follows. After some general remarks in Sect. 2, the determination of the total reaction cross section $\sigma_{\rm reac}$ from angular distributions of elastic scattering and the related uncertainties are discussed in Sect. 3. The available elastic scattering data for ^{4,6,8}He, ^{6,7,8,9,11}Li, ^{7,9,10,11}Be, ^{8,11}B, ^{10,12,13,15}C, ^{14}N, ^{16,17,18}O, ^{17,19}F, and ^{17,20,22,24}Ne and the total reaction cross sections $\sigma_{\rm reac}$ are presented in subsections of Sect. 4. The data for ^{208}Pb + α, summarized in Sect. 4.1, will be used as a reference for $\sigma_{\rm red}$. For comparison to heavier projectiles, some data for ^{40,48}Ca and ^{48}Ti will be added in Sects. 4.29, 4.30, and 4.31. The results will be discussed in Sect. 5, including a brief outlook into data from X + ^{12}C elastic scattering in addition to the main focus on X + ^{208}Pb in the present study. A summary and final conclusions are given at the end in Sect. 6.

2 General remarks

2.1 Reduction schemes

2.1.1 Geometrical reduction scheme

A simple reduction scheme for the comparison of heavy-ion induced reactions, often called geometrical reduction, has been suggested by Gomes et al. [1]. The so-called reduced cross sections $\sigma_{\rm red}$ and reduced energies $E_{\rm red}$ are defined by:

$$E_{\rm red} = \frac{\left(A_P^{1/3} + A_T^{1/3}\right) E_{\rm c.m.}}{Z_P Z_T} \tag{1}$$

$$\sigma_{\rm red} = \frac{\sigma_{\rm reac}}{\left(A_P^{1/3} + A_T^{1/3}\right)^2} \tag{2}$$

The reduced energy $E_{\rm red}$ takes into account the different heights of the Coulomb barrier in the systems under consideration. The factor $Z_P Z_T/(A_P^{1/3} + A_T^{1/3})$, which appears inverse in Eq. (1), reflects the height of the Coulomb potential at the radius $R_{\rm geom}$ = 1.0 fm × $(A_P^{1/3} + A_T^{1/3})$. The reduced reaction cross section $\sigma_{\rm red}$ scales the measured total reaction cross section $\sigma_{\rm reac}$ according to the geometrical size $A_{\rm geom}$ of the projectile-plus-target system which is given by $A_{\rm geom} = \pi R_{\rm geom}^2$. Note that a more realistic choice of R_0 = 1.2 fm or 1.3 fm instead of R_0 = 1.0 fm in the definitions of $R_{\rm geom}$ and $A_{\rm geom}$ would lead only to scaling factors for all reduced energies $E_{\rm red}$ and $\sigma_{\rm red}$ but not affect the interpretation of the $\sigma_{\rm red}$ vs. $E_{\rm red}$ systematics.

The main advantage of this simple geometrical reduction scheme is its trivial dependence on few parameters Z_P, Z_T, A_P, A_T, and $E_{\rm c.m.}$. Extraordinary properties of the colliding nuclei (like larger radii, deviating from the usual $A^{1/3}$ dependence) become directly visible in enhanced $\sigma_{\rm red}$. Taking into account more realistic nuclear radii for individual nuclei in the definitions of Eqs. (1) and (2) (e.g., from the measurement of interaction radii or from charge density distributions from electron scattering) would not be helpful because this would wash out deviations from the standard behavior of the $\sigma_{\rm red}$ vs. $E_{\rm red}$ systematics. Consequently, the present study uses only the simple reduction scheme of $\sigma_{\rm red}$ vs. $E_{\rm red}$ as defined in Eqs. (1) and (2). Washing-out effects will be discussed further in the following Sect. 2.1.3.

It was already pointed out in the initial paper [1] that the data from various systems can be assigned to three groups, namely (*i*) data for tightly bound projectiles (e.g., ^{16}O) with regular $\sigma_{\rm red}$, (*ii*) data for weakly bound projectiles (e.g., ^{6,7}Li and ^{9}Be) with moderately enhanced $\sigma_{\rm red}$, and (*iii*) data for exotic nuclei like ^{6}He with its neutron halo with significantly enhanced $\sigma_{\rm red}$. This general grouping was essentially confirmed in many subsequent studies, see e.g. [8,9] for projectiles with halo properties or [10,11] for many α-induced reactions. For a definition of halo nuclei and the resulting experimental observables, see e.g. [12,13].

2.1.2 Reduced critical interaction distance

Another purely geometrical method for the comparison of different systems is the so-called reduced critical interaction distance. The idea goes back to early work by Christensen et al. [14] and was discussed recently in detail by Guimarães et al. [15]. In this semi-classical approach, the closest interaction distance d_I is derived from a plot of the Rutherford-normalized differential cross section vs. the closest distance d on a Rutherford trajectory. d_I is typically defined as that distance d where the deviation from Rutherford exceeds 2% (but also slightly different definitions have been used [16]).

For comparison of different systems, the closest interaction distance d_I is reduced to $d_{I,\rm red} = d_I/(A_P^{1/3} + A_T^{1/3})$; this is a similar idea as for the reduced cross sections $\sigma_{\rm red}$. It is found that the reduced closest interaction distance $d_{I,\rm red}$ is larger for weakly bound projectiles and dramatically enhanced for ^{11}Li, whereas for tightly bound projectiles almost identical values are found (see Fig. 8 of [15]). The results and interpretation from this $d_{I,\rm red}$ approach are

close to the findings from the $\sigma_{\rm red}$ vs. $E_{\rm red}$ systematics; see also the discussion in Sect. 5.

2.1.3 Wong-type approaches

The widely used Wong formula for the total cross section is based on the approximation of the barrier by an inverse Gaussian potential with a barrier height E_L and curvature $\hbar\omega_L$ at radius R_L for the L-th partial wave [17]. It is pointed out in [17] that the L dependence of R_L and $\hbar\omega_L$ is minor. Using the approximations $R_L \approx R_0$ and $\hbar\omega_L \approx \hbar\omega_0$, finally the total reaction cross section is given analytically as a function of the incoming energy E and the s-wave parameters for the barrier height E_0, radius R_0, and curvature $\hbar\omega_0$ of the barrier. It is found in [17] that this analytical formula is able to reproduce experimental data very well.

On the one hand, this Wong-type approach contains more physics than the simple geometrical approach in Sect. 2.1.1. This allows a reliable prediction of the total reaction cross section if reasonable parameters are used for E_0, R_0, and $\hbar\omega_0$. On the other hand, a reduction of experimental cross sections by normalization to predictions from the Wong formula depends on the choice of the parameters E_0, R_0, and $\hbar\omega_0$; the better the choice for these parameters, the better the predictions from the Wong formula, and small deviations of the total cross section from the Wong prediction cannot be interpreted as a signature for extraordinary behavior of the colliding nuclei. It is also already pointed out in [1] that such reduction schemes have a trend to wash out enhanced cross sections for halo nuclei (see e.g. their Fig. 2) because for such nuclei R_0 is increased and E_0 is reduced.

The standard Wong approach from [17] was later improved by Canto [18,19] by the introduction of a so-called universal fusion function (UFF). This leads to an improved description of experimental reaction cross sections, but the above arguments on the washing-out of extraordinary behavior persist.

2.2 Practical procedure

The present study applies the following strategy for the determination of the total reaction cross section $\sigma_{\rm reac}$ from the angular distribution of elastic scattering. Further explanations can also be found in the next Sect. 3 where some examples are given in detail.

In almost all systems under study, the measured angular distributions were analyzed using the optical model (OM). Unfortunately, it is not common practice to provide the result for $\sigma_{\rm reac}$ from the OM fit; only in about half of the systems under study, the derived $\sigma_{\rm reac}$ are given in the original papers. In these cases the values from the original papers are used in present work.

If $\sigma_{\rm reac}$ is not given in the original studies, I tried to repeat the original OM calculations using the parameters of the OM potentials from the original papers. For simple Woods-Saxon potentials, this can be done without major problems, and $\sigma_{\rm reac}$ can be re-calculated. Such calculations were verified by comparison to the shown results in the original papers. In most cases good agreement was found, but in few cases it was not possible to exactly reproduce the original calculations. These differences may result from different OM codes, from the given (probably) rounded values of the OM parameters, from missing information on the chosen Coulomb radius, and from technical details of the OM calculations like the maximum integration radius, integration step width, and maximum angular momentum. In some cases folding potentials were used in the original papers. Here the available information is often insufficient to exactly reproduce the original calculations.

When it was not possible to re-calculate the resulting $\sigma_{\rm reac}$ from the OM fits of the original papers, I tried to re-fit the angular distributions. As discussed in the following Sect. 3, this requires the original data as a numerical table, including the original experimental uncertainties. As the availability of such high-quality data is limited, experimental databases like EXFOR [20,21] or NRV [22] often re-digitize the data from published figures. Using such low-quality data leads to additional uncertainties for the derived $\sigma_{\rm reac}$ which are difficult to quantify. Furthermore, often the experimental uncertainties are not re-digitized because the quality of the figures does not allow to do this with sufficient reliability. In such cases assumptions on the experimental uncertainties have to be made.

3 Angular distributions of elastic scattering and total reaction cross section $\sigma_{\rm reac}$

A partial wave decomposition of the angular distribution of the differential cross section $(d\sigma/d\Omega)(\vartheta)$ shows that $(d\sigma/d\Omega)(\vartheta)$ depends on the real reflexion coefficients η_L and the real phase shifts δ_L where the complex S-matrix elements are given by $S_L = \eta_L \times \exp(2i\delta_L)$. The total reaction cross section $\sigma_{\rm reac}$ depends only on the reflexion coefficients η_L, but is independent of the phase shifts δ_L. $\sigma_{\rm reac}$ is given by

$$\sigma_{\rm reac} = \sum_L \sigma_L = \frac{\pi}{k^2} \sum_L (2L+1)\,(1-\eta_L^2) \tag{3}$$

where $k = \sqrt{2\mu E_{\rm c.m.}}/\hbar$ is the wave number, and $E_{\rm c.m.}$ is the energy in the center-of-mass (c.m.) system. σ_L is the contribution of the L-th partial wave to the total reaction cross section $\sigma_{\rm reac}$.

At energies above the Coulomb barrier, the η_L for small angular momenta L (corresponding to central collisions in a semi-classical view) are very small, thus leading to σ_L close

to its maximum value $\sigma_{L,\max} = \frac{\pi}{k^2} \times (2\,L + 1)$. This corresponds to full absorption of the incoming partial waves with small angular momentum and tiny elastic cross sections at backward angles. For large angular momenta L (corresponding to large impact parameters in a semi-classical view) the η_L approach unity and thus $\sigma_L \approx 0$; i.e., these partial waves are not absorbed but contribute to the Rutherford cross section at forward angles.

At energies far below the Coulomb barrier, all η_L remain relatively close to unity, and $\sigma_{\rm reac}$ is thus much smaller than above the Coulomb barrier. In a semi-classical view, even in central collisions the incoming particles are not able to pass the Coulomb barrier. As a consequence, the elastic scattering cross section approaches the Rutherford cross section also at backward angles, and the total reaction cross section $\sigma_{\rm reac}$ becomes much smaller.

Depending on the energy and mass of the interacting nuclei, the above sum in Eq. (3) has to be calculated up to angular momenta of more than $L_{\max} \approx 100$. For lighter projectiles around the Coulomb barrier, lower $L_{\max} \approx 30$–50 are sufficient. Thus, a model-independent determination of all η_L and δ_L from an angular distribution in a phase-shift fit is possible only in very limited cases where precise data over the full angular range with a sufficiently huge number of data points are available. Some examples will be provided below, see Sects. 3.1 and 3.2.

Instead of a full phase shift analysis, the angular distribution of elastic scattering is typically fitted using the OM with an appropriate nucleus-nucleus optical model potential (OMP). The parameters of the OMP are adjusted to the experimental data by a χ^2-fit. Unfortunately, such fits often lead to ambiguities for the resulting OMP. This leads to uncertainties in the derived $\sigma_{\rm reac}$ which are difficult to estimate. In practice, most papers simply report the $\sigma_{\rm reac}$ from their best fit without any uncertainty. Sometimes a range of derived $\sigma_{\rm reac}$ is given which results from the variation of the underlying OMP parameters in a reasonable range. In such cases I use the average of the given numbers as $\sigma_{\rm reac}$, and the scatter of the data is taken as uncertainty.

It should be noted that this uncertainty is not the full uncertainty for $\sigma_{\rm reac}$ because all OM fits are performed in the limited model space of the OM which results from the shape of the chosen OMP parametrization, whereas a phase shift fit should allow a model-independent determination of $\sigma_{\rm reac}$. However, as already stated above, such phase shift fits require precise scattering data with well-defined experimental uncertainties. Some illustrative examples for the determination of $\sigma_{\rm reac}$ from different approaches will be given in the following.

In principle, the limitations of the model space in the OM from the chosen parametrization of the OMP can be avoided by a so-called model-independent OMP. Technically, this is often obtained by adding a series of Fourier-Bessel (FB) or Laguerre-Gaussian (LG) functions to a reasonably chosen underlying standard Woods-Saxon potential; see e.g. [23,24]. However, if a fully model-independent analysis shall be achieved, the number of FB or LG functions must be very high, thus leading to the same problems as explained above for the fully model-independent phase shift analysis.

Typical uncertainties of an elastic scattering experiment are composed of three major contributions. As usual, all data points have independent statistical uncertainties. Individual systematic uncertainties for each data point result from accuracy and reproducibility of the experimental detector angle. Furthermore, there is a common systematic uncertainty for all data points from a possible offset of the angular scale relative to the beam axis, typically of the order of 0.1°, which may lead to a significant contribution to the total uncertainty at forward angles because of the steep increase of the Rutherford cross section towards small angles. (Under poor beam conditions, this offset between beam axis and detector angle may even change during the experiment.) Finally, there is a common systematic uncertainty for all data points from the normalization which results from the uncertainties of the beam current integration, target thickness, and solid angle of the detector(s). This overall common systematic uncertainty is typically of the order of 5–15%. In practice, this uncertainty is reduced to about 1–2% by a normalization to the Rutherford cross section at most forward angles. It has to be mentioned that this requires a very careful measurement at very forward angles because of the steep Rutherford cross section, often also requiring a reliable deadtime correction for the high count rates in forward directions.

This complicated situation for the experimental uncertainties often leads to a presentation of experimental scattering data with a statement "the error bars include statistical uncertainties only", and not much information is provided for the other uncertainties. Obviously, such purely statistical uncertainties will be inappropriate for a phase shift fit or an OM fit.

In the next Sects. 3.1, 3.2, 3.3, and 3.4, some selected examples will be discussed in detail to illustrate the typical uncertainties of the total reaction cross sections $\sigma_{\rm reac}$ which result of the derivation from elastic scattering angular distributions. From the examples in the following paragraphs it will become clear that typical uncertainties for $\sigma_{\rm reac}$ are of the order of a few per cent at energies above the Coulomb barrier. At energies far below the Coulomb barrier, the uncertainties may be much larger because of the small deviations of the experimental data from the Rutherford cross section and because of the minor sensitivity of the calculated angular distribution on the underlying OM parameters.

In general, the results from a χ^2 fitting procedure may also depend on the chosen initial values. In the present study I try to use starting values for the parameters of the OMP which roughly correspond to the systematic behavior of volume integrals J_R and J_I of the real and imaginary parts, as e.g.

given in [25]. In practice and in particular for low energies below the Coulomb barrier, the χ^2 landscape turns out to be relatively flat which complicates the fitting procedure and required manual adjusting of the initial values by trial and error. The well-known ambiguities of the parameters of the OMP, in particular towards lower energies, appear also in the present study. However, the determination of the total reaction cross section $\sigma_{\rm reac}$ depends only marginally on the chosen initial values of the fitting procedure as long as the experimental angular distribution covers a sufficiently large angular range.

3.1 ^{208}Pb(α,α)^{208}Pb at $E = 40.4$ MeV

This example is mainly intended to illustrate the importance of a full angular distribution and the essential role of the experimental uncertainties. The data are presented in Fig. 5 of Atzrott et al. [25] with practically no information on the experimental details. I have been involved in this measurement as a student more than 30 years ago, and fortunately all numerical data are still available.

The data will be fitted in different ways. First, a phase shift fit will be used to determine all η_L and δ_L in a model-independent way. For this purpose the approach of Chiste et al. [26] is applied. Second, OM fits will be made using either a folding potential or a standard Woods-Saxon (WS) potential in the real part and a standard WS potential in the imaginary part.

In a first attempt, I fit the experimental data using the statistical uncertainties only. The results are shown in Fig. 1 as dashed lines. It is obvious that the experimental data are not well reproduced with $\chi^2/F \approx 70$ for the phase shift fit and ≈ 100 for the OM fits. The huge χ^2/F result from tiny differences at forward angles where the statistical uncertainties are of the order of 0.01%. In addition, the phase shift fit claims an extreme increase of the angular distribution at backward angles beyond the experimental range. The total cross sections are $\sigma_{\rm reac}$ = 1399 mb for the phase shift fit and 1688 mb (1667 mb) for the OM fit with the folding potential (WS potential) in the real part.

The three fits have been repeated using increased uncertainties. It is stated in the underlying Ph.D. thesis by U. Atzrott that an additional uncertainty of 5% should be added quadratically to the statistical uncertainty to take into account the various systematic uncertainties of the scattering experiment (as discussed above). The resulting fits show $\chi^2/F \approx 0.7$ for the phase shift fit and about 0.9 for the OM fits. These χ^2/F slightly below unity indicate that these increased uncertainties are realistic (maybe, even a bit too high). Now the experimental data are well reproduced over the full angular range of the data, but the phase shift fit still shows a trend to unusual high cross sections at backward angles. The total cross sections are $\sigma_{\rm reac}$ = 1664 mb for the phase shift fit and

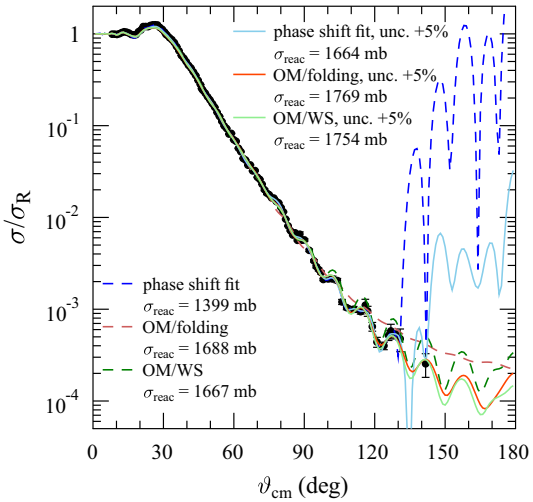

Fig. 1 Angular distribution of the differential cross section of ^{208}Pb(α,α)^{208}Pb elastic scattering at $E = 40.4$ MeV: comparison of experimental data [25] to various fits. The dashed lines result from the statistical uncertainties only; the full lines are obtained from a realistic uncertainty. Further discussion see text

1769 mb (1754 mb) for the OM fit with the folding potential (WS potential) in the real part.

For a better understanding of the various $\sigma_{\rm reac}$ from the different fits, I show the obtained reflexion coefficients η_L and the resulting partial wave cross sections σ_L in Fig. 2. It is obvious that the low $\sigma_{\rm reac}$ from the first phase shift fit (statistical uncertainties only) is related to relatively high η_L for small $L < 15$ where all other approaches show small η_L close to zero. A comparison of the phase shift fit and the OM fits for the data with realistic uncertainties shows that the η_L are quite similar. Only in the small window $18 \le L \le 22$ the σ_L from the phase shift fit are slightly lower than the σ_L from the OM fits, leading to $\sigma_{\rm reac}$ = 1664 mb from the phase shift fit which is about 6% lower than the results from the OM fits with $\sigma_{\rm reac} \approx 1760$ mb.

It must remain an open question whether $\sigma_{\rm reac}$ from the phase shift fit (with its excellent χ^2/F, but strange behavior at backward angles) or from the OM fits (with their implicit restrictions of the model space) provides the best estimate for the real $\sigma_{\rm reac}$ at $E = 40.4$ MeV. Therefore, I finally adopt the average value of $\sigma_{\rm reac} = 1713 \pm 49$ mb which results from the average of the OM fits (1761.5 mb) and the phase shift fit (1664 mb). The uncertainty is taken to include both values (1761.5 mb and 1664 mb). This corresponds to an uncertainty of about 3%. A further reduction of the uncertainty could be achieved from additional data at backward angles. However, the cross sections at backward angles are about 10^{-4} of the Rutherford cross section or about 10^{-8} of the absolute cross sections at forward angles around 10° which complicates the measurements at backward angles.

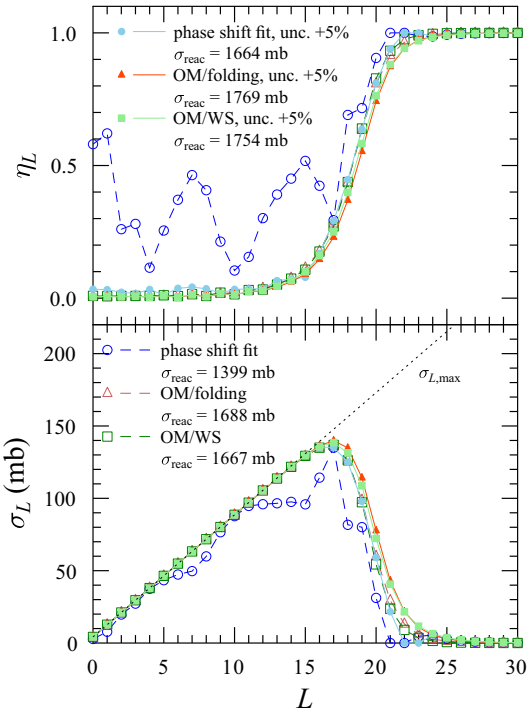

Fig. 2 Reflexion coeffients η_L (upper part) and partial wave cross sections σ_L (lower part) for ^{208}Pb(α,α)^{208}Pb at $E = 40.4$ MeV. Colors and linestyles are identical to Fig. 1. The data are connected by thin lines to guide the eye. The black dotted line indicates the maximum partial wave cross section $\sigma_{L,\max}$ (corresponding to $\eta_L = 0$). Further discussion see text

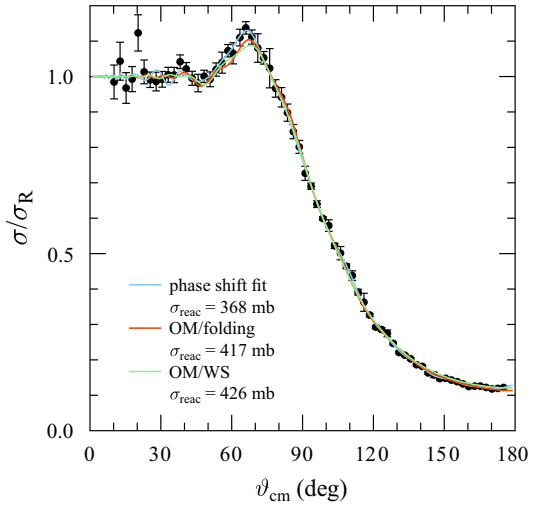

Fig. 3 Angular distribution of the differential cross section of ^{208}Pb(α,α)^{208}Pb elastic scattering at $E = 23.6$ MeV: comparison of experimental data [27] to various fits. Note the small, but significant difference between the phase shift fit and the OM fits in the maximum aound 50°–70° which leads to slightly discrepant σ_{reac}. Further discussion see text

3.2 ^{208}Pb(α,α)^{208}Pb at $E = 23.6$ MeV

This example is mainly intended to illustrate the importance of precise scattering data over the full angular range and the increasing uncertainties of σ_{reac} towards lower energies. Furthermore, limitations in the model space of OM fits will again become visible. The angular distribution at $E = 23.6$ MeV was measured by Karcz et al. [27] already more than 50 years ago. Fortunately, the EXFOR data could be extracted from a table in an underlying report, and thus a re-analysis of the angular distribution is feasible. The data cover the full angular range from about 10° to 175° and reach values of about 10% of the Rutherford cross section at backward angles which is about three orders of magnitude higher than in the previous case at 40.4 MeV. On the one hand, this makes measurements easier because of the higher cross sections. On the other hand, the analysis will be less sensitive because of the smaller deviations from the Rutherford cross section.

In general, the same procedure as in the previous Sect. 3.1 was followed. A phase shift fit and two OM fits with a folding potential and a WS potential were used to extract σ_{reac} from the angular distribution. The fits are shown in Fig. 3.

Overall, the phase shift fit and the OM fits reproduce the experimental data well with $\chi^2/F = 0.9$ for the phase shift fit and 1.2 (1.8) for the OM fit with the folding (WS) potential. But there is a small, but significant difference around the Coulomb/nuclear interference maximum between about 50° and 70°. Both OM fits underestimate the experimental data whereas the phase shift fit is flexible enough to match the data. The higher cross section in the angular distribution of elastic scattering is correlated with a smaller total reaction cross section σ_{reac} which is 368 mb from the phase shift fit and around 420 mb from the two OM fits. The corresponding η_L and σ_L are shown in Fig. 4.

The lower energy of 23.6 MeV (compared to 40.4 MeV in Fig. 2) leads to smaller absorption or η_L closer to unity. This holds in particular for the lowest angular momenta with $L \leq 5$ where $\eta_L \approx 0$ was found at 40.4 MeV (almost full absorption); at 23.6 MeV the η_L are around 0.2–0.5 for $L \leq 5$. The η_L and σ_L from the OM fits show a relatively smooth and similar behavior, leading also to a similar σ_{reac}. Contrary, the η_L from the phase shift fit show a larger scatter and a steeper increase towards $\eta_L \approx 1$ around $L \approx 10$. The corresponding σ_L decrease faster around $L \approx 10$, leading to an overall lower σ_{reac} for the phase shift analysis.

Similar to the conclusions for 40.4 MeV data, it must remain an open question whether σ_{reac} is 368 mb from the phase shift analysis or around 420 mb from the OM fits. Because of the smaller χ^2/F for the phase shift fit and the better description of the data in the maximum of the angular distribution around 50°–70°, I have a slight preference for the phase shift fit. Note that the experimental data at 23.6 MeV cover the full angular range, and thus the phase shift fit cannot behave irregularily at large scattering angles. Similar

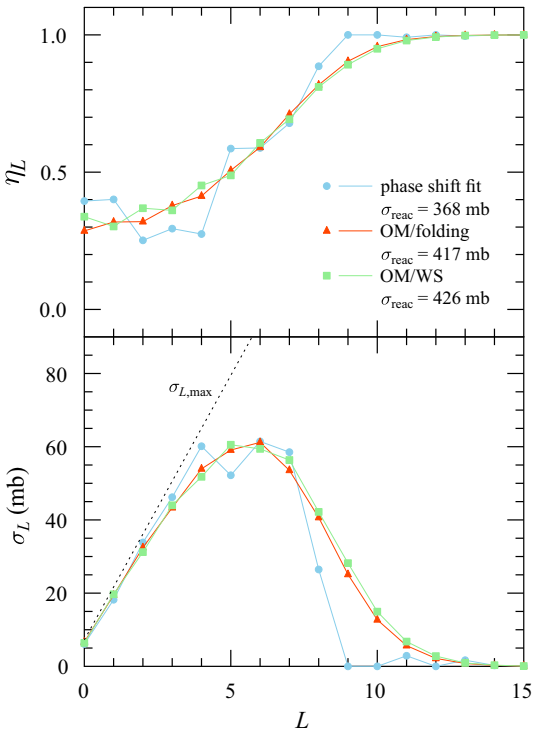

Fig. 4 Reflexion coeffients η_L (upper part) and partial wave cross sections σ_L (lower part) for ^{208}Pb(α,α)^{208}Pb at $E = 23.6$ MeV. Colors and linestyles are identical to Fig. 3. The data are connected by thin lines to guide the eye. The black dotted line indicates the maximum partial wave cross section $\sigma_{L,max}$ (corresponding to $\eta_L = 0$). Further discussion see text

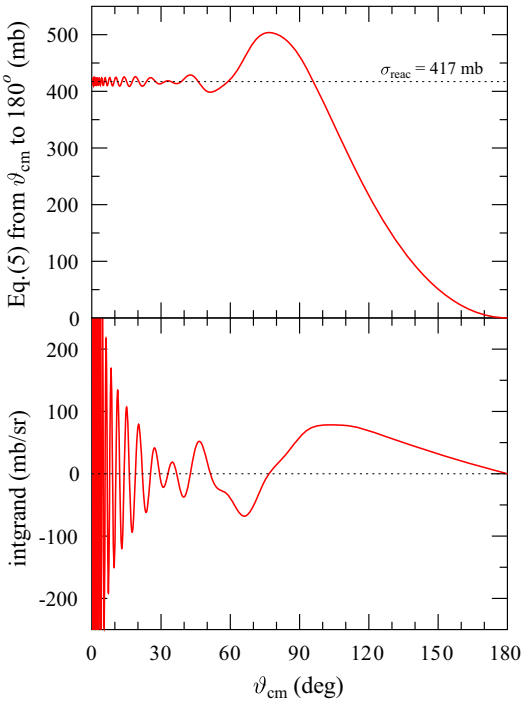

Fig. 5 Lower part: Integrand of Eq. (5) for the determination of the total reaction cross section σ_{reac} from the angular distribution of elastic scattering. Upper part: Integral contribution to σ_{reac} from the integration of Eq. (5) from ϑ to 180°. Further discussion see text

to the 40.4 MeV data, I finally adopt $\sigma_{reac} = 395 \pm 27$ mb from the average and scatter of the phase shift fit on the one hand and the OM fits on the other hand. This corresponds to an uncertainty of about 7% at 23.6 MeV which is roughly twice the uncertainty of σ_{reac} at 40.4 MeV although the data at 23.6 MeV cover a larger angular range.

Finally, it has to be pointed out that a pure OM analysis of the 23.6 MeV data might be interpreted as $\sigma_{reac} = 421.5 \pm 4.5$ mb from the average and scatter of the two OM fits with $\sigma_{reac} = 417$ mb and 426 mb; i.e., an uncertainty of about 1% would be claimed. The phase shift fit reveals that the limitations in the model space of the OM fits would lead to a significant underestimation of the uncertainty of σ_{reac} in the present case.

As this angular distribution at $E = 23.6$ MeV corresponds to $E_{red} = 1.06$ MeV, it is typical for the energy range under study in this work. So I take the chance to illustrate which angular range of the angular distribution in Fig. 3 is most important for the determination of the total reaction cross section σ_{reac}. For this purpose, I use the relation that σ_{reac} results from the angle-integrated difference between the angular distribution $(d\sigma/d\Omega)_R(\vartheta)$ for a point-like charge (pure Rutherford scattering; no absorption and thus $\sigma_{reac} = 0$) and the real angular distribution $(d\sigma/d\Omega)(\vartheta)$:

$$\sigma_{reac} = \int_\Omega \left[\left(\frac{d\sigma}{d\Omega}\right)_R (\vartheta) - \left(\frac{d\sigma}{d\Omega}\right)(\vartheta) \right] d\Omega \quad (4)$$

$$= 2\pi \times \int \left[\left(\frac{d\sigma}{d\Omega}\right)_R (\vartheta) - \left(\frac{d\sigma}{d\Omega}\right)(\vartheta) \right] \times \sin(\vartheta)\, d\vartheta \quad (5)$$

The integrand of Eq. (5) is shown in Fig. 5 (lower part) using the best-fit OM from the folding potential calculation (see red line in Fig. 3). Choosing instead the best-fit from the WS potential or the phase shift fit, would not affect the resulting conclusions.

The Rutherford cross section $(d\sigma/d\Omega)_R(\vartheta)$ shows a very steep $1/\sin^4(\vartheta/2)$ angular dependence. The largest deviation from the Rutherford cross section is found at most backward angles with $\sigma/\sigma_R \approx 0.1$ in this case. However, because of the small absolute Rutherford cross section at backward angles and the additional suppression by the $\sin\vartheta$ factor from the solid angle, the integrand of Eq. (5) remains relatively small at most backward angles. Significantly positive values for the integrand are found at angles around $\vartheta \approx 90°$–$150°$.

Around 60°–80° the cross section in Fig. 3 exceeds the Rutherford cross section in the so-called Coulomb-nuclear interference region, thus leading to a negative integrand in Eq. (5), and for angles below about 40° an oscillatory behavior of the integrand is found. For a quantitative estimate of the

relevance of the negative integrand and the oscillations at forward angles, I have integrated Eq. (5) from a minimum angle $\vartheta_{\min}$ to 180°. The result is shown in Fig. 5, upper part. E.g., the integration of Eq. (5) for the most backward angles from $\vartheta_{\min} = 150°$ to 180° contributes with only 51 mb to the total cross section $\sigma_{\text{reac}} = 417$ mb; the latter value is calculated from Eq. (3). The major contribution to σ_{reac} comes from the angular range between about 90° and 150°. The integration of Eq. (5) from about 95° to 180° leads by accident to the correct σ_{reac}. Integration from about 77° to 180° leads to a result of 504 mb, i.e. overestimating the real σ_{reac}. This overestimation is compensated by the negative integrand in the peak of the Coulomb-nuclear interference. As soon as $\vartheta_{\min}$ is chosen below about 45°, the integration of Eq. (5) leads to the same σ_{reac} as the precise calculation from Eq. (3) with deviations of less than 5%. Note that the huge values of the integrand of Eq. (5) at most forward angles oscillate around zero and cancel each other.

Summarizing, the total reaction cross section σ_{reac} is strongly constrained by the elastic scattering cross sections for angles between about 60° and 150°. The most forward angles do not contribute significantly because the elastic scattering cross section approaches the Rutherford cross section, and the most backward angles do not contribute strongly because the integrand of Eq. (5) remains small. (For an extraordinary exception, see the case of ^{11}Li in Sect. 4.8 with significant deviations of the elastic scattering cross section from the Rutherford cross section already at forward angles.)

3.3 ^{208}Pb(^{10}Be,^{10}Be)^{208}Pb at $E = 38.4$ MeV

This example is mainly intended to illustrate the limits of the present approach for energies far below the Coulomb barrier where the angular distribution of elastic scattering approaches the Rutherford cross section. Furthermore, problems with the re-digitizing of experimental data are briefly mentioned. The experiment has been performed by Kolata et al. [28]. The results are shown in Fig. 1 of [28], but numerical data are not given. Instead, the data have been re-digitized from this figure independently at EXFOR and at NRV. Thus, the data sets at EXFOR and at NRV are close, but not fully identical (see Fig. 6). It must be concluded that – despite the huge efforts at EXFOR and NRV which I highly appreciate – the usage of re-digitized data for fitting cannot be recommended without special care.

Kolata et al. [28] provide two OM fits with either a deep or a shallow WS potential with $\sigma_{\text{reac}} = 3$ mb or 10 mb. Naively, one might conclude that the experimental data constrain the total reaction cross section to $\sigma_{\text{reac}} = 6.5 \pm 3.5$ mb. It is clear from the findings in the previous Sect. 3.2 that such an approach underestimates the real uncertainties. This was already noticed by Kolata et al., and their Fig. 2 shows σ_{reac}

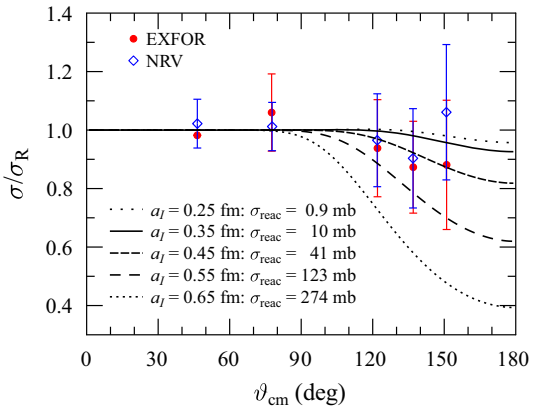

Fig. 6 Angular distribution of the differential cross section of ^{208}Pb(^{10}Be,^{10}Be)^{208}Pb elastic scattering at $E = 38.4$ MeV: comparison of experimental data [28] to various calculations. Note that the two data sets—re-digitized independently at EXFOR and NRV from Fig. 1 in [28]—are not in perfect agreement. The small deviation of the experimental data from the Rutherford cross section prevents a reliable determination of σ_{reac}. Further discussion see text

with a center value of about 9.5 mb and a much larger error bar from less than 1 mb up to 40 mb.

The full line in Fig. 6 corresponds to the deep potential in Kolata et al. with $\sigma_{\text{reac}} = 10$ mb which uses a relatively small diffuseness of the imaginary part of $a_I = 0.35$ fm. The calculations are repeated varying a_I between 0.25 fm and 0.65 fm. The total reaction cross section increases with increasing imaginary diffuseness a_I from 0.9 mb ($a_I = 0.25$ fm) up to 274 mb ($a_I = 0.65$ fm). It becomes obvious from Fig. 6 that the experimental data are compatible (with $\chi^2/F < 1$) with $\sigma/\sigma_R = 1.0$ and thus with $\sigma_{\text{reac}} = 0$ mb; i.e., the data can provide an upper limit only. Depending on the choice of the data from EXFOR or NRV, this upper limit is around 150 mb (EXFOR) or around 80 mb (NRV).

3.4 ^{208}Pb(^{16}O,^{16}O)^{208}Pb at $E = 78$ MeV

This example is mainly intended to illustrate further uncertainties in the determination of σ_{reac}. Elastic scattering angular distributions for ^{208}Pb(^{16}O,^{16}O)^{208}Pb at $E = 78$ MeV are available from three independent experiments.

Lilley et al. [29] show data between about 85° and 170°. The data are normalized to the Rutherford cross section at the most forward angle, and the lowest cross section is slightly below 0.6 of the Rutherford cross section at 170°. The data are not avaibable at EXFOR or NRV. Lilley et al. provide a careful OM study with a wide variation of parameters, leading to σ_{reac} between 36 mb and 57 mb. Despite the concerns in Sect. 3.2, it seems reasonable to adopt $\sigma_{\text{reac}} = 46.4 \pm 7.5$ mb because of the extensive study of the parameter space in this analysis.

Almost simultaneously, the data by Vulgaris et al. [30] were published in 1986. Also these data are not available at EXFOR or NRV. The data cover a smaller angular range from about 100° to 170°. The cross section at the most backward angles is about 0.6 of the Rutherford cross section, i.e., marginally higher than the Lilley et al. data. The OM analysis provides only one data set in a subsequent paper [31] with $\sigma_{\rm reac}$ = 40.1 mb which is slightly lower, but within the error bars of the Lilley et al. result for $\sigma_{\rm reac} = 46.4 \pm 7.5$ mb.

About 15 years later, Silva et al. [32] have measured a series of scattering data for ^{16}O. The data are available at EXFOR after re-digitization of Fig. 3 of [32]. The data cover a wider angular range from about 60° to 175°. Although the re-digitization imposes some additional uncertainties, it is clear that the cross sections at the most backward angles are much higher with about 0.75 of the Rutherford cross section, compared to about 0.6 from the Lilley et al. and Vulgaris et al. data. As $\sigma_{\rm reac}$ is not given by Silva et al., I have re-fitted the data from EXFOR. As expected, the higher elastic scattering cross sections at backward angles correspond to a significantly lower $\sigma_{\rm reac}$ of 27.6 mb.

The three results are shown in Fig. 7. The reason for the discrepancy between the relatively high backward cross sections by Silva et al. [32] and the lower cross sections by Lilley et al. [29] and Vulgaris et al. [30] remains unclear. Most likely, the discrepancy results from small differences in the projectile energies which are given as "78 MeV" in all cases. If this is a rounded value, the real energy can be between 77.5 MeV and 78.4 MeV. Furthermore, a minor correction to the laboratory energy of the projectile should be made to take into account the energy loss in the target. (This correction remains below 100 – 200 keV in the present cases, depending on the target thickness.) Note that a reduction of the energy by 0.5 MeV results in a lower $\sigma_{\rm reac}$ by about 20%, thus potentially explaining the range of the observed $\sigma_{\rm reac}$ in the three experiments at the nominal energies of 78 MeV.

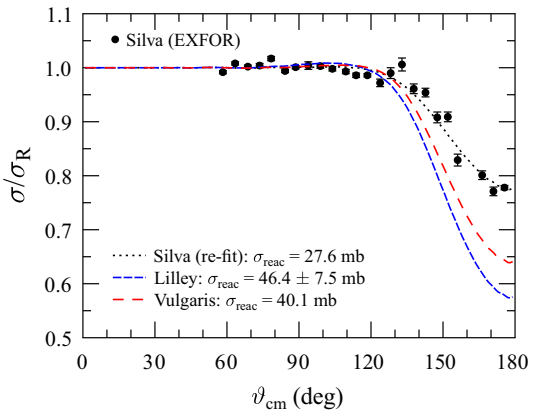

Fig. 7 Angular distribution of the differential cross section of ^{208}Pb(^{16}O,^{16}O)^{208}Pb elastic scattering at $E = 78$ MeV: comparison of experimental data [32] with a new fit (present work) to the best-fit calculations based on the experiments of [29] and [30]. There is obvious disagreement between the experimental data, leading to total cross sections between slightly above 40 mb from [29,30] and slightly below 30 mb from [32]. Further discussion see text

3.5 Some conclusions from the above examples

The following conclusions can be drawn from the above four examples in Sects. 3.1, 3.2, 3.3, and 3.4. (*i*) Typical uncertainties for the determination of the total reaction cross section $\sigma_{\rm reac}$ from elastic scattering angular distributions are of the order of a few per cent at energies above the Coulomb barrier, but increase significantly to about 10 – 20% around the Coulomb barrier and even larger values at very low energies. (*ii*) Precise angular distributions over the full angular range (including experimental uncertainties) are required to obtain very robust results for $\sigma_{\rm reac}$ and to achieve the claimed uncertainties. (*iii*) The restricted model space in OM calculations may constrain the calculated $\sigma_{\rm reac}$ and thus lead to an underestimation of the uncertainty of $\sigma_{\rm reac}$. For light projectiles, this can be investigated by an additional phase shift fit. (*iv*) The $\sigma_{\rm reac}$ calculated from an OM fit is not inevitably the precise $\sigma_{\rm reac}$ of the system under study. But the $\sigma_{\rm reac}$ from any OM fit which reproduces the experimental angular distribution of elastic scattering over a wide angular range, is a reasonable estimate of the precise $\sigma_{\rm reac}$ within the uncertainties as listed above. (*v*) The energy of the projectile should be given as the effective energy in the middle of the target with higher precision because of the steep energy dependence of $\sigma_{\rm reac}$ at low energies below the Coulomb barrier.

3.6 Quasi-elastic data and inelastic scattering to low-lying states

In several cases under study, the energy resolution was not sufficient to distinguish between elastic scattering and inelastic scattering to low-lying excited states of the projectiles. This holds in particular for several even-odd projectiles like ^{7}Li, ^{7}Be, ^{11}Be, ^{17}O, ^{17}F, and ^{19}F. In these cases the experimental angular distributions are often called quasi-elastic angular distributions.

This leads to the following consequences for the analysis of the angular distribution and the determination of the total reaction cross section $\sigma_{\rm reac}$. The quasi-elastic peak in the energy spectrum of the scattered projectiles is composed of the elastic contribution and – depending on the scattering angle – a more or less significant inelastic contribution. Whereas at forward angles the elastic contribution dominates, at backward angles the measured quasi-elastic peak will be somewhat higher than the elastic peak only. Consequently, the deviation from the Rutherford cross section is smaller in the quasi-elastic analysis than it would be in the analysis of the purely elastic data. Such a smaller deviation

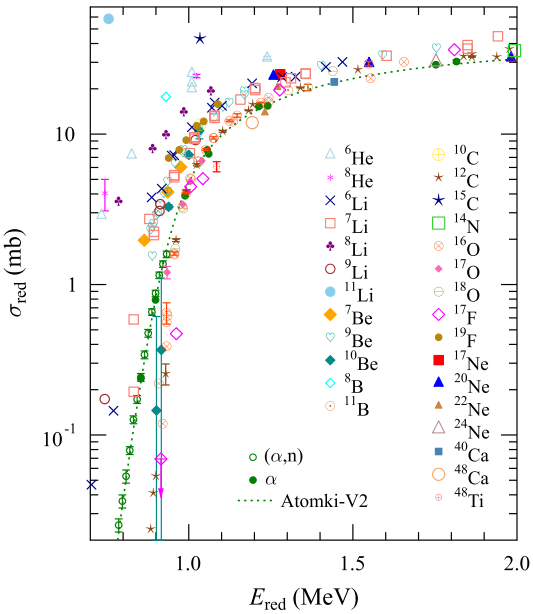

Fig. 8 Reduced cross sections σ_{red} as a function of the reduced energy E_{red}. Larger values of σ_{red} are found for weakly bound projectiles, in particular towards lower energies. Further discussion see text

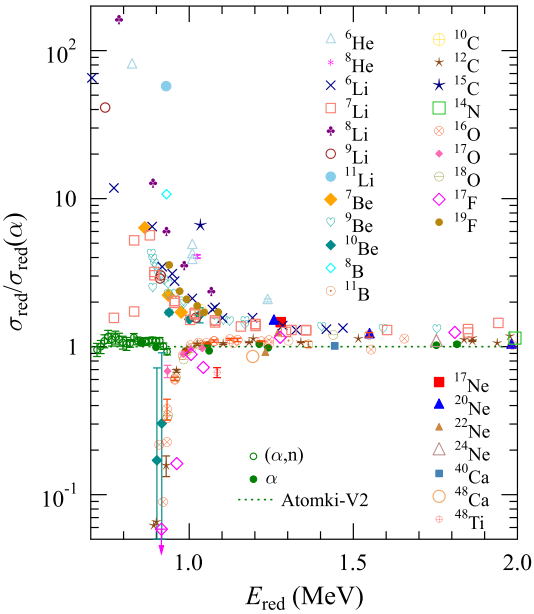

Fig. 9 Ratios of the reduced cross sections σ_{red} to a reference $\sigma_{red}(\alpha)$. Here not only the enhanced σ_{red} for weakly bound projectiles can be seen, but also unexpectedly small σ_{red} for several projectiles with masses above $A = 10$ at low E_{red} below about 1 MeV become more visible. Further discussion see text

from the Rutherford cross section leads to an underestimation of the total reaction cross section σ_{reac} when quasi-elastic data are analyzed in the optical model.

The effect is most pronounced for a strong coupling to the low-lying states, i.e. for cases with a low excitation energy E_x of the low-lying states and a small spin difference ΔJ. Grineviciute and Descouvemont [33] have applied a microscopic continuum discretized coupled-channels model for the case of ^{19}F with its low-lying states at $E_x = 110$ keV ($J^\pi = 1/2^-$) and 197 keV ($5/2^+$) which can be populated from the $1/2^+$ ground state with $\Delta J = 0$ and 2 (see also Sect. 4.24). It is concluded in [33] that "the theoretical inelastic contribution to the quasi-elastic scattering data is small". Because the excitation energies of the lowest states are higher in the other even-odd projectiles, it is reasonable to assume that the underestimation of the total reaction cross section σ_{reac} from the analysis of quasi-elastic angular distributions remains minor not only for ^{19}F but also for the other even-odd projectiles in the present study.

4 Data under study

All energies E in the following discussion will be given in the laboratory system (except explicitly given as $E_{c.m.}$). All reduced energies E_{red} are related to the center-of-mass energies $E_{c.m.}$ by Eq. (1).

All derived reduced cross sections σ_{red} are shown in Fig. 8.

Because of the steep energy dependence of σ_{red} towards low energies, the data are also presented in Fig. 9 as ratio to a reference cross section $\sigma_{red}(\alpha)$ which is calculated for the system ^{208}Pb + α, see Sect. 4.1. In this presentation it becomes visible that there are not only enhanced σ_{red} for weakly bound projectiles, but also unexpectedly small σ_{red} for several projectiles with masses above $A = 10$ at low E_{red} below about 1 MeV. These results will be discussed later in Sect. 5. The α particle has been chosen as a reference in the present study because (i) it is a doubly-magic nucleus, usually considered as a typical tightly bound projectile, and (ii) σ_{reac} can be determined from the available experimental data with small uncertainties down to low reduced energies $E_{red} \approx 0.7$ MeV.

In the following subsections I provide further information for each reaction under study. I start with a detailed discussion of the ^{208}Pb(α,α)^{208}Pb reaction which is used as reference in Fig. 9.

Because of the huge number of data points in Figs. 8 and 9, additional figures with reduced cross sections σ_{red} and ratios $\sigma_{red}/\sigma_{red}(\alpha)$ are shown for those cases which required an extended discussion (Figs. 10, 11, 12, 13, 14, 15, 16, 17, 18, 19, 20, 21, 22 and 23). The presentation of the data in these additional Figs. 10, 11, 12, 13, 14, 15, 16, 17, 18, 19, 20, 21, 22 and 23 uses the following strategy, here explained for the example of the lithium isotopes in Figs. 12 and 13. If data are available only from one experiment (e.g., ^{8}Li and ^{9}Li), the additional figures use the same symbol and color as in the overview Figs. 8 and 9. The same symbol and color are also used in cases when data sets from several experiments are

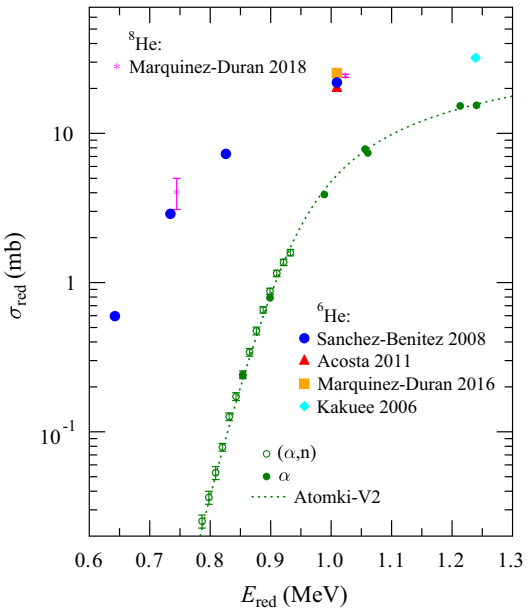

Fig. 10 Same as Fig. 8, but with different scale to visualize the σ_{red} data for ^{6}He and ^{8}He which are far above the reference σ_{red} for the tightly bound α particle

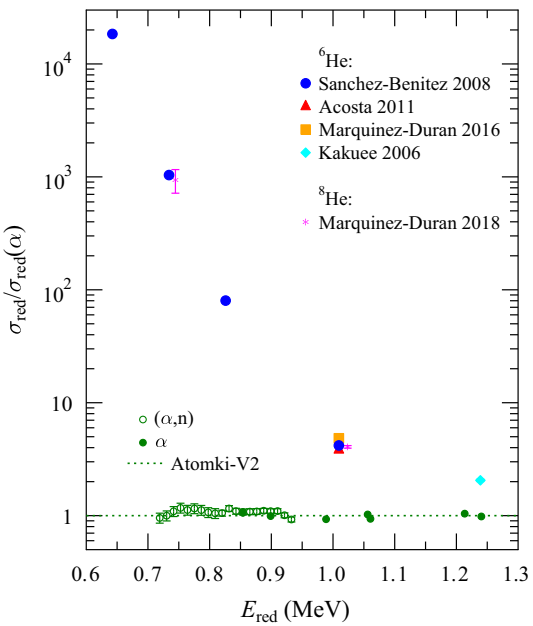

Fig. 11 Same as Fig. 9, but with different scale to visualize the σ_{red} data for ^{6}He and ^{8}He which are far above the reference σ_{red} for the tightly bound α particle. Note the strong energy dependence of the ratio $\sigma_{red}/\sigma_{red}(\alpha)$

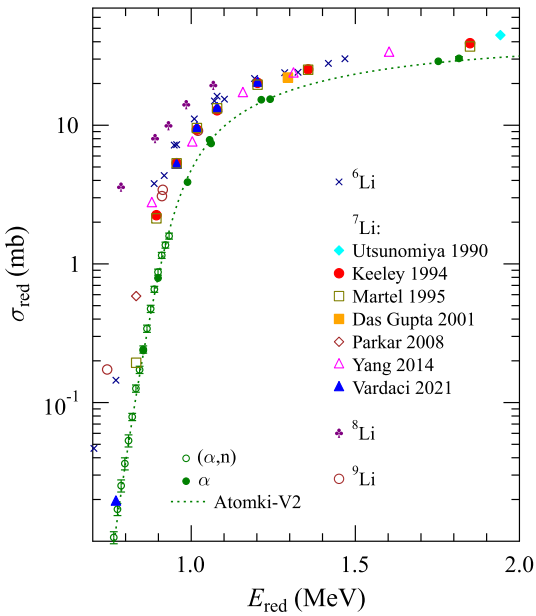

Fig. 12 Same as Fig. 8, but with different scale to visualize the σ_{red} data for ^{6}Li, ^{7}Li, ^{8}Li, and ^{9}Li. The discrepancies between the experimental data sets towards low energies are better visible in the ratios, see Fig. 13. Further discussion see text

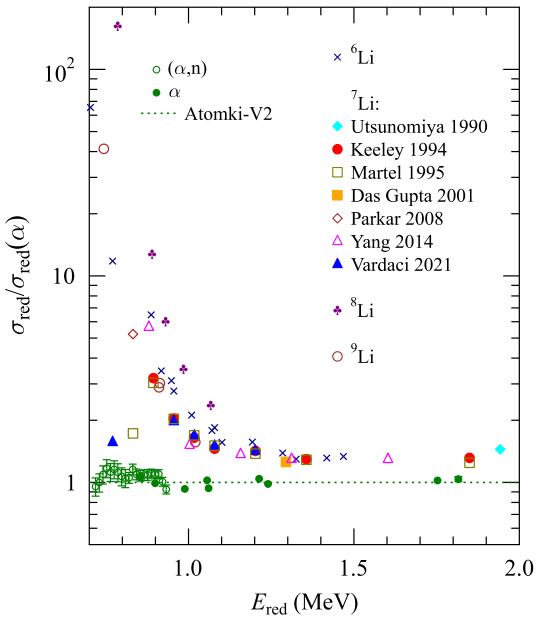

Fig. 13 Same as Fig. 9, but with different scale to visualize the σ_{red} data for ^{6}Li, ^{7}Li, ^{8}Li, and ^{9}Li. Note the low values of Martel et al. [53] and Vardaci et al. [54] for ^{7}Li towards low energies. Further discussion see text

consistent (e.g., ^{6}Li). For ^{7}Li, the energy dependence of the σ_{red} from various experiments differs. Only for these cases, the different experimental data sets are shown with different colors and symbols.

4.1 ^{208}Pb + ^{4}He

Several angular distributions of elastic scattering at energies around the Coulomb barrier are available in literature. Because of the above discussion I restrict myself to studies which either provide σ_{reac} in the original publication or

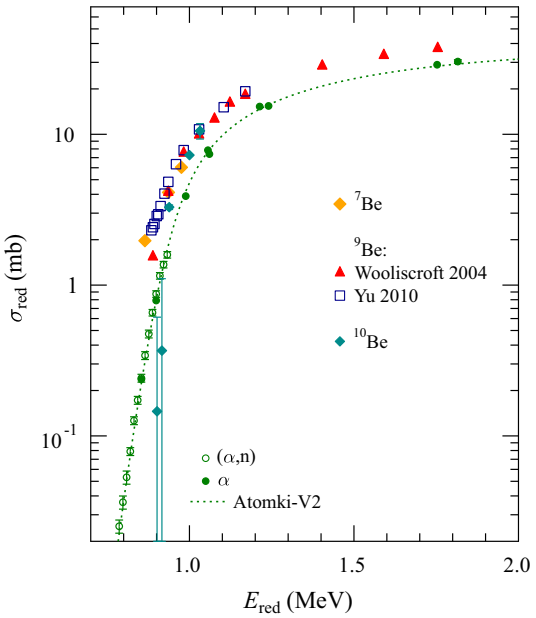

Fig. 14 Same as Fig. 8, but with different scale to visualize the σ_{red} data for ^{7}Be, ^{9}Be, and ^{10}Be. The small discrepancies between the experimental data sets for ^{9}Be towards low energies are better visible in the ratios, see Fig. 15. Further discussion see text

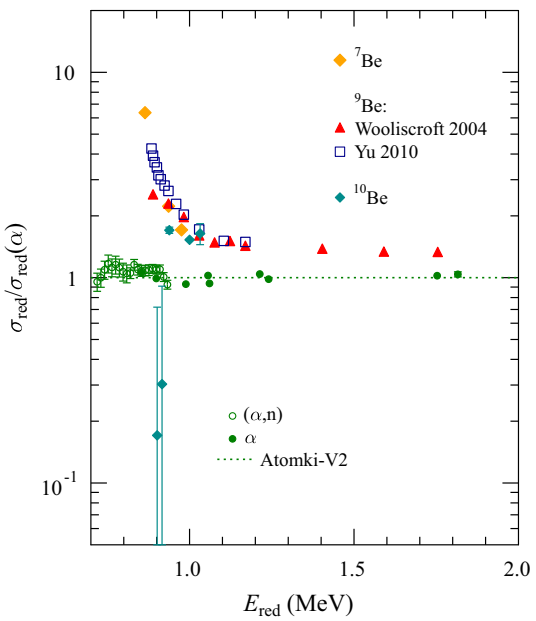

Fig. 15 Same as Fig. 9, but with different scale to visualize the σ_{red} data for ^{7}Be, ^{9}Be, and ^{10}Be. There are minor differences in the energy dependence of the two data sets by [65] and [66] towards low energies. Contrary to ^{7}Be and ^{9}Be, the σ_{red} from the ^{208}Pb(^{10}Be,^{10}Be)^{208}Pb data [28] show a completely different energy dependence. Further discussion see text

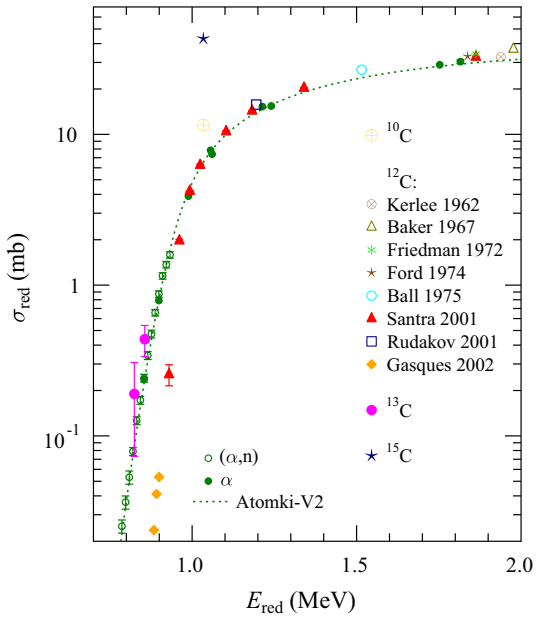

Fig. 16 Same as Fig. 8, but with different scale to visualize the σ_{red} data for ^{10}C, ^{12}C, ^{13}C, and ^{15}C. Note the huge σ_{red} for ^{15}C and the small σ_{red} for ^{12}C towards low energies which are better visible in the ratios, see Fig. 17. Further discussion see text

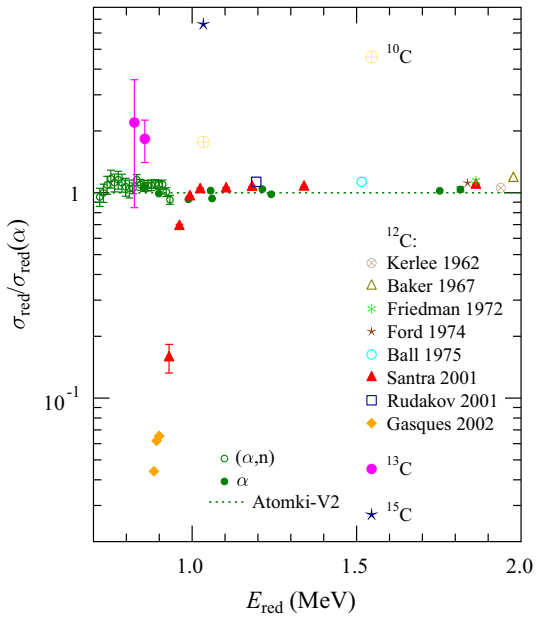

Fig. 17 Same as Fig. 9, but with different scale to visualize the σ_{red} data for ^{10}C, ^{12}C, ^{13}C, and ^{15}C. Below $E_{red} \approx 1$ MeV, the σ_{red} for ^{12}C are lower than the reference data $\sigma_{red}(\alpha)$. Further discussion see text

the numerical data are available or sufficient information is available for a re-analysis.

Three angular distributions at 19, 20, and 22 MeV have been measured by Barnett et al. [34]. σ_{reac} can be calculated from the given OMP parameters. The same holds for the data by Lilley et al. [35] at 23.5 MeV. Data by Karcz et al. [27] are available at 23.6 and 27.6 MeV. The 23.6 MeV data have been discussed in detail in Sect. 3.2. The 27.6 MeV data have been re-analyzed in a similar way. The results of Lilley et al. and Karcz et al. agree within about 5% around

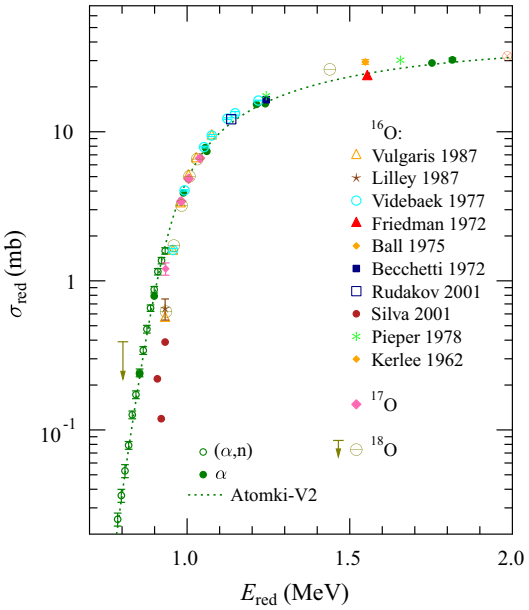

Fig. 18 Same as Fig. 8, but with different scale to visualize the σ_{red} data for ^{16}O, ^{17}O, and ^{18}O. Note the small σ_{red} for ^{16}O towards low energies which are better visible in the ratios, see Fig. 19. Further discussion see text

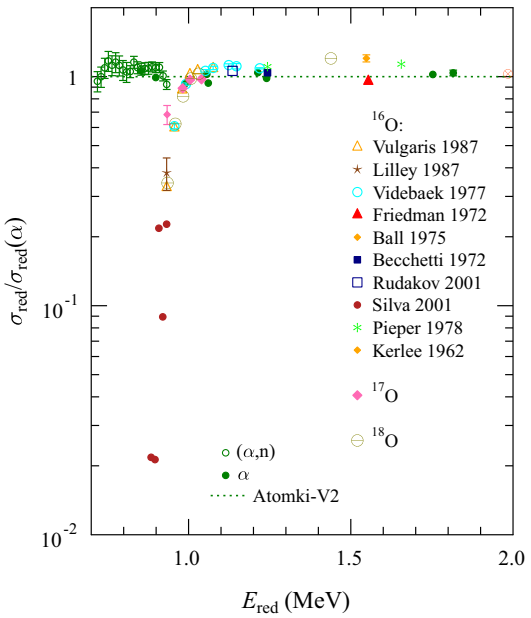

Fig. 19 Same as Fig. 9, but with different scale to visualize the σ_{red} data for ^{16}O, ^{17}O, and ^{18}O. Similar to the findings for ^{12}C, below $E_{red} \approx 1$ MeV, the σ_{red} for ^{16}O are lower than the reference data $\sigma_{red}(\alpha)$. A similar trend is observed for ^{18}O. Further discussion see text

23.5 MeV. The data by Baxter et al. [36] at 27.0 MeV were already analyzed in [25]. That analysis was confirmed by a new fit to the EXFOR data, leading to almost the same σ_{reac} as by Karcz et al. at 27.6 MeV. At 39 MeV an angular distribution is available by Gonchar et al. [37]. The EXFOR data are taken from an underlying preprint which allows a reasonable estimate of σ_{reac} although the data do not cover a wide angular range. Finally, the data by Atzrott et al. [25] at 40.4 MeV were already analyzed in Sect. 3.1. The resulting σ_{reac} of the data at 39 MeV by Gonchar et al. and the data at 40.4 MeV by Atzrott et al. are consistent. The data of Hudson et al. [38] between 19.5 MeV and 25.5 MeV were not re-analyzed because the EXFOR data set is based on a re-digitization. All σ_{reac} from the analysis of ^{208}Pb$(\alpha,\alpha)^{208}$Pb elastic scattering are shown in Figs. 8 and 9 with small green full circles. The elastic scattering data cover an energy range of 0.85 MeV $\leq E_{red} \leq$ 1.82 MeV.

It is difficult to provide σ_{reac} at lower energies from elastic scattering because the angular distribution shows only tiny deviations from the Rutherford cross section below about 20 MeV. But it has been shown that the total reaction cross section is well approximated by the (α,n) cross section for heavy target nuclei at energies above the (α,n) threshold and below the $(\alpha,2n)$ threshold, see e.g. Fig. 3 of [39]. Therefore, I extend the energy range under study for ^{208}Pb + α towards lower energies using the ^{208}Pb$(\alpha,n)^{211}$Po data by Barnett et al. [34]. The approximate σ_{reac} data from the (α,n) reaction are shown in Figs. 8 and 9 with small green open circles. The (α,n) data cover an energy range down to $E_{red} \approx 0.72$ MeV

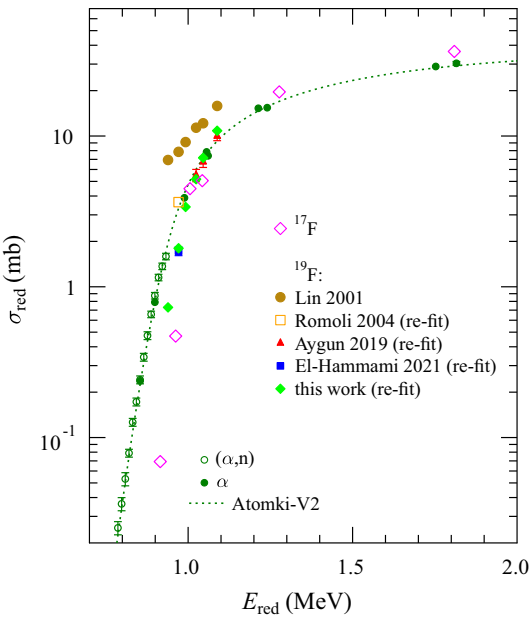

Fig. 20 Same as Fig. 8, but with different scale to visualize the σ_{red} data for ^{17}F and ^{19}F. Note the discrepant σ_{red} for ^{19}F from the different analyses which become better visible in the next Fig. 21. Further discussion see text

and overlap with the data from elastic scattering around $E_{red} \approx 0.9$ MeV.

It has been shown that the Atomki-V2 α-nucleus OMP is able to predict the total reaction cross section of α-induced reactions for heavy nuclei at low energies [40,41]. The result

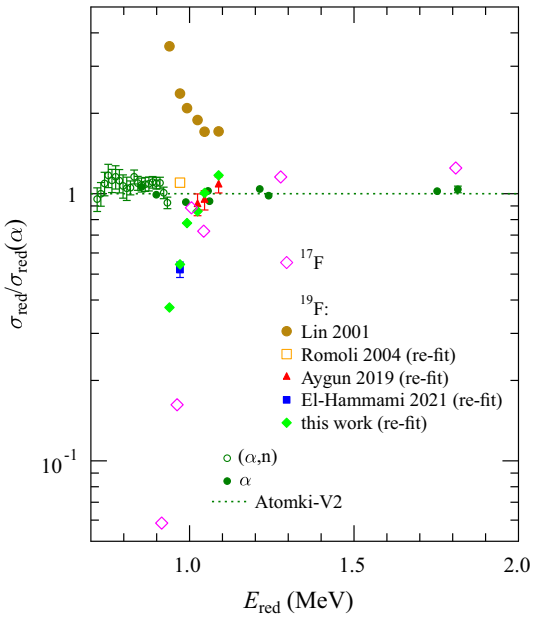

Fig. 21 Same as Fig. 9, but with different scale to visualize the σ_{red} data for ^{17}F and ^{19}F. Whereas the original analysis of Lin et al. [103] shows high σ_{red} for ^{19}F like for typical weakly bound projectiles, several subsequent OM analyses of these experimental data indicate much lower σ_{red}, similar to tightly bound nuclei. Further discussion see text

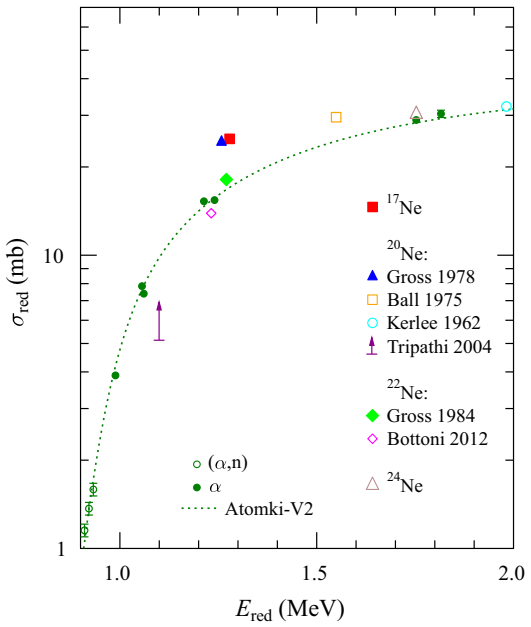

Fig. 22 Same as Fig. 8, but with different scale to visualize the σ_{red} data for ^{17}Ne, ^{20}Ne, ^{22}Ne, and ^{24}Ne. The lower limit from the sum of fusion cross sections of Ref. [107] is shown in addition. Further discussion see text

is shown in Figs. 8 and 9 as a dotted green line. The deviations between the calculated σ_{reac} from the Atomki-V2 OMP and the experimental data is less than 10% for all data from elastic scattering and most (α,n) data. The largest deviations are found around E_{red} between 0.75 MeV and 0.78 MeV; the deviations do not exceed 17%. The found ratio close to unity between the experimental and the calculated σ_{reac} over the full energy range under study confirms the consistency of the present analysis of σ_{reac}.

The excellent reproduction of the experimental σ_{reac} data using the Atomki-V2 OMP allows a reliable interpolation between the experimental data points. The calculated σ_{reac} from the Atomki-V2 OMP are converted to reduced cross sections σ_{red} which are then used as a reference for comparison of the σ_{red} from the different systems under study. The presentation of the ratio $r = \sigma_{red}/\sigma_{red}(\alpha)$ in Fig. 9 is suitable for comparison between the different systems under study because it circumvents the steep energy dependence of σ_{red} towards lower energies. Details of the energy dependence of σ_{red} for the various projectiles under study will be better visible in Fig. 9 with the ratios $\sigma_{red}/\sigma_{red}(\alpha)$ than in the presentation of the σ_{red} in Fig. 8.

The reference calculation is listed in Table 2 in the Appendix. The table includes the reduced energy E_{red}, the reduced cross section σ_{red}, the underlying energy $E_{c.m.}$ in the center-of-mass system and the total reaction cross section σ_{reac}. In addition, the astrophysical S-factor $S(E)$ is given.

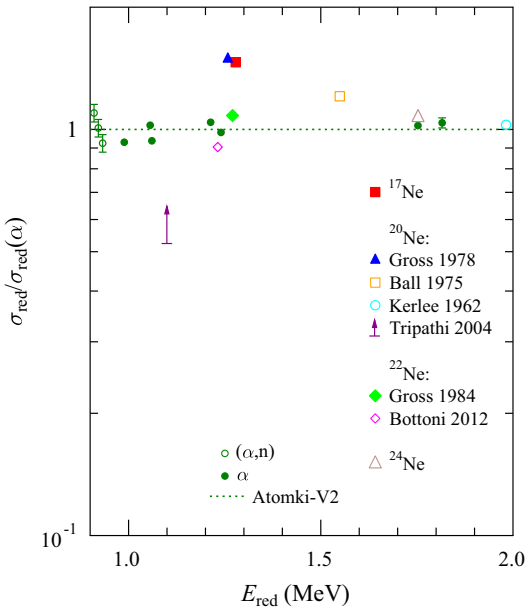

Fig. 23 Same as Fig. 9, but with different scale to visualize the σ_{red} data for ^{17}Ne, ^{20}Ne, ^{22}Ne, and ^{24}Ne. Further discussion see text

4.2 ^{208}Pb + ^{6}He

Several experiments have been done for ^{208}Pb(^{6}He,^{6}He) ^{208}Pb elastic scattering. The data by Sánchez-Benítez et al. [42] cover the low energy region between 14 MeV and 22 MeV. σ_{reac} is not given in [42], but the OMP parameters allow to reproduce the fits and to calculate σ_{reac} between 35.7 mb

Table 1 Reduced cross sections σ_{red} for ^{7}Be, ^{9}Be, ^{10}Be, and ^{11}Be from elastic scattering on ^{208}Pb at higher energies above E_{red} = 2 MeV [67,69,70]. The neutron-halo nucleus ^{11}Be shows a strongly enhanced ratio to the reference calculation (marked in bold), compared to the weakly bound ^{7}Be and ^{9}Be and the tightly bound ^{10}Be

projectile	E_{lab} (MeV)	σ_{reac} (mb)	E_{red} (MeV)	σ_{red} (mb)	$\sigma_{red}/\sigma_{red}(\alpha)$
^{11}Be[1]	140	7798	3.30	117.4	**3.05**
^{10}Be[1]	127	3067	2.98	47.0	1.25
^{9}Be [1]	88	2473	2.06	38.6	1.20
^{7}Be[2]	130	3063	3.01	49.9	1.32
^{7}Be [3]	125	3182	2.89	51.8	1.38

[1]Ref. [67]
[2]Ref. [69]
[3]Ref. [70]

at 14 MeV and 1315 mb at 22 MeV. There are two further angular distributions at 22 MeV by Acosta et al. [43] and Marquínez-Durán et al. [44]. The numerical data by Acosta et al. are available at EXFOR. Because σ_{reac} is not given in [43], the angular distribution was re-fitted, leading to σ_{reac} = 1205 mb. Marquínez-Durán et al. have analyzed their own data with σ_{reac} = 1522 mb, and a further analysis of a combined data set at 22 MeV leads to σ_{reac} = 1459 mb in [44]. Finally, at 27 MeV $\sigma_{reac} = 1924 \pm 46$ mb is derived from the experimental data by Kakuee et al. [45] using the two almost identical fits to the data in the subsequent paper [46], Table 1, last two lines.

The experimental data cover the range of 0.64 MeV $\leq E_{red} \leq$ 1.24 MeV. The σ_{red} values for ^{6}He are significantly higher than the reference values, see the light-blue open triangles in Figs. 8 and 9. For better visualization, the data for ^{6}He are shown in the separate Figs. 10 and 11.

Figures 10 and 11 nicely show that the σ_{red} for ^{6}He are by far higher than the σ_{red} for the tightly bound α particle. In addition, there is a strong energy dependence with increasing ratios $\sigma_{red}/\sigma_{red}(\alpha)$ towards lower energies. Although the uncertainties of σ_{red} at the lowest energies may be huge (see discussion in Sect. 3), the trend of increasing σ_{red} of ^{6}He towards lower energies is an experimental fact. It has been interpreted as a signature of the two-neutron halo in ^{6}He with its α + 2n cluster structure [42–46] and the low two-neutron separation energy of only 975 keV. Such a halo structure corresponds to a wave function with a long-range tail which leads to absorption of the incoming ^{6}He projectiles at large radii which becomes more and more relevant towards sub-barrier energies. In OM calculations, this is reflected by a shift of the imaginary potential towards larger radii for low energies. This effect was also observed in other ^{6}He + nucleus scattering data, see e.g. [47,48].

4.3 ^{208}Pb + ^{8}He

Only few data are available for ^{208}Pb(^{8}He,^{8}He)^{208}Pb elastic scattering. A first experiment by Marquínez-Durán et al. [44] determined σ_{reac} of this reaction as 1520 mb at 16 MeV. In a subsequent experiment by the same collaboration [49] further data at 22 MeV were measured, and a common analysis gave $\sigma_{reac} = 1529 \pm 40$ mb at 22 MeV and 254 ± 60 mb at 16 MeV. I show only the data from the latter paper in Figs. 8, 9, 10, and 11 as small magenta stars. The experimental data cover the range of E_{red} from 0.74 MeV to 1.02 MeV.

The σ_{red} for ^{8}He show almost the same behavior as the σ_{red} for ^{6}He. The σ_{reac} for ^{8}He are significantly enhanced in comparison to the reference data, and the enhancement is increasing towards lower energies. Interestingly, noticable differences between the required OMP for ^{6}He and ^{8}He have been identified in [49]. The discussion in [49] points out that several reaction mechanisms like one-neutron and two-neutron transfer, breakup, and to minor extend also fusion contribute to the total reaction cross section σ_{reac} for ^{8}He. A tentative conclusion is drawn in [49] that the breakup cross section for ^{8}He must be considerably smaller than for ^{6}He. Although the different reaction mechanisms may contribute in varying weights to the σ_{reac} for ^{8}He and ^{6}He, at the end a very similar behavior of the σ_{red} for ^{8}He and ^{6}He is found.

4.4 ^{208}Pb + ^{6}Li

Several experimental angular distributions of ^{208}Pb (^{6}Li,^{6}Li)^{208}Pb elastic scattering are avilable in literature. The data by Gemmeke et al. [50] cover the energy range between 23 MeV and 48 MeV. Total reaction cross sections are not provided, but the σ_{reac} can be re-calculated from the given OMP parameters. In the same energy range Keeley et al. [51]

provide angular distributions between 27 MeV and 39 MeV. Here the $\sigma_{\rm reac}$ are listed in their Table 2. Chun-Lei et al. [52] provide further angular distributions between 25 MeV and 46 MeV. The authors provide only the depths of real and imaginary potentials at the sensitivity radius R_S, but no information on the underlying WS parameters and on the obtained $\sigma_{\rm reac}$ is given in [52]. Fortunately, the original data are available at EXFOR, and so it is possible to re-fit the data and determine $\sigma_{\rm reac}$ without major problems.

The derived $\sigma_{\rm reac}$ from the different experiments [50–52] cover reduced energies $E_{\rm red}$ between 0.70 MeV and 1.47 MeV. The $\sigma_{\rm reac}$ are consistent with each other. The data can be found as blue crosses in Figs. 8 and 9 at the upper end of the bulk of data for weakly bound projectiles. The data are also added for comparison to the plots for ^{7}Li in the next section, see Figs. 12 and 13. The $\sigma_{\rm red}$ for ^{6}Li are slightly lower than the $\sigma_{\rm red}$ for the neutron halo nucleus ^{6}He, but both data sets for $\sigma_{\rm red}$ of ^{6}Li and ^{6}He show a similar slope with an increasing ratio $\sigma_{\rm red}/\sigma_{\rm red}(\alpha)$ towards lower energies. This finding is reflected in the properties of the ^{6}Li nucleus. Similar to ^{6}He, also for ^{6}Li strong clustering is expected with a dominant $\alpha + d$ contribution in the wave function. The separation energy of the two clusters is also quite low with 1.47 MeV, but slightly higher than in the ^{6}He case. At higher energies above the Coulomb barrier around $E_{\rm red} \approx 1.5$ MeV, the data for ^{6}Li follow the general trend of $\sigma_{\rm red}$ for weakly bound projectiles which is about a factor of 1.5 above the reference $\sigma_{\rm red}(\alpha)$ from the ^{208}Pb(α,α)^{208}Pb reaction.

4.5 ^{208}Pb + ^{7}Li

The experimental situation for ^{208}Pb(^{7}Li,^{7}Li)^{208}Pb is more complicated than in the previous cases. There is a low-lying level at $E^* = 478$ keV in ^{7}Li. The experimental energy resolution of the scattering experiments is not always sufficient to resolve the $3/2^-$ ground state and $1/2^-$ excited state at 478 keV. This may be one explanation for the discrepant experimental results for this reaction.

Utsunomiya et al. [55] have measured an angular distribution at 63 MeV from about 10° to 70°, corresponding to $E_{\rm red} = 1.94$ MeV, i.e., the upper end of the energy range under study. $\sigma_{\rm reac}$ is not given, but can be re-calculated from the OMP parameters. Keeley et al. [51] have covered a broad energy range between 29 and 60 MeV. The $\sigma_{\rm reac}$ are provided in their Table 1, and a subsequent re-analysis by Martel et al. [53] confirmed these results. Das Gupta et al. [56] measured an angular distribution at 42 MeV; $\sigma_{\rm reac}$ was recalculated from the OMP parameters in their Table 1. Parkar et al. [57] provide an angular distribution over the full angular range at 27 MeV. The data had to be re-fitted because no OMP parameters are given; fortunately, the data set at EXFOR was provided by the authors as numerical table. The data by Yang et al. [58] cover a wide energy range from 25.7 MeV to 42.6 MeV. In addition, an earlier experiment by Zeller et al. [59] at 52 MeV is re-analyzed; this data point from the Zeller data is included in the data set of Yang in the presentation. The $\sigma_{\rm reac}$ have been recalculated from the OMP parameters in Table I. Recently, new angular distributions became available by Vardaci et al. [54] at low energies between 25 MeV and 39 MeV. $\sigma_{\rm reac}$ are provided in Table 2 of this work.

Overall, the data cover an energy range from 25 MeV to 63 MeV, corresponding to $E_{\rm red}$ from 0.77 MeV to 1.94 MeV. The results are shown in Figs. 8 and 9 with orange open squares. They are located in the middle of the bulk of weakly bound projectiles. Similar to the two previous projectiles ^{6}He and ^{6}Li, a strong α clustering component is found in the wave function of ^{7}Li = $\alpha + t$. The separation energy between the two clusters is 2.468 MeV, i.e. somewhat higher than in the case of ^{6}Li. Thus, slightly lower $\sigma_{\rm red}$ can be expected for ^{7}Li compared to ^{6}Li. This can be seen in the additional Figs. 12 and 13.

An interesting feature becomes visible in the plot of the ratios of $\sigma_{\rm red}/\sigma_{\rm red}(\alpha)$ in Fig. 13 which is not as obvious in the plot of $\sigma_{\rm red}$ in Fig. 12. There is a general trend of increasing ratios $\sigma_{\rm red}/\sigma_{\rm red}(\alpha)$ towards lower energies around $E_{\rm red} \approx 1$ MeV, very similar to the trend for ^{6}Li which can be seen in all data sets at these energies by Keeley, Martel, Parkar, Yang, and Vardaci. But at 27 MeV, corresponding to $E_{\rm red}$ = 0.83 MeV, a significant discrepancy appears between the relatively high $\sigma_{\rm red}$ = 0.59 mb by Parkar and the relatively low $\sigma_{\rm red}$ = 0.19 mb by Martel. (No parameters at 27 MeV are provided in the Keeley paper). The ratios to $\sigma_{\rm red}(\alpha)$ are about 5.2 for the Parkar $\sigma_{\rm red}$ and about 1.7 for the Martel $\sigma_{\rm reac}$. At 25 MeV, the data by Vardaci of $\sigma_{\rm reac}$ = 1.18 mb and $\sigma_{\rm red}$ = 0.019 mb indicate an even lower ratio of about 1.5 only. The error bars of the Vardaci angular distribution are very small, thus allowing to constrain $\sigma_{\rm reac}$ with an uncertainty of less than a factor of two. Thus, there is strong experimental evidence that the energy dependence of $\sigma_{\rm red}$ of ^{7}Li deviates significantly from ^{6}He and ^{6}Li. Unfortunately, the error bars of the Yang data at 25.7 MeV do not allow to determine $\sigma_{\rm reac}$ with a reasonable accuracy. The number which can be calculated from the given OMP parameters, is of the order of microbarns and thus far below the already low $\sigma_{\rm reac}$ from the Vardaci experiment. But the experimental angular distribution at 25.7 MeV can also be reproduced with χ^2/F below 1 with much higher $\sigma_{\rm reac}$ up to about 10 mb. This data point at 25.7 MeV is omitted in Figs. 12 and 13. Interestingly, the next-lowest data point by Yang at 28.6 MeV, corresponding to $E_{\rm red}$ = 0.88 MeV, shows a high ratio around 5.7 which is close to the ratio of Parkar at 27 MeV ($E_{\rm red}$ = 0.83 MeV) and above the ratio around 3.0–3.2 at 29 MeV ($E_{\rm red}$ = 0.89 MeV) from Keeley and Martel.

Summarizing the data for ^{7}Li, there is some tension between the experimental data sets towards low energies. But there is strong evidence for a significantly different energy

dependence of σ_{red} compared to ^{6}He and ^{6}Li, leading to much lower σ_{red} and ratios $\sigma_{red}/\sigma_{red}(\alpha)$ towards low E_{red} below about 0.8–0.9 MeV. At higher energies, the σ_{red} for ^{7}Li follow the general trend of weakly bound projectiles.

4.6 ^{208}Pb + ^{8}Li

Data for ^{208}Pb(^{8}Li,^{8}Li)^{208}Pb are available only by Kolata et al. [60]. Five angular distributions have been measured at energies between about 20 MeV and 25 MeV, corresponding to σ_{red} = 0.79 MeV to 1.07 MeV. The total reaction cross sections are provided in Table I of [60]. The data are shown with dark purple club symbols in Figs. 8 and 9. The results for σ_{red} for ^{8}Li exceed the σ_{red} of ^{6}Li and ^{7}Li, but remain below σ_{red} for ^{6}He. Such results are expected for ^{8}Li with its small neutron separation energy of 2.033 MeV. The energy dependence of σ_{red} for ^{8}Li shows the same increase towards low energies as ^{6}He and ^{6}Li. Contrary to ^{7}Li, no evidence for a decreasing ratio $\sigma_{red}/\sigma_{red}(\alpha)$ towards very low energies can be seen.

4.7 ^{208}Pb + ^{9}Li

Overall, four angular distributions have been measured by Cubero et al. for ^{208}Pb(^{9}Li,^{9}Li)^{208}Pb which are shown in Fig. 3 of [61] and Fig. 3 of [62]. The experiments cover only a limited energy range between 24 MeV and 33 MeV, corresponding to E_{red} = 0.74 MeV to 1.02 MeV. The data at EXFOR have been provided by the authors and have to be used for a re-analysis because total reaction cross sections are not given in [61,62]. A separate analysis was made for two angular distributions which were measured at the projectile energy of 29.5 MeV because two targets with different thicknesses were used, leading to effective energies of 29.28 MeV and 29.20 MeV. The results for σ_{red} of ^{9}Li from the present re-analysis are shown in Figs. 8 and 9 with brown open circles. Because the data for ^{9}Li are difficult to see in the bulk of data for weakly bound projectiles, the σ_{red} for ^{9}Li are also included in the separate Figs. 12 and 13. The data show a steep increase towards lower energies, similar to ^{6}He, ^{6}Li, and ^{8}Li, but different from ^{7}Li.

Outside the shown energy range of Figs. 8 and 9, one more angular distribution has been measured by Skobelev et al. [63] at $E_{c.m.}$ = 82 MeV, corresponding to E_{red} = 2.67 MeV. The resulting σ_{red} = 73.6 mb fits nicely into the general trend of weakly bound projectiles at higher energies with ratios $\sigma_{red}/\sigma_{red}(\alpha) \approx 1.5$ (as found above for ^{6}Li and ^{7}Li).

4.8 ^{208}Pb + ^{11}Li

Only few experimental data are available for ^{208}Pb (^{11}Li,^{11}Li)^{208}Pb elastic scattering. Two angular distributions at the energies of 29.6 MeV and 24.0 MeV were measured in [61], corresponding to σ_{red} = 0.76 MeV and 0.93 MeV. (Note that I have corrected the given energies in [61] by about 300 keV to take into account the energy loss of the ^{11}Li projectiles in the ^{208}Pb target with a thickness of 1.45 mg/cm^2.) It was found in [61] that elastic scattering of the neutron-halo projectile ^{11}Li shows a completely different angular distribution which deviates from the Rutherford cross section already at forward angles.

It is very difficult to find reasonable fits in the OM which describe the ^{11}Li elastic scattering data. Although the OMP parameters must remain quite uncertain under these conditions, it is nevertheless obvious that the resulting total reaction cross sections are huge because of the deviations of the angular distribution from Rutherford over a wide angular range. The obtained σ_{reac} are about 3900 mb at 24.0 MeV and 6200 mb at 29.6 MeV which translates to σ_{red} = 58 mb (93 mb) at E_{red} = 0.76 MeV (0.93 MeV). The ratios to the reference cross sections are huge with 57.5 at the upper energy (E_{red} = 0.93 MeV) and about 8600 at the lower energy (E_{red} = 0.76 MeV). The data are shown with lightblue full circles in Figs. 8 and 9. However, because of the huge numbers, only the lower data point is within the scale of Fig. 8 with the σ_{red}, and only the upper data point is within the scale of Fig. 9 with the ratio $\sigma_{red}/\sigma_{red}(\alpha)$. The huge slope of the ratio with more than two orders of magnitude between E_{red} = 0.76 MeV and 0.93 MeV exceeds the slope of other nuclei under study and reflects the extreme neutron-to-proton ratio and neutron halo properties of ^{11}Li.

4.9 ^{208}Pb + ^{7}Be

^{7}Be is the isospin mirror nucleus of ^{7}Li. Consequently, many similarities can be expected. ^{7}Be has also a noticable α-cluster structure as α + ^{3}He. The separation energy of the clusters is very low with 1.587 MeV, i.e. only about 2/3 of the separation energy in ^{7}Li which should also result in enhanced σ_{red}.

Experimentally, similar to the ^{7}Li case, there is a low-lying excited state in ^{7}Be at an excitation energy of 429 keV which complicates the measurement of elastic scattering because a high energy resolution is needed to separate the contributions of the $3/2^-$ ground state and the $1/2^-$ excited state. Furthermore, experiments with ^{7}Be are by far more complicated than with ^{7}Li because ^{7}Be is unstable.

Angular distributions of elastic scattering at low energies have been measured by Mazzocco et al. [64] at three energies between 37.4 MeV and 42.2 MeV which corresponds to E_{red} between 0.86 MeV and 0.98 MeV. Total reaction cross sections are provided in Table I of [64]. The resulting σ_{red} are shown in Figs. 8 and 9 as big filled orange diamonds. As expected, the σ_{red} for ^{7}Be are located in the bulk of weakly bound projectiles. The ratio $\sigma_{red}/\sigma_{red}(\alpha)$ increases towards lower energies, similar to the many previous cases except its

mirror ^{7}Li. The lowest energy E_{red} = 0.86 MeV for ^{7}Be is slightly above the energy range where the energy dependence of the σ_{red} data for ^{7}Li deviates from the typical behavior of weakly bound projectiles. Thus, it must remain an open question whether ^{7}Be will behave similar or different as its mirror ^{7}Li towards low energies.

Furthermore, the σ_{red} data for ^{7}Be are also included in the additional Figs. 14 and 15 which are mainly intended for a better visualization of the ^{9}Be and ^{10}Be data (see next Sects. 4.10 and 4.11).

4.10 ^{208}Pb + ^{9}Be

Elastic ^{208}Pb(^{9}Be,^{9}Be)^{208}Pb scattering at low energies was investigated experimentally in two studies. Woolliscroft et al. [65] have measured angular distributions between 38 MeV and 75 MeV, and Yu et al. [66] have complemented these data between 37 MeV and 50 MeV. Overall, data for reduced energies between 0.88 MeV and 1.75 MeV are available. In addition, Duan et al. [67] have measured recently an additional angular distribution at 88 MeV which corresponds to E_{red} = 2.06 MeV (slightly outside the shown range in Figs. 8 and 9).

Although neither Woolliscroft et al. nor Yu et al. provide the total reaction cross sections σ_{reac} from their fits, a subsequent analysis by Palli et al. [68] re-fits all angular distributions and lists the resulting σ_{reac} in their Table I. The derived σ_{red} for ^{9}Be are shown in Figs. 8 and 9 with light-blue heart symbols. The additional Figs. 14 and 15 illustrate the data for ^{7}Be, ^{9}Be, and ^{10}Be.

The nucleus ^{9}Be has a strong $\alpha + \alpha + n$ cluster structure where the neutron is only weakly bound by 1.665 MeV. Consequently, enhanced σ_{red} can be expected. Indeed, the σ_{red} for ^{9}Be are located in the bulk of weakly bound projectiles in Figs. 8 and 9. Towards higher energies, the σ_{red} are a factor of 1.3–1.4 above the reference calculation. Towards lower energies, the ratios $\sigma_{red}/\sigma_{red}(\alpha)$ for ^{9}Be increase in the usual way for weakly bound projectiles. There is a minor difference between the two data sets. The σ_{red} from Yu et al. are slightly higher than the σ_{red} from Woolliscroft et al. towards the lowest energies; otherwise, the two data sets agree well. And also the σ_{red} from the 88 MeV data of Duan et al. with σ_{red} = 38.6 mb and a ratio $\sigma_{red}/\sigma_{red}(\alpha)$ = 1.20 at E_{red} = 2.06 MeV fits nicely into the general trend of the data for ^{9}Be.

4.11 ^{208}Pb + ^{10}Be

The ^{208}Pb(^{10}Be,^{10}Be)^{208}Pb reaction was studied at low energies by Kolata et al. [28]. Five angular distributions at energies between 38.4 MeV and 43.9 MeV are shown in Fig. 1 of [28]. Total reaction cross sections from different OM fits are provided in Table I of [28]. However, it is noted in [28] that the angular distributions at the two lowest energies show only tiny deviations from the Rutherford cross section, and thus the obtained σ_{reac} from the OM fits have significant uncertainties. Consequently, σ_{reac} with larger uncertainties are shown in Fig. 2 of [28]. As also discussed above in Sect. 3.3, the two OM fits by Kolata et al. at the lowest energy of 38.4 MeV provide σ_{reac} = 3 mb or 10 mb. Their Fig. 2 shows σ_{reac} with a larger error bar, with a lower end exceeding the lower range of the diagram at 1 mb, and an upper end around 40 mb. I adopt these results from Fig. 2 of [28] although my re-fits in Sect. 3.3 indicate that the upper limit may be even higher at 80 mb or 150 mb, depending on the choice of the re-digitized data either from NRV or from EXFOR.

The σ_{red} from ^{208}Pb(^{10}Be,^{10}Be)^{208}Pb scattering cover an energy range between E_{red} = 0.90 MeV and 1.03 MeV. The σ_{red} for ^{10}Be are shown in Figs. 8 and 9 with dark cyan filled diamonds. Interestingly, the data for the three upper energies are located at the lower end of weakly bound projectiles although ^{10}Be is tightly bound with a neutron separation energy of 6.8 MeV, proton separation energy of 19.6 MeV, and α separation energy of 7.4 MeV. The ratio to the reference calculation is about 1.5–1.7 for the three upper energies. Contrary, the σ_{red} at the two lowest energies are much lower, with ratios of about 0.17 and 0.30 at E_{red} = 0.90 MeV and 0.92 MeV. The original error bar of Kolata et al. ends below a ratio of 1.0, but from my additional analysis the ratio may be up to a factor of 4 higher. Thus, the available experimental data point towards lower σ_{red} at low energies and towards a different energy dependence for the σ_{red} for ^{10}Be (compared to several weakly bound projectiles like ^{6}He, ^{6}Li, ^{7}Li, ^{7}Be, ^{9}Be). But unfortunately the uncertainties for σ_{red} are too large to come to a clear conclusion on the energy dependence of σ_{red} for ^{10}Be. Interestingly, the low σ_{red} for ^{10}Be at the lowest energies nicely match the results for several tightly bound projectiles which will be discussed later in this study.

4.12 ^{208}Pb + ^{11}Be

Elastic scattering data for ^{208}Pb(^{11}Be,^{11}Be)^{208}Pb at low energies around the Coulomb barrier are not available in literature. Because of the low neutron separation energy of 502 keV and because of $J^{\pi} = 1/2^{+}$ of the ground state of ^{11}Be, this nucleus can be expected to show strongly enhanced σ_{red} because of its pronounced neutron halo properties. As some data are available at higher energies, we briefly discuss the results above the usual energy range of the present study.

Duan et al. [67] have measured angular distributions for ^{11}Be, ^{10}Be, and ^{9}Be scattering from ^{208}Pb. The respective energies were 140 MeV for ^{11}Be, 127 MeV for ^{10}Be, and 88 MeV for ^{9}Be. Total cross sections of 7798 mb, 3067 mb, and 2473 mb are reported in [67], leading to the following results for σ_{red} in Table 1. The data are complemented by another data sets at higher energies for ^{7}Be by Yang et al. [69] and Wang et al. [70]. Although the E_{red} of the different data sets at

higher energies do not match exactly, the σ_{red} vs. E_{red} curve is sufficiently flat at these energies, and thus a comparison of the ratios $\sigma_{red}/\sigma_{red}(\alpha)$ in Table 1 clearly reveals that the σ_{red} for ^{11}Be is far above the σ_{red} for ^{7}Be, ^{9}Be, and ^{10}Be which show the typical behavior of weakly bound projectiles with ratios above 1.0 but below about 1.5 (see also Fig. 9). A similar enhancement of σ_{red} of ^{11}Be (compared to ^{9}Be and ^{10}Be) can be derived from low-energy scattering data on ^{64}Zn [71]. This finding strenghtens the interpretation of ^{11}Be as a neutron halo nucleus (e.g., [71,72]).

For completeness I mention another recent experiment at relatively high energies where angular distributions for ^{208}Pb(^{12}B,^{12}B)^{208}Pb and ^{208}Pb(^{12}N,^{12}N)^{208}Pb elastic scattering were measured by Wang et al. [73]. Both odd-odd nuclei, ^{12}B and ^{12}N, are relatively weakly bound with a low neutron separation energy of 3370 keV for ^{12}B and a very low proton separation energy of 600 keV for ^{12}N. The total reaction cross sections σ_{reac} from the angular distributions at E = 255 MeV for ^{12}B and 343 MeV for ^{12}N are given by Wang et al. as about 3600 mb in both cases, leading to $\sigma_{red} \approx$ 53 mb at E_{red} = 4.77 MeV for ^{12}B and E_{red} = 4.64 MeV for ^{12}N. This result is less than a factor of two above the reference calculation, i.e. close to the typical values for weakly bound and exotic halo projectiles. This underlines the extraordinary properties of ^{11}Be where a much higher σ_{red} above 100 mb was found already at the slightly lower E_{red} = 3.30 MeV (see Table 1).

4.13 ^{208}Pb + ^{8}B

^{8}B is the isospin mirror nucleus of ^{8}Li. The proton separation energy of ^{8}B is as low as 136 keV which is even below the relatively small neutron separation energy of its mirror ^{8}Li of 2.033 MeV. There is only one angular distribution of ^{208}Pb(^{8}B,^{8}B)^{208}Pb elastic scattering at low energies by Mazzocco et al. [64] at 50 MeV which corresponds to E_{red} = 0.93 MeV. The total reaction cross section σ_{reac} is provided in Table I of [64]. The resulting σ_{red} is shown in Figs. 8 and 9 as open light-blue diamond. This σ_{red} for ^{8}B shows a strong enhancement close to the results for its mirror nucleus ^{8}Li and the neutron halo nucleus ^{6}He, thus indicating the proton halo of ^{8}B.

Somewhat surprisingly, at higher energies between E_{red} = 3.17 MeV and 4.43 MeV, σ_{red} between 53 mb and 55 mb were derived in [69,70,74] which is only moderately enhanced and corresponds to ratios $\sigma_{red}/\sigma_{red}(\alpha)$ of about 1.4, in line with the overall results for many weakly bound projectiles (see Fig. 9).

Very recently, an angular distribution of elastic ^{8}B scattering on a natural zirconium target was measured at 26.5 MeV by Palli et al. [75]. The total reaction cross section of σ_{reac} = 180 ± 40 mb translates to about σ_{red} = 4.3 mb at E_{red} = 0.79 MeV and a ratio $\sigma_{red}/\sigma_{red}(\alpha)$ of about 150; i.e., all data for ^{8}B at low E_{red} are close to the data for the ^{8}Li mirror nucleus.

4.14 ^{208}Pb + ^{11}B

Contrary to ^{8}B, the nucleus ^{11}B is stable and tightly bound with neutron and proton separation energies above 11 MeV, and also the cluster separation energies of an $\alpha + \alpha + t$ structure are 8.7 MeV and 11.2 MeV for the α and the triton. Thus, ^{11}B can be considered as a typical example for a tightly bound nucleus, independent of a possible cluster structure. From a shell model point of view, ^{11}B consists of the tightly bound ^{12}C with one proton hole in the $p_{3/2}$ shell, also without any evidence for a weak binding.

There is one angular distribution of ^{208}Pb(^{11}B,^{11}B)^{208}Pb elastic scattering in literature by Sahu et al. [76] at 69 MeV. The data cover only a limited angular range of 45° to 75°. The total reaction cross section of σ_{reac} = 1302 mb in Table I of [76] corresponds to σ_{red} = 19.6 mb at E_{red} = 1.30 MeV. The ratio to the reference calculation is $\sigma_{red}/\sigma_{red}(\alpha)$ = 1.10, i.e. close to unity within 10%. A similar result is found from the earlier experiment by Ford et al. [77] at the slightly higher energy of 72.2 MeV. The results for ^{11}B are shown in Figs. 8 and 9 with a light-brown dotted circle.

4.15 ^{208}Pb + ^{10}C

The very proton-rich (N/Z = 0.667) even-even nucleus ^{10}C is moderately bound with a proton separation energy of 4.0 MeV and α separation energy of 5.1 MeV. Recently, Linares et al. [78] have measured an angular distribution of ^{208}Pb(^{10}C,^{10}C)^{208}Pb elastic scattering at 66 MeV. The total reaction cross section from an OM fit is given as σ_{reac} = 753 mb, corresponding to σ_{red} = 11.5 mb at E_{red} = 1.03 MeV.

The data point for ^{10}C is shown in Figs. 8 and 9 with a ⊕ symbol in light orange color. The data point is located at the lower end of the bulk of weakly bound projectiles, and is almost hidden behind two close-lying results for ^{19}F (see also Sect. 4.24). From the separation energies of ^{10}C, such an enhanced σ_{red} is somewhat unexpected. However, the original analysis in [78] using the so-called universal fusion function (UFF) shows an even more pronounced enhancement of the ^{10}C cross section (see Fig. 5 in [78]). A slightly enhanced σ_{red} for ^{10}C is also observed at higher energies where Yang et al. [79] report σ_{red} = 51.4 mb at E_{red} = 3.54 MeV, corresponding to a noticably enhanced ratio $\sigma_{red}/\sigma_{red}(\alpha)$ = 1.33.

4.16 ^{208}Pb + ^{12}C

Elastic scattering for the ^{208}Pb(^{12}C,^{12}C)^{208}Pb reaction was investigated experimentally in several studies. A broad range of energies was covered by Santra et al. [80]. Overall, seven angular distributions were measured at energies between 58.9

MeV and up to 84.9 MeV, and the derived σ_{reac} are listed in Table I of [80]. In addition, earlier data at 118 MeV by Friedman et al. [81] were re-analyzed in [80], leading to σ_{reac} close, but slightly lower by less than 5%, than the original analysis in [81]. An earlier experiment by Ball et al. [82] shows an angular distribution between 20° and 75° at the energy of 96 MeV. The total reaction cross section was derived from various fits, leading to $\sigma_{reac} = 1754 - 1869$ mb; from the scatter of the derived σ_{reac}, I adopt $\sigma_{reac} = 1810 \pm 58$ mb. Angular distributions at relatively low energies between 54.5 MeV and 57.0 MeV are reported by Gasques et al. [83]. As σ_{reac} are not provided in [83], I have re-fitted the data which are available at EXFOR. Another angular distribution is available in Rudakov et al. [84] at 75.7 MeV. Here the EXFOR data were re-fitted which are taken from a numerical table including the uncertainties. The total cross section σ_{reac} at 116.4 MeV is derived from the experiment by Larsen et al. [85]. Because the information in [85] is very limited, σ_{reac} is re-calculated from the OMP parameters of a subsequent analysis of the Larsen et al. data by the same group in Ford et al. [77]. Finally, early angular distributions are available at 122.8 MeV by Kerlee et al. [86] and at 125.3 MeV by Baker et al. [87]. For a brief discussion of the data analysis in [87], see Sect. 4.19.

The above mentioned angular distributions cover the energy range of E_{red} from 0.88 MeV to 1.98 MeV. The resulting σ_{red} are shown with brown stars in Figs. 8 and 9. For better visualization of the individual experiments, two further Figs. 16 and 17 have been added.

The σ_{red} from the different ^{12}C scattering data are nicely consistent and agree well with the reference data from α scattering at higher energies above $E_{red} \approx 1$ MeV within deviations of less than 15%. However, an unexpected deviation between the ^{12}C data and the reference data is found below $E_{red} \approx 1$ MeV where low ratios $\sigma_{red}/\sigma_{red}(\alpha)$ down to about 0.05 are found at $E_{red} = 0.88$ MeV to 0.89 MeV. The extremely low ratios are based on the re-fits of the experimental data of Gasques et al. only, but also the lowest data point by Santra et al. at $E_{red} = 0.93$ MeV clearly shows a ratio far below 1.0 with $\sigma_{red}/\sigma_{red}(\alpha) = 0.158 \pm 0.025$. Similar low ratios to the reference $\sigma_{red}(\alpha)$ will be found in several further data for tightly bound projectiles (see below).

4.17 ^{208}Pb + ^{13}C

Experimental data for ^{208}Pb(^{13}C,^{13}C)^{208}Pb elastic scattering are very scarce. Franey et al. [88] have measured transfer reactions on ^{208}Pb at sub-Coulomb energies. They pointed out that the elastic angular distributions were mainly measured "as justification for using Coulomb distorted waves in the analyses of transfer reactions". Accordingly, the measured angular distributions at 52 MeV and at 54 MeV (E_{red} = 0.82 MeV and 0.86 MeV) consist only of few data points, and the deviations from the Rutherford cross section remain below 10%. I have tried to re-fit these angular distributions by adopting the OMP parameters of Santra et al. [80] and by re-adjusting only the diffuseness of the imaginary OMP. The obtained σ_{reac} and σ_{red} show significant uncertainties, and thus the data are only shown in Figs. 16 and 17. Despite the uncertainties of roughly a factor of two for σ_{reac}, is seems that the data for ^{13}C are located slightly above the reference calculation with $\sigma_{red}/\sigma_{red}(\alpha) \approx 2$ around $E_{red} \approx 0.84$ MeV. These σ_{red} are much higher than for the tightly bound ^{12}C, but also much lower than the results for weakly bound projectiles. The neutron separation energy of ^{13}C is 4.946 MeV which is neither tightly nor weakly, but moderately bound.

4.18 ^{208}Pb + ^{15}C

A preliminary analysis of a recent ^{208}Pb(^{15}C,^{15}C)^{208}Pb scattering experiment at the HIE-ISOLDE facility in CERN is given by Ovejas et al. [89]. A total reaction cross section of σ_{reac} = 3035 mb was found at 65 MeV, corresponding to a reduced cross section σ_{red} = 43.1 mb at E_{red} = 1.03 MeV. The result is shown as a big blue star in Figs. 8, 9, 16, and 17. The obtained σ_{red} for ^{15}C is even slightly above the results for the neutron halo nucleus ^{6}He. It will be interesting to see whether the final analysis of the data will confirm this result, but the dramatic differences between the angular distributions of ^{208}Pb(^{12}C,^{12}C)^{208}Pb and ^{208}Pb(^{15}C,^{15}C)^{208}Pb scattering in Fig. 3 of [89] clearly show that σ_{reac} for ^{15}C is strongly enhanced.

The neutron binding energy in the neutron-rich ^{15}C nucleus is tiny with 1.218 MeV, and furthermore the spin and parity of $J^{\pi} = 1/2^{+}$ indicate that the ground state wave function has a strong ^{14}C + n component with a s-wave ($L = 0$) neutron halo. Consequently, the obtained huge σ_{red} for ^{15}C is not surprising.

4.19 ^{208}Pb + ^{14}N

One angular distribution for ^{208}Pb(^{14}N,^{14}N)^{208}Pb has been measured in literature by Baker et al. [87] at 146.7 MeV already in 1967. Instead of an OM fit, Baker et al. use a simple parametrization of the S-matrix and fit the parameters to their experimental angular distribution. The reflexion coefficients η_L are essentially characterized by the range of angular momenta L where the η_L change from almost zero (full absorption for low L, corresponding to central collisions) to almost one (no absorption for high L, corresponding to peripheral collisions). The given formula for the η_L in [87] allows to recalculate the total reaction cross section σ_{reac} from Eq. (3).

Baker et al. have measured angular distributions for ^{12}C, ^{14}N, and ^{16}O for energies close to $E_{red} = 2$ MeV. In all cases, the ratio to the reference calculation $\sigma_{red}/\sigma_{red}(\alpha)$ is between

1.14 and 1.18, see Fig. 8 and 9. An earlier experiment for ^{208}Pb(^{14}N,^{14}N)^{208}Pb by Kerlee et al. [86] at almost the same energy of 147.2 MeV finds a slightly lower σ_{reac}, leading to a ratio $\sigma_{red}/\sigma_{red}(\alpha) = 1.05$ at $E_{red} = 2.003$ MeV (i.e., outside Figs. 8 and 9).

4.20 ^{208}Pb + ^{16}O

^{16}O is a doubly-magic, tightly bound nucleus with proton and neutron separation energies above 12 MeV. And also the α separation energy is not very low with 7.162 MeV. A series of experimental angular distributions for ^{208}Pb(^{16}O,^{16}O)^{208}Pb is available in literature which makes ^{16}O, together with ^{12}C and the α particle, another paradigm for a tightly bound projectile in the present study.

A series of angular distributions was measured by Videbaeck et al. [90] between 80 MeV and 102 MeV. The derived σ_{reac} are listed in their Table II from different OM fits. The average and standard deviation have been adopted. These data have been complemented by Vulgaris et al. [30,31] between 78 MeV and 90 MeV. Here σ_{reac} are provided in their Table III without uncertainties. An extension towards lower energies was provided by Silva et al. [32] who measured angular distributions between 74 MeV and 78 MeV. Unfortunately, Silva et al. do not provide σ_{reac}, and the limited information on the chosen potentials does not allow to re-calculate σ_{reac} from the original analysis. So I have used the data at EXFOR to re-fit the angular distributions and to determine σ_{reac}. Pieper et al. [91] have measured two angular distributions in the energy range of the present study at 104 MeV and 138.5 MeV. The obtained σ_{reac} are not listed in [91], but can be re-calculated from the OMP parameters in their table IV (best-fit set "I3"). In addition to the above experiments which provided many angular distributions, the following studies show one additional angular distribution. The experiment by Baker et al. [87] at 158 MeV or $E_{red} = 2.03$ MeV is marginally above the chosen energy range of the present study, but fits into the general trend of the σ_{red} data with a ratio $\sigma_{red}/\sigma_{red}(\alpha) = 1.14$. Ball et al. [82] show data at 129.5 MeV and 192 MeV (the latter with $E_{red} = 2.30$ MeV outside the chosen energy range, but with $\sigma_{red}/\sigma_{red}(\alpha) = 1.20$ close to the data at lower E_{red}). The σ_{reac} are provided in their Table 2 from different OM fits. Becchetti et al. [92] have measured elastic scattering at 104 MeV, and σ_{reac} can be re-calculated from the OMP parameters in a footnote of their Table I. The same holds for the angular distribution at 130 MeV by Friedman et al. [81]; here in addition a parametrized phase shift fit was made, leading to practically the same σ_{reac} within less than 1%. A third angular distribution at 78 MeV is measured by Lilley et al. [29]. For a discussion of these three measurements at 78 MeV, see above Sect. 3.4. Finally, the angular distribution by Rudakov et al. [84] at 95 MeV was re-fitted using the original data which are available at EXFOR.

Overall, the available angular distributions cover a wide range of energies from 74 MeV up to almost 200 MeV, corresponding to E_{red} from 0.88 MeV up to more than 2.0 MeV. The resulting σ_{red} are shown in Figs. 8 and 9 with light-red $\otimes$ symbols. For better visualization, the data for the oxygen isotopes are shown also in the additional Figs. 18 and 19.

In general, the agreement between the different experimental data sets is very reasonable. Typical uncertainties have been illustrated above in Sect. 3.4. Below $E_{red} \approx 1$ MeV, a major deviation between the data for ^{16}O and the reference data from the α particle is found, leading to ratios $\sigma_{red}/\sigma_{red}(\alpha)$ far below unity, reaching values of only about 0.02 at $E_{red} \approx 0.9$ MeV. Although the uncertainties of the derived σ_{reac} and σ_{red} increase towards lower energies, the overall good agrement between the different experiments for ^{16}O shows that these unexpectedly small σ_{red} are an experimental fact. Furthermore, this finding is very similar to the results for ^{12}C, see Sect. 4.16 and Figs. 16 and 17. Although the low-energy data by Franey et al. [88] do not allow to determine σ_{reac} with reasonable accuracy, upper limits for σ_{reac} can be derived from the angular distributions at 69.05 MeV, 70.95 MeV, and 72.95 MeV. Thes upper limits confirm the trend towards ratios $\sigma_{red}/\sigma_{red}(\alpha) < 1.0$ at low energies for ^{16}O.

4.21 ^{208}Pb + ^{17}O

Only few data are available for ^{208}Pb(^{17}O,^{17}O)^{208}Pb elastic scattering. Lilley et al. [29] show an angular distribution at 78 MeV, and σ_{reac} was determined by a careful analysis of OM fits (see their Table 1, similar to ^{16}O above). Torresi et al. [93] show six angular distributions at energies between 50 MeV and 87 MeV. Unfortunately, the angular distributions cover only a very limited angular range, and at the lower energies the deviation from the Rutherford cross section is tiny. Torresi et al. provide directly the reduced cross sections σ_{red} in their Fig. 2 for their three highest energies of 82 MeV, 84 MeV, and 87 MeV; here I use these three data points (re-digitized). Finally, an angular distribution at 66.95 MeV has been measured by Franey et al. [88], but also here the deviation from Rutherford is too small to allow for a determination of the total reaction cross section σ_{reac}. The upper limit from the Franey et al. angular distribution is far above the ratio $\sigma_{red}/\sigma_{red}(\alpha) = 1.0$, thus not constraining the low-energy behavior of σ_{red} for ^{17}O.

The obtained σ_{red} data for ^{17}O cover reduced energies E_{red} between 0.94 MeV and 1.04 MeV. The data are shown in Figs. 8 and 9 with small pink filled diamonds. The lowest data point from the Lilley et al. angular distribution is clearly below the reference data with $\sigma_{red}/\sigma_{red}(\alpha) \approx 0.68$, and also the three σ_{red} from the Torresi et al. experiment show a trend

of decreasing ratios $\sigma_{red}/\sigma_{red}(\alpha)$ towards lower E_{red} although the deviations from unity are small at these E_{red} around 1 MeV. It seems that the σ_{red} data for ^{17}O are close to the results for ^{12}C and ^{16}O, but the deviation from the reference data is probably somewhat less pronounced than in the ^{12}C and ^{16}O cases.

The neutron separation energy of ^{17}O is moderately low with 4.143 MeV which is even lower than for ^{13}C with 4.946 MeV. Thus, it is somewhat surprising to see that the σ_{red} data for ^{17}O show ratios $\sigma_{red}/\sigma_{red}(\alpha)$ smaller than unity, whereas the σ_{red} for ^{13}C show ratios above unity at low energies. However, the experimental data in both cases show significant uncertainties. Better experimental data are required for a robust conclusion whether ^{13}C and ^{17}O show similar or discrepant σ_{red} towards low energies.

4.22 ^{208}Pb + ^{18}O

Vulgaris et al. [30,31] have measured five angular distributions at energies between 78 MeV and 86 MeV. At higher energies, an angular distribution is available at 120 MeV by Gross et al. [94]. In both studies, various OM fits have been made to estimate σ_{reac}, and the results are provided in Table III of [31] and Table I of [94]. The resulting σ_{red} cover the energy range of E_{red} between 0.94 MeV and 1.44 MeV and are shown in Figs. 8 and 9 with olive $\ominus$ symbols. Another angular distribution at the low energy of 66.95 MeV, measured by Franey et al. [88], deviates only marginally from the Rutherford cross section and unfortunately does not allow to determine σ_{reac}. An upper limit of about 30 mb can be estimated which corresponds to $\sigma_{red} \leq 0.4$ mb at $E_{red} = 0.80$ MeV which is about a factor of 10 above the reference calculation. No relevant information can be obtained from this upper limit.

For better visualization, the data for ^{18}O are also shown in Figs. 18 and 19. The upper limit from the Franey et al. angular distribution is included in Fig. 18; it is located outside the shown range of Fig. 19.

The data by Vulgaris et al. indicate that the σ_{red} for ^{18}O behave almost similar to ^{16}O and ^{12}C, i.e. showing a significantly decreasing ratio $\sigma_{red}/\sigma_{red}(\alpha)$ towards lower energies below $E_{red} \approx 1$ MeV. On the one hand, such a behavior can be expected from the relatively high proton and neutron separation energies of ^{18}O. On the other hand, the ^{18}O structure with two neutrons outside the doubly-magic ^{16}O core, could also lead to some enhancement for σ_{red} because of two-neutron transfer reactions which may be seen from the slightly high σ_{red} from the Gross et al. experiment at the higher energy $E_{red} = 1.44$ MeV.

The low σ_{red} for ^{18}O are confirmed by a re-analysis of the Vulgaris et al. data at 86 MeV by Aygun et al. [95]. The re-analysis finds $\sigma_{reac} = 475.5$ mb or 413.0 mb using either WS or double-folding potentials. Averaging both results leads to $\sigma_{reac} = 444 \pm 31$ mb which is about 7% lower than the original analysis with $\sigma_{reac} = 479$ mb. One should keep in mind that the given uncertainty of 31 mb from the deviation of the two OM fits may underestimate the real uncertainty (as discussed in Sect. 3.2).

4.23 ^{208}Pb + ^{17}F

^{17}F is the isospin mirror nucleus of ^{17}O. The proton separation energy of ^{17}F of only 600 keV is far lower than the neutron separation energy of ^{17}O. But it has been pointed out that a pronounced proton halo appears only for the first excited state in ^{17}F ($1/2^+$ at 495 keV, proton s-wave), but not for the ground state ($5/2^+$, proton d-wave) [96]. Thus it is interesting to see how the σ_{red} for ^{17}F will behave at low energies.

Much experimental efforts have been spent to measure angular distributions for ^{208}Pb(^{17}F,^{17}F)^{208}Pb elastic scattering. One angular distribution at 86 MeV was measured by Signorini et al. [97], and the two earlier angular distributions at 90.4 MeV and 98.0 MeV by Romoli et al. [98] were re-analyzed. Here I adopt the σ_{reac} from Table 1 of [97]. Liang et al. [99] provide data at 120 MeV, but the result for σ_{reac} can only be found in the above mentioned Table 1 of [97]. An earlier experiment by Liang et al. [100] shows an angular distribution at 170 MeV. Here σ_{reac} can be recalculated from the given OMP parameters. Recently, a new angular distribution at 94.5 MeV became available by Rong et al. [101]. As σ_{reac} is not given in [101], the data at EXFOR were re-fitted, and $\sigma_{reac} = 323$ mb was determined. Another re-analysis by Heo et al. [102] shows slightly higher results for σ_{reac} at 98 MeV by about 30% and similar results within about 10% at 120 MeV and 170 MeV.

The data for ^{17}F cover reduced energies E_{red} between 0.92 MeV and 1.81 MeV; the data are shown in Figs. 8 and 9 with pink open diamonds. For better visualization, the data for ^{17}F are also included in Figs. 20 and 21 for ^{19}F (see next Sect. 4.24). Obviously, the data for ^{17}F follow the general trend of low ratios $\sigma_{red}/\sigma_{red}(\alpha)$ towards low energies, similar to its isospin mirror ^{17}O and also similar to the tightly bound ^{12}C and ^{16}O projectiles. Despite the very low proton separation energy, there is no evidence for an enhancement of σ_{red} for ^{17}F.

4.24 ^{208}Pb + ^{19}F

Somewhat surprising, the situation for ^{19}F is worse than for most other cases under study although ^{19}F is a stable nucleus and ^{208}Pb(^{19}F,^{19}F)^{208}Pb experiments can be made with standard techniques. The only experiment in literature by Lin et al. [103] provides six angular distributions over a wide angular range at energies between 88 MeV and 102 MeV which corresponds to E_{red} from 0.94 MeV to 1.09 MeV. The total

reaction cross section σ_{reac} is listed in Table I of [103]. The results are shown in Figs. 8 and 9 with small full brown circles.

The data for ^{19}F are located close to the results for the weakly bound ^{6}Li. At first view, this seems to indicate that ^{19}F behaves like a weakly bound projectile although the proton and neutron separation energies are high with 7994 keV and 10,432 keV. The lowest separation energy is $S_\alpha = 4014$ keV which is still far above the smaller separation energies of the typical weakly bound projectiles.

A closer look sheds some doubt on this interpretation. The experimental data by Lin et al. did not resolve the three very low-lying excited states in ^{19}F which are the $1/2^+$ ground state, the $1/2^-$ state at 110 keV with its pronounced α-cluster structure, and the $5/2^+$ state at 197 keV. Lin et al. point out that they use phenomenological optical potentials but they use a coupled-channels code and take into account the coupling to the $5/2^+$ state at 197 keV. The $1/2^-$ state was excluded in the calculations because of its different structure. It remains unclear from the paper which coupling between the $1/2^+$ and $5/2^+$ states was applied and which ratio between the $1/2^+$ ground state and the $5/2^+$ state resulted from the coupling. Furthermore, it is not clear whether the shown curves in their Fig. 2 (called "optical model fits by the ECIS code") correspond to the $1/2^+$ ground state only or to the sum of $1/2^+$ ground state at $5/2^+$ excited state.

Grineviciute and Descouvemont [33] applied a microscopic continuum discretized coupled-channels model to the ^{208}Pb(^{19}F,^{19}F)^{208}Pb scattering data, and they conclude that the "theoretical inelastic contribution to the quasielastic scattering data is small" (as measured by Lin et al.). Thus, a standard OM fit (i.e., without coupling to excited states) should provide a reasonable estimate for σ_{reac}. Note that the σ_{reac} from the pure OM fits will be lower because the elastic cross section is assumed to contribute by 100% to the experimental angular distribution and is thus higher than in the calculation by Lin et al. Indeed much lower σ_{reac} were found in subsequent OM analyses of the Lin et al. data by Romoli et al. [98], Aygun [104], and El-Hammamy et al. [105], although this interesting result was not discussed in the latter studies. As the latter studies cover only a part of the angular distributions by Lin et al., I have re-fitted all angular distributions which are available at NRV. The results from these new fits nicely overlap with the later OM fits, but are much lower than the original σ_{reac} by Lin et al. The results are shown in the additional Figs. 20 and 21.

It becomes obvious from Figs. 20 and 21 that the original σ_{red} data by Lin et al. are above the reference calculation and show the typical energy dependence for weakly bound projectiles with a strong increase of the ratio $\sigma_{red}/\sigma_{red}(\alpha)$ towards lower energies. Contrary, the re-analysis by an OM fit to the same experimental data favors that the σ_{red} of ^{19}F are lower than the reference calculation, and the difference increases towards lower energies. A clear conclusion for ^{19}F can only be drawn from additional σ_{red} data at lower and higher energies. This calls for further experiments on ^{208}Pb(^{19}F,^{19}F)^{208}Pb elastic scattering with excellent energy resolution to distinguish between the contributions from the low-lying excited states in ^{19}F.

4.25 ^{208}Pb + ^{17}Ne

The nucleus ^{17}Ne has a low proton separation energy of 1469 keV and thus maybe another candidate for enhanced σ_{red} towards low energies. Furthermore, the two-proton separation energy is even lower with 933 keV. Very recently, an angular distribution of ^{208}Pb(^{17}Ne,^{17}Ne)^{208}Pb elastic scattering was measured by Ovejas et al. [106] at 136 MeV, corresponding to E_{red} = 1.28 MeV. Note that I have used an effective energy in the center of the target which is 2.5 MeV lower the than incoming energy of 136 MeV because of the energy loss of the ^{17}Ne projectiles in a 1.2 mg/cm^2 target which is rotated by about 60° (see experimental details in [106]). This shifts E_{red} down from 1.30 MeV to 1.28 MeV. The ratio $\sigma_{red}/\sigma_{red}(\alpha)$ = 1.46 is slightly enhanced but very close to the results for the neighboring projectile ^{20}Ne in the next Sect. 4.26. The result is shown in Fig. 8 and 9 with a full red square.

Interestingly, the obtained ratio $\sigma_{red}/\sigma_{red}(\alpha)$ for ^{17}Ne is almost identical to ^{20}Ne whereas the ratio is slightly lower by about 20% than for ^{22}Ne (see Secs. 4.26 and 4.27). The results for the different neon isotopes are shown in enlarged scale in Figs. 22 and 23.

A very recent re-analysis of the Ovejas et al. data by Heo et al. [108] derives a slightly higher total reaction cross section σ_{reac}. However, σ_{reac} is only increased by 3% to 5%, depending on the choice of OMP parameters. This corresponds to the expected uncertainties of σ_{reac} at energies slightly above the Coulomb barrier (as also discussed in Sect. 3.1 and 3.2).

4.26 ^{208}Pb + ^{20}Ne

Similar to ^{19}F, the proton and neutron separation energies of ^{20}Ne are high with 12,843 keV and 16,855 keV, and the separation energy of the α-particle is relatively low with 4730 keV. Unfortunately, the available data for ^{208}Pb(^{20}Ne,^{20}Ne)^{208}Pb elastic scattering are not sufficient to determine the low-energy behavior of σ_{red} below $E_{red} \approx 1$ MeV, and thus no strong conclusion can be drawn on the relevance of the low α separation energy for σ_{red} of ^{20}Ne.

An early experiment by Kerlee et al. [86] has measured an angular distribution at 206.2 MeV, i.e. at the upper end of the energy range of this work. A later experiment by Ball et al. [82] at 161.2 MeV provides the OMP parameters to re-calculate σ_{reac} for ^{20}Ne. Another experiment was done at 130.9 MeV by Gross et al. [109], but neither total reaction

cross sections nor the parameters of the OMP for the pure OM calculation are provided in [109]. A recent experiment on ^{17}Ne has shown these data for comparison, and σ_{reac} = 1817 mb is given in [106]. A re-fit of the data by Gross et al. resulted in an almost identical result of σ_{reac} = 1786 mb. There are two further angular distributions at the lower energies of 108.6 MeV and 115.0 MeV by Strojek et al. [110]. Unfortunately, the energy resolution of that experiment was not sufficient to resolve the ground state contribution and the contribution of the first excited state of ^{20}Ne with $J^\pi = 2^+$, $E^* = 1.63$ MeV, and only quasi-elastic angular distributions are shown in Figs. 2 and 3 of [110].

A further attempt to constrain the low-energy behavior of σ_{red} for ^{20}Ne is made using the data by Tripathi et al. [107]. They have measured partial cross sections of many exit channels of ^{20}Ne-induced fusion with ^{208}Pb at 114.4 MeV. As pointed out in the Introduction, this summed partial cross sections can provide only a lower limit because of additional contributions of unobserved channels. The result from the Tripathi et al. data in their Table II is 382.8 mb, leading to σ_{red} = 5.1 mb at E_{red} = 1.10 MeV which corresponds to a ratio $\sigma_{red}/\sigma_{red}(\alpha)$ of about 0.5; thus, this lower limit cannot provide further insight into the low-energy behavior of σ_{red} for ^{20}Ne.

The results for ^{20}Ne are shown in Figs. 8 and 9 with blue full triangles. A more detailed view is added in Figs. 22 and 23. Summarizing the findings for ^{20}Ne, σ_{red} could be determined only at three energies between 130.9 MeV and 206.2 MeV, corresponding to reduced energies E_{red} between 1.26 MeV and 1.98 MeV. The behavior of σ_{red} below E_{red} = 1 MeV cannot be constrained from the available angular distributions, and also the study of the fusion data by Tripathi et al. provides only a lower limit and cannot give further information on the low–energy behavior of σ_{red} for ^{20}Ne.

4.27 ^{208}Pb + ^{22}Ne

Contrary to the two previously studied neon isotopes ^{17}Ne and ^{20}Ne, the nucleus ^{22}Ne is tightly bound with proton and neutron separation energies above 10 MeV and an α separation energy of 9667 keV. Accordingly, a behavior of the reduced cross section σ_{red} similar to other tightly bound projectiles can be expected.

Gross et al. [111] have measured an angular distribution of ^{208}Pb(^{22}Ne,^{22}Ne)^{208}Pb elastic scattering at 132 MeV, corresponding to E_{red} = 1.27 MeV. As no total cross section σ_{reac} is provided in [111], I have re-fitted the angular distribution. The resulting σ_{reac} = 1563 mb is about 13% higher than the result from the WS parameters in [111] which were determined in a coupled-channels approach. This leads to σ_{red} = 20.5 mb or a ratio $\sigma_{red}/\sigma_{red}(\alpha)$ = 1.23. Few further data points of an angular distribution heve been measured by Bottoni et al. [112] at 128 MeV as a part of their experiment for ^{24}Ne (see next Sect. 4.28). These few data points do not allow to derive σ_{reac} with high reliability. But a reasonable description of the few data points is achieved in [112] with standard OMP parameters, and so I use σ_{reac} = 1059 mb from that calculation, leading to σ_{red} = 13.9 mb at E_{red} = 1.23 MeV; this corresponds to a ratio $\sigma_{red}/\sigma_{red}(\alpha)$ = 0.90, i.e., slightly below unity. The two results for ^{22}Ne are shown in Figs. 8 and 9 with small light-brown full triangles; a more detailed view is provided in Figs. 22 and 23.

The data for ^{22}Ne do not reach low energies below E_{red} $\approx$ 1 MeV. Thus, a conclusion on the behavior of σ_{red} at sub-Coulomb energies is not possible for the tightly bound projectile ^{22}Ne, but the data show a weak trend towards low ratios ratio $\sigma_{red}/\sigma_{red}(\alpha)$ at low energies.

4.28 ^{208}Pb + ^{24}Ne

Only one angular distribution for ^{208}Pb(^{24}Ne,^{24}Ne)^{208}Pb at 182 MeV, corresponding to E_{red} = 1.75 MeV, is available in literature which is discussed in two papers by Benzoni et al. [113] and Bottoni et al. [112]. The resulting ratio $\sigma_{red}/\sigma_{red}(\alpha)$ = 1.07 is close to unity which is an expected result for a tightly bound projectile at energies significantly above the Coulomb barrier. Because the determination of σ_{reac} from few experimental data points is somewhat uncertain, I have re-fitted the angular distribution. My result for σ_{reac} is less than 5% higher than the original result, thus confirming the analysis in [112,113]. Note that despite the big ratio N/Z = 1.4 for ^{24}Ne, the neutron separation energy is still high with 8869 keV, and the proton and α separation energies are above 10 MeV. The result for ^{24}Ne is shown in Figs. 8 and 9 with a big open dusky pink triangle; a more detailed view is given in Figs. 22 and 23.

4.29 ^{208}Pb + ^{40}Ca

For comparison, I add some further examples of intermediate mass, tightly bound projectiles. Elastic ^{208}Pb(^{40}Ca,^{40}Ca)^{208}Pb scattering was investigated by Oganessian et al. [114] at 302 MeV, corresponding to E_{red} = 1.44 MeV. As σ_{reac} is not given in [114], I have re-fitted the data which are available at NRV from a re-digitization of Fig. 2 of [114]. The result for σ_{red} agrees with the reference calculation with a ratio of $\sigma_{red}/\sigma_{red}(\alpha)$ = 1.01 which is very close to unity.

The result for σ_{red} of ^{40}Ca is shown in Figs. 8 and 9 with a steel-blue full square. The relatively high energy of E_{red} = 1.44 MeV does not allow to draw conclusions on the low-energy behavior of σ_{red} for ^{40}Ca. Two further angular distributions for ^{40}Ca have been measured by Szilner et al. [115] at

the lower energies of 235 MeV and 249 MeV. Unfortunately, this experiment was not able to resolve inelastic contributions, and only quasi-elastic angular distributions are shown in Fig. 8 of [115]. As the data are available at EXFOR, I have re-fitted the angular distributions under the assumption that the inelastic contributions are small. This leads to ratios $\sigma_{red}/\sigma_{red}(\alpha) = 1.16$ and 1.26 at $E_{red} = 1.13$ MeV and 1.19 MeV. Inelastic contributions would reduce the elastic cross section and thus enhance the total reaction cross section σ_{reac}. Hence, although the determination of σ_{red} for the lower energies has major uncertainties from the unknown inelastic contributions, there is no evidence that the ratios $\sigma_{red}/\sigma_{red}(\alpha)$ for ^{40}Ca decrease towards low energies (as e.g. clearly observed for ^{12}C and ^{16}O). Because of the uncertain inelastic contributions, the σ_{red} from the Szilner et al. data are not included in Figs. 8 and 9.

4.30 ^{208}Pb + ^{48}Ca

Only one angular distribution of ^{208}Pb(^{48}Ca,^{48}Ca)^{208}Pb elastic scattering is available in literature at 252 MeV which was measured in the same experiment as ^{40}Ca in the previous Sect. 4.29 by Oganessian et al. [114]. The re-fit of the data leads to $\sigma_{red} = 11.9$ mb at $E_{red} = 1.19$ MeV, corresponding to a ratio $\sigma_{red}/\sigma_{red}(\alpha) = 0.86$ which is below the σ_{red} for ^{40}Ca. This result is shown with a big open orange circle in Figs. 8 and 9.

The relatively low σ_{red} of ^{48}Ca is somewhat unexpected because the significant neutron excess of ^{48}Ca with $N/Z = 1.4$ should lead to noticably enhanced neutron transfer cross sections. Thus, the low σ_{red} for ^{48}Ca at $E_{red} = 1.19$ MeV may be considered as a weak evidence for low ratios $\sigma_{red}/\sigma_{red}(\alpha)$ towards lower energies (as e.g. observed for ^{12}C and ^{16}O).

4.31 ^{208}Pb + ^{48}Ti

As final example I show the derived σ_{red} for ^{48}Ti which is another tightly bound nucleus. Here the experimental angular distribution of ^{208}Pb(^{48}Ti,^{48}Ti)^{208}Pb elastic scattering at 252 MeV by Oganessian et al. [114] covers a wide angular range which allows a reliable determination of the total reaction cross section. The energy of 252 MeV corresponds to a relatively low E_{red} of 1.08 MeV, and the obtained total reaction cross section from different fits of $\sigma_{reac} = 556 \pm 43$ mb corresponds to $\sigma_{red} = 6.1 \pm 0.5$ mb. The result is shown with a small red $\oplus$ symbol in Figs. 8 and 9.

The low ratio of $\sigma_{red}/\sigma_{red}(\alpha) = 0.67 \pm 0.05$ strengthens the evidence that the reduced cross sections σ_{red} for tightly bound projectiles are significantly lower than the reference calculation of the also tightly bound α particle. Note that the result for ^{48}Ti shows the lowest ratio $\sigma_{red}/\sigma_{red}(\alpha)$ at energies above $E_{red} = 1.0$ MeV for all reactions under study.

5 Discussion

It is widely accepted that the reduced cross sections σ_{red} for a variety of projectiles and targets are grouped into three categories, namely tightly bound projectiles, weakly bound projectiles, and projectiles with halo properties, see e.g. [1, 5–7]. It is obvious from the above Figs. 8 and 9 and the information in Sect. 4 that this simple classification does not fully reflect the more complex behavior of the σ_{red} vs. E_{red} data. This holds in particular for the energy dependence of σ_{red} which was previously not well visible because of the steep decrease of σ_{red} towards low energies. The present study improves the visualization by normalizing the σ_{red} data to a reference calculation for a tightly bound projectile. The α particle was chosen as a reference because (*i*) experimental data for σ_{red} are available down to energies of $E_{red} \approx 0.7$ MeV far below the Coulomb barrier, and (*ii*) a calculation is available which reproduces the σ_{red} data over the full energy range under study and can thus be used for interpolation between the experimental σ_{red} data and also for extrapolation towards lower energies.

It is found that at energies above the Coulomb barrier for $E_{red} > 1.5$ MeV all projectiles behave almost identical with ratios $\sigma_{red}/\sigma_{red}(\alpha)$ of the order of 1.0–1.5, with a slight trend of higher ratios for weakly bound projectiles, but overall almost independent of the properties of the projectile. Towards lower energies below $E_{red} \approx 1.3$ MeV, this ratio increases for weakly bound projectiles (like ^{6}Li, ^{7}Li, ^{7}Be, ^{9}Be), and this increase is more pronounced for projectiles with halo properties (like ^{6}He, ^{8}He, ^{8}Li, ^{9}Li, ^{11}Li, ^{8}B, ^{15}C). Surprisingly, also the tightly bound ^{19}F shows an increasing ratio towards lower E_{red}, very close to the results for ^{6}Li; but the latter result is not confirmed by later re-analyses of the scattering data (see Sect. 4.24).

The ratios for ^{7}Li show the unusual feature that the trend of increasing ratios towards lower energies changes around $E_{red} \approx 0.9$ MeV and leads to ratios $\sigma_{red}/\sigma_{red}(\alpha)$ between 1.5 and 2 which is much lower than for other weakly bound projectiles and halo projectiles where ratios above 10 and up to several thousand were found (the latter being outside of the scale of Fig. 9). The reason for this unusual finding for ^{7}Li remains unclear; for details, see Sect. 4.5.

Contrary to the weakly bound projectiles and halo projectiles, the ratios $\sigma_{red}/\sigma_{red}(\alpha)$ for tightly bound projectiles decrease with energy below $E_{red} \approx 1.0$ MeV. This holds for ^{12}C, ^{16}O, and ^{18}O, but it seems also to hold for the relatively weakly bound projectiles ^{17}O and ^{17}F. As a word of caution, it has to be mentioned that extremely low values of the ratio $\sigma_{red}/\sigma_{red}(\alpha)$ below $\approx 10^{-1}$ are only found for ^{12}C, ^{16}O, and one data point for ^{17}F. The data for ^{17}F may be underestimated because of inelastic scattering (see Sect. 3.6), and all data with $\sigma_{red}/\sigma_{red}(\alpha) < 10^{-1}$ for ^{12}C [83] and ^{16}O [32] were measured at the same lab (São Paulo Pelletron Accelerator,

Brazil). The discussion in Sect. 3.4 points to some inaccuracies in the energy of the data for ^{16}O at 78 MeV from different labs with a trend to lower values for the São Paulo data. However, such a minor inaccuracy of a few hundred keV cannot explain the found energy dependence of $\sigma_{red}/\sigma_{red}(\alpha)$. Nevertheless, although there is no reason to doubt in the São Paulo data, an independent verification of the low $\sigma_{red}/\sigma_{red}(\alpha)$ for ^{12}C and ^{16}O would be desirable.

The tightly bound projectile ^{10}Be shows relatively high ratios above $E_{red} \approx 0.95$ MeV, close to the data of ^{7}Li and ^{7}Be. But towards lower E_{red} the ratios drop steeply and come close to the results for tightly bound projectiles.

For several further projectiles only few angular distributions for elastic scattering from ^{208}Pb are available, and often the energies are located around or above $E_{red} \approx 1$ MeV. In these cases it is impossible to make a clear statement whether the σ_{red} for these projectiles behave regular. This holds e.g. for ^{11}B, ^{14}N, ^{17}Ne, ^{20}Ne, ^{22}Ne, ^{24}Ne and also for the intermediate mass projectiles ^{40}Ca, ^{48}Ca, and ^{48}Ti. However, the latter three intermediate mass projectiles show a slight trend to low ratios at low energies, i.e., similar to other tightly bound projectiles like ^{12}C and ^{16}O.

The above findings using the σ_{red} vs. E_{red} approach can be compared to the results from another approach which is based on the reduced critical interaction distance and reduced strong-absorption distance. Guimarães et al. [15] present data for elastic scattering of 14 light heavy ions between ^{6}He and ^{19}F on ^{208}Pb which in general nicely agree with the present results. In particular, small and almost identical reduced distances are found for ^{12}C, ^{16}O, and ^{17}F. Interestingly, the results for ^{19}F in [15] are also close to ^{12}C, ^{16}O, and ^{17}F. This finding is in agreement with the present re-analysis of the Lin et al. data [103] for ^{19}F; however, when the data from the original analysis in [103] are used, ^{19}F behaves different from ^{12}C, ^{16}O, and ^{17}F. Unfortunately, in the case of ^{7}Li, Guimarães et al. restrict themselves to the experimental data by Keeley et al. [51]. It would have been very interesting to see how the data by Martel et al. [53] would affect the analysis in [15] because the σ_{red} data by Martel et al. show a very unusual behavior in the present study.

All above data for σ_{red} are derived from experiments with ^{208}Pb. This allows a comparison of the different projectiles, because the same heavy target nucleus ^{208}Pb was used in all studies. For comparison with a light target, I finish the discussion by adding two plots for σ_{red} data with a ^{12}C target which have been reviewed recently by Zamora et al. [116] (see Figs. 24 and 25).

Similar to the data with the ^{208}Pb target, the σ_{red} data for the ^{12}C target are enhanced for weakly bound projectiles and halo projectiles like ^{6}He, ^{6}Li, ^{7}Li, ^{8}Li, ^{7}Be, ^{9}Be, and ^{8}B. Somewhat surprising, also the σ_{red} for ^{10}Be and ^{11}B are clearly enhanced, and the ratio $\sigma_{red}/\sigma_{red}(\alpha)$ is about 2 for energies above E_{red} = 1.5 MeV. (Note the larger scale of

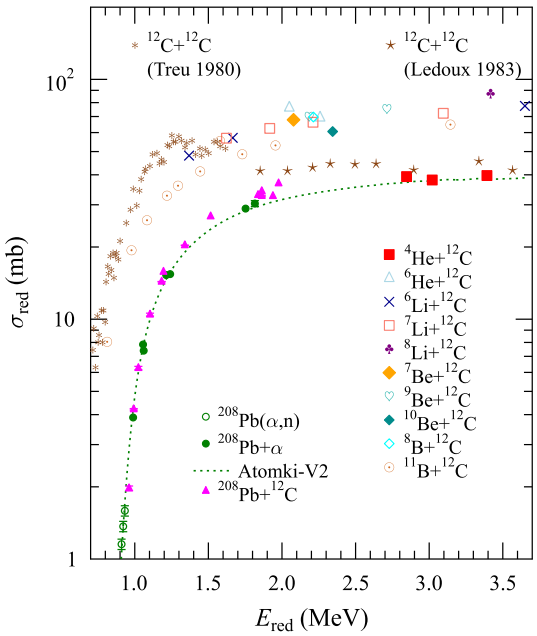

Fig. 24 Same as Fig. 8, but for ^{12}C as target (instead of ^{208}Pb). The σ_{red} data are taken from [116]. For comparison, the data for ^{12}C + ^{208}Pb from Fig. 8 are also shown. Further discussion see text

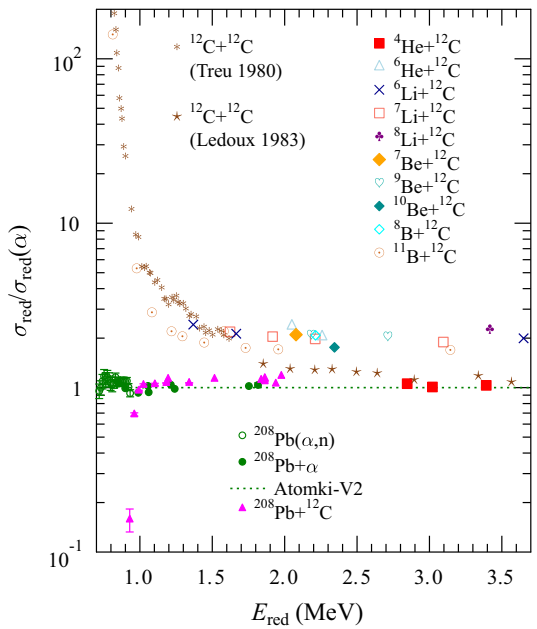

Fig. 25 Same as Fig. 9, but for ^{12}C as target (instead of ^{208}Pb). For comparison, the data for ^{12}C + ^{208}Pb from Fig. 9 are also shown. Further discussion see text

energies up to E_{red} = 3.7 MeV for the σ_{red} of the ^{12}C target in Figs. 24 and 25, compared to Figs. 8 and 9 for the ^{208}Pb target.)

Most of the data for the ^{12}C target in [116] do not reach the sub-Coulomb region where a very pronounced increase of the ratio $\sigma_{red}/\sigma_{red}(\alpha)$ was found for the ^{208}Pb target in com-

bination with weakly bound projectiles; most tightly bound projectiles showed the opposite trend of decreasing ratios towards low energies. Only the data for ^{11}B + ^{12}C scattering in [116] cover a wide range of E_{red}, and it can be seen that these data behave like weakly bound projectiles over the full range of E_{red}. A possible explanation for this exceptional behavior of the tightly bound ^{11}B and ^{12}C nuclei may be related to elastic proton exchange between the ^{11}B projectile and the ^{12}C target which leads to characteristic oscillation patterns in the backward range of the elastic scattering angular distributions even at low energies below the Coulomb barrier [117]. Such patterns are absent in all low-energy data under study with the ^{208}Pb target.

Also the σ_{red} data for ^{12}C + ^{12}C in [116] are found above the reference calculation with ratios $\sigma_{red}/\sigma_{red}(\alpha)$ between about 1.1 and 1.4 (with a small but clear trend towards increasing ratios with decreasing energy). Contrary, the data for ^{12}C + ^{208}Pb show ratios closer to unity at higher reduced energies E_{red} and the opposite energy dependence. The energy range of the ^{12}C + ^{12}C data in [116] is restricted to $E_{c.m.}$ between 14.6 MeV and 30.9 MeV because the data are taken from Ledoux et al. [118] only. Because of the high relevance of the ^{12}C + ^{12}C fusion cross section at low energies (mainly motivated for the determination of astrophysical reaction rates, see e.g. [119–121]), I add also the data by Treu et al. [122] at lower energies down to $E_{c.m.} = 5.5$ MeV, thus covering E_{red} from 0.71 MeV to 3.9 MeV. Unfortunately, the data by Treu et al. and by Ledoux et al. do not overlap. But from a reasonable extrapolation of the energy dependence, one can estimate that the absolute normalization of the data by Treu et al. is about a factor of 1.5 higher than the data by Ledoux et al. (as can be nicely seen in Fig. 25). Subsequent theoretical analyses [123,124] of these two data sets and a comparison to the experimental reaction yields in [125] clearly favor the lower absolute normalization of the Ledoux et al. data. But independent of the somewhat uncertain absolute normalization, the σ_{red} data of Treu et al. nicely show that the ratio $\sigma_{red}/\sigma_{red}(\alpha)$ increases strongly towards low energies for ^{12}C + ^{12}C whereas the completely opposite behavior was found for the ^{12}C + ^{208}Pb data in Sect. 4.16. For completeness it has to be noted that the number of data points for the total reaction cross sections in the original papers [118], Fig. 4, and [122], Fig. 2, is much larger than the shown data points in Figs. 24 and 25 because it is practically impossible to re-digitize those data points from the tiny original Figures; but the shown data in Figs. 24 and 25 reflect the general trend of the original data.

Summarizing the above discussion, the comparison of reduced cross sections σ_{red} for different projectile-target combinations at energies around the Coulomb barrier shows that there is no simple classification scheme into tightly bound nuclei, weakly bound nuclei, and halo nuclei. The energy dependence of σ_{red}, best visualized by a plot of the ratio to a reference calculation $\sigma_{red}/\sigma_{red}(\alpha)$, shows strong trends to low ratios for tightly bound projectiles and strongly increasing ratios for weakly bound and halo projectiles towards low energies. But also exceptional behaviors are found e.g. for ^{7}Li with its unusual energy dependence of σ_{red} or for ^{17}F with its behavior like a tightly bound projectile despite its small proton separation energy of less than 1 MeV. Furthermore, for ^{12}C it is found that the σ_{red} behave as expected like a tightly bound projectile for the ^{208}Pb target, but like a weakly bound projectile for a ^{12}C target. The behavior of σ_{red} for ^{12}C-induced elastic scattering from various targets and the transition from low ratios $\sigma_{red}/\sigma_{red}(\alpha)$ for heavy targets (^{208}Pb) to high ratios for light targets (^{12}C) should be the scope of future investigations. A recent study by Xu et al. [126] has already investigated various elastic scattering angular distributions of ^{12}C-induced reacions, and a global ^{12}C-nucleus OMP is provided. However, this global potential cannot reach the required accuracy to extract total reaction cross sections σ_{reac} at low energies. In several cases this global ^{12}C-nucleus OMP underestimates the elastic scattering cross sections at low energies in the backward angular range, thus leading to an overestimation of the total reaction cross section σ_{reac} in these cases.

6 Summary and conclusions

Total reaction cross sections σ_{reac} were derived from angular distributions of elastic scattering for various projectiles and the target nucleus ^{208}Pb. Overall, about 200 σ_{reac} are derived at energies around the Coulomb barrier. Depending on the available data in the original papers and in the EXFOR and NRV databases, the σ_{reac} were taken either (i) from the original paper (if available) or (ii) re-calculated from the optical model parameters in the original paper (if available) or (iii) determined by re-fitting the angular distributions from EXFOR or NRV. These data for σ_{reac} allow to characterize the properties of the projectile nuclei because the same target nucleus ^{208}Pb is used in all cases under study.

For comparison of the results for different projectiles at different energies, the simple reduction scheme of reduced cross sections σ_{red} vs. reduced energies E_{red} (as proposed by Gomes et al. [1]) was applied. Because of the steep energy dependence of σ_{red} towards low energies below the Coulomb barrier, the data are presented as ratio $\sigma_{red}/\sigma_{red}(\alpha)$ where $\sigma_{red}(\alpha)$ is a reference which is calculated for α-induced reactions using the Atomki-V2 α-nucleus optical model potential. This presentation illustrates differences in the energy dependence of the σ_{red} for the different projectiles which might go missing in the logarithmic scale of the standard σ_{red} vs. E_{red} presentation.

It is generally accepted that the σ_{red} are grouped into three categories, namely tightly bound nuclei with low σ_{red}, weakly

bound nuclei with slightly enhanced σ_{red}, and exotic halo nuclei with strongly enhanced σ_{red}. The present work shows that the σ_{red} at higher energies above $E_{red} \approx 1.5$ MeV are close to each other, with only small enhancements for weakly bound and for exotic halo nuclei. But there are dramatic differences between the σ_{red} towards lower energies, in particular below $E_{red} \approx 1.0$ MeV, with extremely high ratios $\sigma_{red}/\sigma_{red}(\alpha)$ up to several orders of magnitude for exotic halo nuclei, but also with low ratios far below unity for tightly bound nuclei like ^{12}C and ^{16}O. The latter result is somewhat unexpected as the chosen reference, the α-particle, is also tightly bound.

Furthermore, besides these general findings, there are some special cases with unusual or unexpected behavior. For ^{7}Li the energy dependence of $\sigma_{red}/\sigma_{red}(\alpha)$ deviates towards low energies from the otherwise found increasing ratio for weakly bound nuclei. The relatively weakly bound nuclei ^{17}O and ^{17}F behave like or at least close to the tightly bound doubly-magic ^{16}O. Contrary, there is some evidence that the moderately bound ^{13}C shows much larger σ_{red} than the tightly bound ^{12}C. The results for ^{19}F in the original paper [103] differ from several later analyses of the same data, including the present re-analysis, and thus no clear statement on the energy dependence of σ_{red} for ^{19}F can be made.

Finally, a comparison of σ_{red} for the target nucleus ^{208}Pb (from this work) and for the target ^{12}C (from [116]) shows that in some cases the ratios $\sigma_{red}/\sigma_{red}(\alpha)$ behave completely different. This is most pronounced for ^{12}C + ^{208}Pb with low and decreasing ratios $\sigma_{red}/\sigma_{red}(\alpha)$ towards low energies, but high and increasing ratios towards low energies for ^{12}C + ^{12}C.

Further experimental angular distributions over a wide angular range with small uncertainties are required to provide deeper insight into the behavior of the reduced cross sections σ_{red} as a function of reduced energy E_{red}. A careful analysis of these angular distributions is mandatory to determine σ_{reac} and σ_{red} from the experimental data, with a focus on the uncertainty of σ_{reac}. Such additional data are essential to strengthen and verify the above conclusions, in particular on the found ratios $\sigma_{red}/\sigma_{red}(\alpha)$ towards low energies with their huge variations between about 10^{-2} and 10^{+4} below $E_{red} < 1$ MeV.

Note added in Proof

The final analysis of the data for ^{15}C (see Sect. 4.18) became available after submission of the present work [Távora *et el.*, Phys. Lett. B **855**, 138770 (2024)]. The total reaction cross section σ_{reac} is now given as 1695 mb which is a factor of 1.79 lower than the preliminary analysis in Ovejas et al. [89] where $\sigma_{reac} = 3035$ mb was derived. This brings the reduced cross section σ_{red} for ^{15}C closer to the results of other weakly bound projectiles like ^{6}He, but is still significantly above the results for tightly bound projectiles.

Acknowledgements I thank many colleagues and friends from Atomki for 30 years of longstanding collaboration with many encouraging discussions. In particular, the common work with Zs. Fülöp, Gy. Gyürky, G. G. Kiss, T. Szücs, and E. Somorjai is acknowledged. This work was supported by NKFIH (K134197).

Funding Open access funding provided by HUN-REN Institute for Nuclear Research.

Data Availability Statement Data will be made available on reasonable request. [Author's comment: Data is available upon request from the Authors.]

Code Availability Statement Code/software will be made available on reasonable request. [Author's comment: Code is available upon request from the Authors.]

Appendix A Reference cross section for ^{208}Pb + ^{4}He

The results for the reference calculation for the system ^{208}Pb + ^{4}He are listed in Table 2. The calculation has been discussed in Sect. 4.1. Table 2 includes the reduced energy E_{red}, the reduced cross section σ_{red}, the underlying energy $E_{c.m.}$ in the center-of-mass system and the total reaction cross section σ_{reac}. In addition, the astrophysical S-factor $S(E)$ is given. Interpolations for σ_{red} between the given E_{red} should be done using the S-factor instead of the very steep σ_{red} towards the lowest E_{red}.

Table 2 Results of the reference calculation for the ^{208}Pb + ^{4}He system for E_{red} = 0.5 to 2.5 MeV. In addition to the cross sections, also the astrophysical S-factor is listed

E_{red} (MeV)	$\sigma_{red}(\alpha)$ (mb)	$E_{c.m.}$ (MeV)	σ_{reac} (mb)	$S(E)$ (keV b)	E_{red} (MeV)	$\sigma_{red}(\alpha)$ (mb)	$E_{c.m.}$ (MeV)	σ_{reac} (mb)	$S(E)$ (keV b)
0.500	1.685e–09	10.915	9.508e–08	1.945e+36	1.500	2.336e+01	32.746	1.318e+03	1.100e+29
0.525	1.341e–08	11.461	7.571e–07	1.558e+36	1.525	2.394e+01	33.292	1.351e+03	7.218e+28
0.550	9.050e–08	12.007	5.107e–06	1.239e+36	1.550	2.450e+01	33.837	1.383e+03	4.781e+28
0.575	5.264e–07	12.553	2.971e–05	9.800e+35	1.575	2.504e+01	34.383	1.413e+03	3.196e+28
0.600	2.680e–06	13.098	1.513e–04	7.702e+35	1.600	2.555e+01	34.929	1.442e+03	2.155e+28
0.625	1.210e–05	13.644	6.830e–04	6.017e+35	1.625	2.605e+01	35.475	1.470e+03	1.466e+28
0.650	4.904e–05	14.190	2.768e–03	4.676e+35	1.650	2.652e+01	36.020	1.497e+03	1.005e+28
0.675	1.801e–04	14.736	1.017e–02	3.616e+35	1.675	2.698e+01	36.566	1.523e+03	6.948e+27
0.700	6.053e–04	15.281	3.416e–02	2.785e+35	1.700	2.742e+01	37.112	1.548e+03	4.840e+27
0.725	1.876e–03	15.827	1.059e–01	2.138e+35	1.725	2.784e+01	37.658	1.571e+03	3.397e+27
0.750	5.405e–03	16.373	3.050e–01	1.637e+35	1.750	2.825e+01	38.204	1.594e+03	2.401e+27
0.775	1.456e–02	16.919	8.219e–01	1.252e+35	1.775	2.864e+01	38.749	1.616e+03	1.710e+27
0.800	3.689e–02	17.464	2.082e+00	9.555e+34	1.800	2.902e+01	39.295	1.638e+03	1.225e+27
0.825	8.811e–02	18.010	4.973e+00	7.269e+34	1.825	2.937e+01	39.841	1.658e+03	8.840e+26
0.850	1.985e–01	18.556	1.120e+01	5.489e+34	1.850	2.971e+01	40.387	1.677e+03	6.417e+26
0.875	4.192e–01	19.102	2.366e+01	4.077e+34	1.875	3.005e+01	40.932	1.696e+03	4.689e+26
0.900	8.210e–01	19.648	4.633e+01	2.934e+34	1.900	3.037e+01	41.478	1.714e+03	3.446e+26
0.925	1.470e+00	20.193	8.294e+01	2.012e+34	1.925	3.068e+01	42.024	1.731e+03	2.547e+26
0.950	2.382e+00	20.739	1.344e+02	1.298e+34	1.950	3.097e+01	42.570	1.748e+03	1.893e+26
0.975	3.507e+00	21.285	1.979e+02	7.885e+33	1.975	3.125e+01	43.115	1.764e+03	1.415e+26
1.000	4.758e+00	21.831	2.685e+02	4.565e+33	2.000	3.152e+01	43.661	1.779e+03	1.063e+26
1.025	6.055e+00	22.376	3.417e+02	2.559e+33	2.025	3.179e+01	44.207	1.794e+03	8.034e+25
1.050	7.346e+00	22.922	4.146e+02	1.409e+33	2.050	3.204e+01	44.753	1.808e+03	6.098e+25
1.075	8.604e+00	23.468	4.856e+02	7.702e+32	2.075	3.229e+01	45.298	1.822e+03	4.651e+25
1.100	9.814e+00	24.014	5.539e+02	4.210e+32	2.100	3.252e+01	45.844	1.835e+03	3.565e+25
1.125	1.097e+01	24.559	6.193e+02	2.312e+32	2.125	3.275e+01	46.390	1.848e+03	2.745e+25
1.150	1.208e+01	25.105	6.817e+02	1.280e+32	2.150	3.297e+01	46.936	1.861e+03	2.123e+25
1.175	1.314e+01	25.651	7.413e+02	7.160e+31	2.175	3.319e+01	47.482	1.873e+03	1.650e+25
1.200	1.414e+01	26.197	7.982e+02	4.049e+31	2.200	3.339e+01	48.027	1.885e+03	1.287e+25
1.225	1.511e+01	26.742	8.526e+02	2.318e+31	2.225	3.359e+01	48.573	1.896e+03	1.008e+25
1.250	1.603e+01	27.288	9.045e+02	1.343e+31	2.250	3.379e+01	49.119	1.907e+03	7.929e+24
1.275	1.691e+01	27.834	9.542e+02	7.879e+30	2.275	3.398e+01	49.665	1.918e+03	6.261e+24
1.300	1.775e+01	28.380	1.002e+03	4.680e+30	2.300	3.417e+01	50.210	1.928e+03	4.964e+24
1.325	1.856e+01	28.926	1.047e+03	2.814e+30	2.325	3.435e+01	50.756	1.939e+03	3.949e+24
1.350	1.933e+01	29.471	1.091e+03	1.712e+30	2.350	3.452e+01	51.302	1.948e+03	3.154e+24
1.375	2.007e+01	30.017	1.133e+03	1.054e+30	2.375	3.469e+01	51.848	1.958e+03	2.527e+24
1.400	2.078e+01	30.563	1.173e+03	6.567e+29	2.400	3.485e+01	52.393	1.967e+03	2.032e+24
1.425	2.147e+01	31.109	1.212e+03	4.135e+29	2.425	3.502e+01	52.939	1.976e+03	1.640e+24
1.450	2.212e+01	31.654	1.249e+03	2.632e+29	2.450	3.518e+01	53.485	1.985e+03	1.327e+24
1.475	2.275e+01	32.200	1.284e+03	1.693e+29	2.475	3.534e+01	54.031	1.995e+03	1.078e+24

References

1. P.R.S. Gomes, J. Lubian, I. Padron, R.M. Anjos, Uncertainties in the comparison of fusion and reaction cross sections of different systems involving weakly bound nuclei. Phys. Rev. C **71**, 017601 (2005). https://doi.org/10.1103/PhysRevC.71.017601
2. A. Ingemarsson, J. Nyberg, P.U. Renberg, O. Sundberg, R.F. Carlson, A.J. Cox, A. Auce, R. Johansson, G. Tibell, D.T. Khoa, R.E. Warner, New results for reaction cross sections of intermediate energy α-particles on targets from 9Be to 208Pb. Nucl. Phys. A **676**(1), 3–31 (2000). https://doi.org/10.1016/S0375-9474(00)00200-1
3. G. Gyürky, P. Mohr, Z. Fülöp, Z. Halász, G.G. Kiss, T. Szücs, E. Somorjai, Relation between total cross sections from elastic scattering and α-induced reactions: The example of ^{64}zn. Phys. Rev. C **86**, 041601 (2012). https://doi.org/10.1103/PhysRevC.86.041601
4. A. Ornelas, P. Mohr, G. Gyürky, Z. Elekes, Z. Fülöp, Z. Halász, G.G. Kiss, E. Somorjai, T. Szücs, M.P. Takács, D. Galaviz, R.T. Güray, Z. Korkulu, N. Özkan, C. Yalçin, α scattering and α-induced reaction cross sections of ^{64}Zn at low energies. Phys. Rev. C **94**, 055807 (2016). https://doi.org/10.1103/PhysRevC.94.055807
5. C. Signorini, M. Mazzocco, D. Pierroutsakou, In: Tanihata, I., Toki, H., Kajino, T. (eds.) Low-Energy Reactions with Halo Nuclei, pp. 1125–1204. Springer, Singapore (2023). https://doi.org/10.1007/978-981-19-6345-2_67
6. J.J. Kolata, V. Guimarães, E.F. Aguilera, Elastic scattering, fusion, and breakup of light exotic nuclei. The European Physical Journal A **52**, 123 (2016). https://doi.org/10.1140/epja/i2016-16123-1
7. E.F. Aguilera, E. Martinez-Quiroz, D. Lizcano, A. Gómez-Camacho, J.J. Kolata, L.O. Lamm, V. Guimarães, R. Lichtenthäler, O. Camargo, F.D. Becchetti, H. Jiang, P.A. DeYoung, P.J. Mears, T.L. Belyaeva, Reaction cross sections for ^{8}B, ^{7}Be, and ^{6}Li +^{58} Ni near the coulomb barrier: Proton-halo effects. Phys. Rev. C **79**, 021601 (2009). https://doi.org/10.1103/PhysRevC.79.021601
8. Faria, P.N., Lichtenthäler, R., Pires, K.C.C., Moro, A.M., Lépine-Szily, A., Guimarães, V., Mendes, D.R., Arazi, A., Rodríguez-Gallardo, M., Barioni, A., Morcelle, V., Morais, M.C., Camargo, O., Alcantara Nuñez, J., Assunção, M.: Elastic scattering and total reaction cross section of ^{6}He +^{120} Sn. Phys. Rev. C **81**, 044605 (2010) https://doi.org/10.1103/PhysRevC.81.044605
9. A. Lépine-Szily, L. R., V. Guimarães, The Radioactive Ion Beams in Brazil (RIBRAS) facility. The European Physical Journal A **50**, 128 (2014) https://doi.org/10.1140/epja/i2014-14128-4
10. P. Mohr, G.G. Kiss, Z. Fülöp, D. Galaviz, G. Gyürky, E. Somorjai, Elastic alpha scattering experiments and the alpha-nucleus optical potential at low energies. At. Data Nucl. Data Tables **99**(6), 651–679 (2013). https://doi.org/10.1016/j.adt.2012.10.003
11. P. Mohr, Cross sections of α-induced reactions for targets with masses $A \approx 20 - 50$ at low energies. The European Physical Journal A **51**(5), 56 (2015). https://doi.org/10.1140/epja/i2015-15056-5
12. I. Tanihata, H. Savajols, R. Kanungo, Recent experimental progress in nuclear halo structure studies. Prog. Part. Nucl. Phys. **68**, 215–313 (2013). https://doi.org/10.1016/j.ppnp.2012.07.001
13. A.D. Pietro, P. Figuera, M. Fisichella, M. Lattuada, M. Zadro, Elastic scattering induced by halo nuclei. J. Phys: Conf. Ser. **492**(1), 012001 (2014). https://doi.org/10.1088/1742-6596/492/1/012001
14. P.R. Christensen, V.I. Manko, F.D. Becchetti, R.J. Nickles, A study of 16,18o and 12c induced reactions on a = 40–96 nuclei. Nucl. Phys. A **207**(1), 33–77 (1973). https://doi.org/10.1016/0375-9474(73)90023-7
15. V. Guimarães, J. Lubian, J.J. Kolata, E.F. Aguilera, M. Assunção, V. Morcelle, Phenomenological critical interaction distance from elastic scattering measurements on a ^{208}Pb target. The European Physical Journal A **54**, 223 (2018). https://doi.org/10.1140/epja/i2018-12662-7
16. A. Pakou, K. Rusek, Interaction distances for weakly bound nuclei at near barrier energies. Phys. Rev. C **69**, 057602 (2004). https://doi.org/10.1103/PhysRevC.69.057602
17. C.Y. Wong, Interaction barrier in charged-particle nuclear reactions. Phys. Rev. Lett. **31**, 766–769 (1973). https://doi.org/10.1103/PhysRevLett.31.766
18. L.F. Canto, P.R.S. Gomes, J. Lubian, L.C. Chamon, E. Crema, Dynamic effects of breakup on fusion reactions of weakly bound nuclei. Nucl. Phys. A **821**(1), 51–71 (2009). https://doi.org/10.1016/j.nuclphysa.2009.02.001
19. L.F. Canto, P.R.S. Gomes, J. Lubian, L.C. Chamon, E. Crema, Disentangling static and dynamic effects of low breakup threshold in fusion reactions. J. Phys. G: Nucl. Part. Phys. **36**(1), 015109 (2008). https://doi.org/10.1088/0954-3899/36/1/015109
20. N. Otuka, E. Dupont, V. Semkova, B. Pritychenko, A.I. Blokhin, M. Aikawa, S. Babykina, M. Bossant, G. Chen, S. Dunaeva, R.A. Forrest, T. Fukahori, N. Furutachi, S. Ganesan, Z. Ge, O.O. Gritzay, M. Herman, S. Hlavač, K. Katō, B. Lalremruata, Y.O. Lee, A. Makinaga, K. Matsumoto, M. Mikhaylyukova, G. Pikulina, V.G. Pronyaev, A. Saxena, O. Schwerer, S.P. Simakov, N. Soppera, R. Suzuki, S. Takács, X. Tao, S. Taova, F. Tárkányi, V.V. Varlamov, J. Wang, S.C. Yang, V. Zerkin, Y. Zhuang, Towards a More Complete and Accurate Experimental Nuclear Reaction Data Library (EXFOR): International Collaboration Between Nuclear Reaction Data Centres (NRDC). Nucl. Data Sheets **120**, 272–276 (2014). https://doi.org/10.1016/j.nds.2014.07.065
21. N. Otuka, Data base EXFOR. https://www-nds.iaea.org/exfor/
22. A.S. Denikin, A.P. Alekseev, A.V. Karpov, V.V. Samarin, M.A. Naumenko, A.Y. Kozhin, V.A. Rachkov, V.V. Saiko, Data base NRV. http://nrv.jinr.ru/nrv/
23. E. Friedman, C.J. Batty, Method for optical model analysis of alpha-nucleus elastic scattering. Phys. Rev. C **17**, 34–42 (1978). https://doi.org/10.1103/PhysRevC.17.34
24. G. Bartnitzky, A. Blazevic, H.G. Bohlen, J.M. Casandjian, M. Chartier, H. Clement, B. Gebauer, A. Gillibert, T. Kirchner, D.T. Khoa, A. Lepine-Szily, W. Mittig, W. von Oertzen, A.N. Ostrowski, P. Roussel-Chomaz, J. Siegler, M. Wilpert, T. Wilpert, Model-unrestricted nucleus-nucleus scattering potentials from measurement and analysis of 16o + 16o scattering. Phys. Lett. B **365**(1), 23–28 (1996). https://doi.org/10.1016/0370-2693(95)01292-3
25. U. Atzrott, P. Mohr, H. Abele, C. Hillenmayer, G. Staudt, Uniform α-nucleus potential in a wide range of masses and energies. Phys. Rev. C **53**, 1336–1347 (1996). https://doi.org/10.1103/PhysRevC.53.1336
26. V. Chisté, R. Lichtenthäler, A.C.C. Villari, L.C. Gomes, S-matrix analysis of heavy-ion elastic scattering. Phys. Rev. C **54**, 784–790 (1996). https://doi.org/10.1103/PhysRevC.54.784
27. W. Karcz, I. Kluska, Z. Sanok, J. Szmider, J. Szymankowski, S. Wiktor, R. Wolski, Measurements of the elastic scattering cross-section of alpha particles on the heavy and medium weight nuclei in the vicinity of the Coulomb barrier in a wide angular range. Acta Physica Polonica **3**, 525–530 (1972)
28. J.J. Kolata, E.F. Aguilera, F.D. Becchetti, Y. Chen, P.A. DeYoung, H. García-Martínez, J.D. Hinnefeld, J.H. Lupton, E. Martinez-Quiroz, G. Peaslee, Elastic scattering of ^{10}Be on ^{208}Pb near the coulomb barrier. Phys. Rev. C **69**, 047601 (2004). https://doi.org/10.1103/PhysRevC.69.047601
29. J.S. Lilley, M.A. Nagarajan, D.W. Banes, B.R. Fulton, I.J. Thompson, Multistep effects in reactions of 17O with 208Pb near the

coulomb barrier. Nucl. Phys. A **463**(3), 710–730 (1987). https://doi.org/10.1016/0375-9474(87)90639-7
30. E. Vulgaris, L. Grodzins, S.G. Steadman, R. Ledoux, Fusion, transfer, and elastic scattering at sub-barrier energies for ^{16},18o ions on ^{208}Pb and ^{15}N and ^{16}O ions on ^{209}Bi. Phys. Rev. C **33**, 2017–2027 (1986). https://doi.org/10.1103/PhysRevC.33.2017
31. E. Vulgaris, L. Grodzins, S.G. Steadman, R. Ledoux, Erratum: Fusion, transfer, and elastic scattering at sub-barrier energies for ^{16},18O ions on ^{208}Pb and ^{15}N and ^{16}O ions on ^{209}Bi. Phys. Rev. C **34**, 1495–1495 (1986). https://doi.org/10.1103/PhysRevC.34.1495
32. C.P. Silva, M.A.G. Alvarez, L.C. Chamon, D. Pereira, M.N. Rao, E.S. Rossi Jr., L.R. Gasques, M.A.E. Santo, R.M. Anjos, J. Lubian, P.R.S. Gomes, C. Muri, B.V. Carlson, S. Kailas, A. Chatterjee, P. Singh, A. Shrivastava, K. Mahata, S. Santra, The heavy-ion nuclear potential: determination of a systematic behavior at the region of surface interaction distances. Nucl. Phys. A **679**(3), 287–303 (2001). https://doi.org/10.1016/S0375-9474(00)00347-X
33. J. Grineviciute, P. Descouvemont, Elastic scattering of ^{17}F,^{17}O, and ^{19}F on a heavy target in a microscopic continuum discretized coupled-channels method. Phys. Rev. C **90**, 034616 (2014). https://doi.org/10.1103/PhysRevC.90.034616
34. A.R. Barnett, J.S. Lilley, Interaction of alpha particles in the lead region near the coulomb barrier. Phys. Rev. C **9**, 2010–2027 (1974). https://doi.org/10.1103/PhysRevC.9.2010
35. J.S. Lilley, M.A. Franey, F. Da Hsuan, Alpha inelastic scattering by 208pb near the coulomb barrier. Nucl. Phys. A **342**(1), 165–184 (1980). https://doi.org/10.1016/0375-9474(80)90512-6
36. A.M. Baxter, S. Hinds, R.H. Spear, T.H. Zabel, R. Smith, Octupole vibrations in the even mercury and lead isotopes. Nucl. Phys. A **369**(1), 25–37 (1981). https://doi.org/10.1016/0375-9474(81)90004-X
37. V.Y. Gonchar, K.S. Zheltonog, G.N. Ivanov, V.I. Kanashevich, S.V. Laptev, A.V. Yushkov, Small-Angle Elastic Scattering of Alpha Particles on Nickel and Lead. Sov. J. Nucl. Phys. **9**, 843 (1969)
38. G.M. Hudson, R.H. Davis, ^{208}Pb$(\alpha,\alpha)^{208}$Pb scattering near the coulomb barrier. Phys. Rev. C **9**, 1521–1524 (1974). https://doi.org/10.1103/PhysRevC.9.1521
39. G. Gyürky, P. Mohr, A. Angyal, Z. Halász, G.G. Kiss, Z. Mátyus, T.N. Szegedi, T. Szücs, Z. Fülöp, Cross section measurement of the ^{144}Sm$(\alpha,n)^{147}$Gd reaction for studying the α-nucleus optical potential at astrophysical energies. Phys. Rev. C **107**, 025803 (2023). https://doi.org/10.1103/PhysRevC.107.025803
40. P. Mohr, Z. Fülöp, G. Gyürky, G.G. Kiss, T. Szücs, Successful prediction of total α-induced reaction cross sections at astrophysically relevant sub-coulomb energies using a novel approach. Phys. Rev. Lett. **124**, 252701 (2020). https://doi.org/10.1103/PhysRevLett.124.252701
41. P. Mohr, Z. Fülöp, G. Gyürky, G.G. Kiss, T. Szücs, A. Arcones, M. Jacobi, A. Psaltis, Astrophysical reaction rates of α-induced reactions for nuclei with $26 \leq z \leq 83$ from the new atomki-v2 α-nucleus potential. At. Data Nucl. Data Tables **142**, 101453 (2021). https://doi.org/10.1016/j.adt.2021.101453
42. A.M. Sánchez-Benítez, D. Escrig, M.A.G. Álvarez, M.V. Andrés, C. Angulo, M.J.G. Borge, J. Cabrera, S. Cherubini, P. Demaret, J.M. Espino, P. Figuera, M. Freer, J.E. García-Ramos, J. Gómez-Camacho, M. Gulino, O.R. Kakuee, I. Martel, C. Metelko, A.M. Moro, F. Pérez-Bernal, J. Rahighi, K. Rusek, D. Smirnov, O. Tengblad, P. Van Duppen, V. Ziman, Study of the elastic scattering of 6he on 208pb at energies around the coulomb barrier. Nucl. Phys. A **803**(1), 30–45 (2008). https://doi.org/10.1016/j.nuclphysa.2008.01.030
43. L. Acosta, A.M. Sánchez-Benítez, M.E. Gómez, I. Martel, F. Pérez-Bernal, F. Pizarro, J. Rodríguez-Quintero, K. Rusek, M.A.G. Alvarez, M.V. Andrés, J.M. Espino, J.P. Fernández-García, J. Gómez-Camacho, A.M. Moro, C. Angulo, J. Cabrera, E. Casarejos, P. Demaret, M.J.G. Borge, D. Escrig, O. Tengblad, S. Cherubini, P. Figuera, M. Gulino, M. Freer, C. Metelko, V. Ziman, R. Raabe, I. Mukha, D. Smirnov, O.R. Kakuee, J. Rahighi, Elastic scattering and α-particle production in ^{6}he + ^{208}pb collisions at 22 mev. Phys. Rev. C **84**, 044604 (2011). https://doi.org/10.1103/PhysRevC.84.044604
44. G. Marquínez-Durán, I. Martel, A.M. Sánchez-Benítez, L. Acosta, R. Berjillos, J. Dueñas, K. Rusek, N. Keeley, M.A.G. Álvarez, M.J.G. Borge, A. Chbihi, C. Cruz, M. Cubero, J.P. Fernández-García, B. Fernández-Martínez, J.L. Flores, J. Gómez-Camacho, K.W. Kemper, J.A. Labrador, M. Marqués, A.M. Moro, M. Mazzocco, A. Pakou, V.V. Parkar, N. Patronis, V. Pesudo, D. Pierroutsakou, R. Raabe, R. Silvestri, N. Soic, L. Standyło, I. Strojek, O. Tengblad, R. Wolski, Z. Abou-Haidar, Precise measurement of near-barrier ^{8}He +^{208} Pb elastic scattering: Comparison with ^{6}He. Phys. Rev. C **94**, 064618 (2016). https://doi.org/10.1103/PhysRevC.94.064618
45. O.R. Kakuee, J. Rahighi, A.M. Sánchez-Benıítez, M.V. Andrés, S. Cherubini, T. Davinson, W. Galster, J. Gómez-Camacho, A.M. Laird, M. Lamehi-Rachti, I. Martel, A.C. Shotter, W.B. Smith, J. Vervier, P.J. Woods, Elastic scattering of the halo nucleus 6he from 208pb above the coulomb barrier. Nucl. Phys. A **728**(3), 339–349 (2003). https://doi.org/10.1016/j.nuclphysa.2003.08.030
46. O.R. Kakuee, M.A.G. Alvarez, M.V. Andrés, S. Cherubini, T. Davinson, A. Di Pietro, W. Galster, J. Gómez-Camacho, A.M. Laird, M. Lamehi-Rachti, I. Martel, A.M. Moro, J. Rahighi, A.M. Sánchez-Benitez, A.C. Shotter, W.B. Smith, J. Vervier, P.J. Woods, Long range absorption in the scattering of 6he on 208pb and 197au at 27 mev. Nucl. Phys. A **765**(3), 294–306 (2006). https://doi.org/10.1016/j.nuclphysa.2005.11.012
47. P. Mohr, Folding potential for the system ^{209}Bi−^{6}He. Phys. Rev. C **62**, 061601 (2000). https://doi.org/10.1103/PhysRevC.62.061601
48. P. Mohr, P.N. Faria, R. Lichtenthäler, K.C.C. Pires, V. Guimarães, A. Lépine-Szily, D.R. Mendes, A. Arazi, A. Barioni, V. Morcelle, M.C. Morais, Comparison of ^{120}Sn(^{6}He,^{6}He)^{120}Sn and ^{120}Sn$(\alpha,\alpha)^{120}$Sn elastic scattering and signatures of the ^{6}He neutron halo in the optical potential. Phys. Rev. C **82**, 044606 (2010). https://doi.org/10.1103/PhysRevC.82.044606
49. G. Marquínez-Durán, I. Martel, A.M. Sánchez-Benítez, L. Acosta, J.L. Aguado, R. Berjillos, A.R. Pinto, T. García, J.A. Dueñas, K. Rusek, N. Keeley, K.W. Kemper, M.A.G. Álvarez, M.J.G. Borge, A. Chbihi, C. Cruz, M. Cubero, J.P. Fernández-García, B. Fernández-Martínez, J.L. Flores, J. Gómez-Camacho, J.A. Labrador, F.M. Marqués, A.M. Moro, M. Mazzocco, A. Pakou, V.V. Parkar, N. Patronis, V. Pesudo, D. Pierroutsakou, R. Raabe, R. Silvestri, N. Soić, L. Standyło, I. Strojek, O. Tengblad, R. Wolski, Z. Abou-Haidar, Interaction of ^{8}He with ^{208}Pb at near-barrier energies: ^{4}He and ^{6}He production. Phys. Rev. C **98**, 034615 (2018). https://doi.org/10.1103/PhysRevC.98.034615
50. H. Gemmeke, B. Deluigi, L. Lassen, D. Scholz, Coulomb and Nuclear Excitation in the Sequential Break-up of ^{6}Li. Z. Phys. A. **286**, 73–75 (1978). https://doi.org/10.1007/BF01434615
51. N. Keeley, S.J. Bennett, N.M. Clarke, B.R. Fulton, G. Tungate, P.V. Drumm, M.A. Nagarajan, J.S. Lilley, Optical model analyses of 6,7li + 208pb elastic scattering near the coulomb barrier. Nucl. Phys. A **571**(2), 326–336 (1994). https://doi.org/10.1016/0375-9474(94)90064-7
52. Z. Chun-Lei, Z. Huan-Qiao, L. Cheng-Jian, R. Ming, L. Zu-Hua, Y. Feng, W. Xiu-Kun, Z. Ping, A. Guang-Peng, J. Hui-Ming, W. Zhen-Dong, X. Xin-Xing, B. Chun-Lin, Unusual threshold anomaly in the 6li+208pb system. Chin. Phys. Lett. **23**(5), 1146 (2006). https://doi.org/10.1088/0256-307X/23/5/023
53. I. Martel, J. Gómez-Camacho, C.O. Blyth, N.M. Clarke, P.R. Dee, B.R. Fulton, J.A.R. Griffith, S.J. Hall, N. Keeley, G. Tungate, N.J.

Davis, K. Rusek, K.A. Connell, J.S. Lilley, M.W. Bailey, Study of the threshold anomaly in the scattering of polarized 7li from 208pb. Nucl. Phys. A **582**(1), 357–368 (1995). https://doi.org/10.1016/0375-9474(94)00492-6

54. E. Vardaci, P.K. Rath, M. Mazzocco, A. Di Nitto, G. La Rana, C. Parascandolo, D. Pierroutsakou, M. Romoli, A. Boiano, A. Vanzanella, M. Cinausero, G. Prete, N. Gelli, F. Lucarelli, C. Mazzocchi, M. La Commara, L. Fortunato, A. Guglielmetti, F. Soramel, L. Stroe, C. Signorini, Study of the threshold anomaly effect in the reaction ^{7}li+^{208}pb at energies around the coulomb barrier. The European Physical Journal A **57**, 95 (2021). https://doi.org/10.1140/epja/s10050-021-00400-3
55. H. Utsunomiya, Y.-W. Lui, L. Cooke, H. Dejbakhsh, D.R. Haenni, P. Heimberg, A. Ray, B.K. Srivastava, R.P. Schmitt, T. Udagawa, Continuous distribution of α-t relative kinetic energies in 7li breakup reactions. Nucl. Phys. A **511**(2), 379–406 (1990). https://doi.org/10.1016/0375-9474(90)90165-I
56. D. Gupta, C. Samanta, A. Chatterjee, S. Kailas, B.J. Roy, K. Mahata, A. Shrivastava, Measurement of 42 mev 7li projectile breakup on 208pb target near grazing incidence. Nucl. Phys. A **683**(1), 3–20 (2001). https://doi.org/10.1016/S0375-9474(00)00452-8
57. V.V. Parkar, V. Jha, B.J. Roy, S. Santra, K. Ramachandran, A. Shrivastava, A. Chatterjee, S.R. Jain, A.K. Jain, S. Kailas, Dipole polarizability of ^{7}Li from precision measurement of the elastic scattering on ^{208}Pb below the coulomb barrier. Phys. Rev. C **78**, 021601 (2008). https://doi.org/10.1103/PhysRevC.78.021601
58. L. Yang, C.J. Lin, H.M. Jia, F. Yang, Z.D. Wu, X.X. Xu, H.Q. Zhang, Z.H. Liu, P.F. Bao, L.J. Sun, N.R. Ma, Optical model potentials for the ^{6}He+^{209}bi reaction from a ^{208}Pb(^{7}Li,^{6}He)^{209}Bi reaction analysis. Phys. Rev. C **89**, 044615 (2014). https://doi.org/10.1103/PhysRevC.89.044615
59. A.F. Zeller, D.C. Weisser, T.R. Ophel, D.F. Hebbard, The 208Pb(7Li, 6He)209Bi reaction at 52 MeV. Nucl. Phys. A **332**(3), 515–524 (1979). https://doi.org/10.1016/0375-9474(79)90016-2
60. J.J. Kolata, V.Z. Goldberg, L.O. Lamm, M.G. Marino, C.J. O'Keeffe, G. Rogachev, E.F. Aguilera, H. García-Martínez, E. Martinez-Quiroz, P. Rosales, F.D. Becchetti, T.W. O'Donnell, D.A. Roberts, J.A. Brown, P.A. DeYoung, J.D. Hinnefeld, S.A. Shaheen, Elastic scattering and transfer in the ^{8}Li+^{208}Pb system near the coulomb barrier. Phys. Rev. C **65**, 054616 (2002). https://doi.org/10.1103/PhysRevC.65.054616
61. M. Cubero, J.P. Fernández-García, M. Rodríguez-Gallardo, L. Acosta, M. Alcorta, M.A.G. Alvarez, M.J.G. Borge, L. Buchmann, C.A. Diget, H.A. Falou, B.R. Fulton, H.O.U. Fynbo, D. Galaviz, J. Gómez-Camacho, R. Kanungo, J.A. Lay, M. Madurga, I. Martel, A.M. Moro, I. Mukha, T. Nilsson, A.M. Sánchez-Benítez, A. Shotter, O. Tengblad, P. Walden, Do halo nuclei follow rutherford elastic scattering at energies below the barrier? the case of ^{11}Li. Phys. Rev. Lett. **109**, 262701 (2012). https://doi.org/10.1103/PhysRevLett.109.262701
62. M. Cubero, J.P. Fernández-Garcia, J.A. Lay, L. Acosta, M. Alcorta, M. Madurga, M.A.G. Alvarez, M.J.G. Borge, L. Buchmann, C.A. Diget, B. Fulton, H.O.U. Fynbo, D. Galaviz, J. Gómez-Camacho, I. Martel, A. Moro, I. Mukha, T. Nilsson, A.M. Sánchez-Benítez, A. Shotter, O. Tengblad, P. Walden, Scattering of 9li on 208pb at energies around the coulomb barrier. EPJ Web of Conferences **17**, 16002 (2011). https://doi.org/10.1051/epjconf/20111716002
63. N.K. Skobelev, S.M. Lukyanov, Y.E. Penionzhkevich, S.P. Tretyakova, C. Borcea, V.E. Zhuchko, V.A. Gorshkov, K.O. Terenetsky, V.P. Verbitsky, Y.A. Pozdnyakov, Elastic scattering of 86 MeV ^{9}Li and 55 MeV ^{6}He on ^{208}Pb. Z. Phys. A. **341**, 315–318 (1992). https://doi.org/10.1007/BF01283540
64. M. Mazzocco, N. Keeley, A. Boiano, C. Boiano, M. La Commara, C. Manea, C. Parascandolo, D. Pierroutsakou, C. Signorini, E. Strano, D. Torresi, H. Yamaguchi, D. Kahl, L. Acosta, P. Di Meo, J.P. Fernandez-Garcia, T. Glodariu, J. Grebosz, A. Guglielmetti, Y. Hirayama, N. Imai, H. Ishiyama, N. Iwasa, S.C. Jeong, H.M. Jia, Y.H. Kim, S. Kimura, S. Kubono, G. La Rana, C.J. Lin, P. Lotti, G. Marquínez-Durán, I. Martel, H. Miyatake, M. Mukai, T. Nakao, M. Nicoletto, A. Pakou, K. Rusek, Y. Sakaguchi, A.M. Sánchez-Benítez, T. Sava, O. Sgouros, V. Soukeras, F. Soramel, E. Stiliaris, L. Stroe, T. Teranishi, N. Toniolo, Y. Wakabayashi, Y.X. Watanabe, L. Yang, Y.Y. Yang, H.Q. Zhang, Elastic scattering for the ^{8}B and ^{7}Be+^{208}Pb systems at near-coulomb barrier energies. Phys. Rev. C **100**, 024602 (2019). https://doi.org/10.1103/PhysRevC.100.024602
65. R.J. Woolliscroft, B.R. Fulton, R.L. Cowin, M. Dasgupta, D.J. Hinde, C.R. Morton, A.C. Berriman, Elastic scattering and fusion of ^{9}Be+^{208}Pb: Density function dependence of the double folding renormalization. Phys. Rev. C **69**, 044612 (2004). https://doi.org/10.1103/PhysRevC.69.044612
66. N. Yu, H.Q. Zhang, H.M. Jia, S.T. Zhang, M. Ruan, F. Yang, Z.D. Wu, X.X. Xu, C.L. Bai, Unusual potential behavior for the weakly bound nucleus 9be in elastic scattering from 208pb and 209bi near the threshold. J. Phys. G: Nucl. Part. Phys. **37**(7), 075108 (2010). https://doi.org/10.1088/0954-3899/37/7/075108
67. F.F. Duan, Y.Y. Yang, K. Wang, A.M. Moro, V. Guimarães, D.Y. Pang, J.S. Wang, Z.Y. Sun, J. Lei, A. Di Pietro, X. Liu, G. Yang, J.B. Ma, P. Ma, S.W. Xu, Z. Bai, X.X. Sun, Q. Hu, J.L. Lou, X.X. Xu, H.X. Li, S.Y. Jin, H.J. Ong, Q. Liu, J.S. Yao, H.K. Qi, C.J. Lin, H.M. Jia, N.R. Ma, L.J. Sun, D.X. Wang, Y.H. Zhang, X.H. Zhou, Z.G. Hu, H.S. Xu, Scattering of the halo nucleus 11Be from a lead target at 3.5 times the Coulomb barrier energy. Phys. Lett. B **811**, 135942 (2020). https://doi.org/10.1016/j.physletb.2020.135942
68. K. Palli, J. Casal, A. Pakou, Coherent description of elastic scattering and fusion at near-barrier energies for the ^{9}Be+^{208}Pb and ^{9}Be+^{197}Au reactions. Phys. Rev. C **105**, 064609 (2022). https://doi.org/10.1103/PhysRevC.105.064609
69. Y.Y. Yang, X. Liu, D.Y. Pang, D. Patel, R.F. Chen, J.S. Wang, P. Ma, J.B. Ma, S.L. Jin, Z. Bai, V. Guimarães, Q. Wang, W.H. Ma, F.F. Duan, Z.H. Gao, Y.C. Yu, Z.Y. Sun, Z.G. Hu, S.W. Xu, S.T. Wang, D. Yan, Y. Zhou, Y.H. Zhang, X.H. Zhou, H.S. Xu, G.Q. Xiao, W.L. Zhan, Elastic scattering of the proton drip line nuclei ^{7}Be,^{8}B, and ^{9}C on a lead target at energies around three times the coulomb barriers. Phys. Rev. C **98**, 044608 (2018). https://doi.org/10.1103/PhysRevC.98.044608
70. J.S. Wang, Y.Y. Yang, Q. Wang, L. Jin, J.B. Ma, M.R. Huang, J.L. Han, P. Ma, S.L. Jin, Z. Bai, Q. Hu, J.B. Chen, R. Wada, Z.Y. Sun, R.F. Chen, X.Y. Zhang, Z.G. Hu, X.H. Yuan, X.G. Cao, Z.G. Xu, S.W. Xu, C. Zhen, Z.Q. Chen, Z. Chen, S.Z. Chen, C.M. Du, L.M. Duan, F. Fu, B.X. Gou, J. Hu, J.J. He, X.G. Lei, S.L. Li, Y. Li, Q.Y. Lin, L.X. Liu, F.D. Shi, S.W. Tang, G. Xu, L.Y. Zhang, X.H. Zhang, W. Zhang, M.H. Zhao, Y.H. Zhang, H.S. Xu, G.Q. Xiao, S. Mukhejee, N. Keeley, K. Rusek, D.Y. Pang, 7be, 8b+208pb elastic scattering at above-barrier energies. J. Phys: Conf. Ser. **420**(1), 012075 (2013). https://doi.org/10.1088/1742-6596/420/1/012075
71. A. Di Pietro, G. Randisi, V. Scuderi, L. Acosta, F. Amorini, M.J.G. Borge, P. Figuera, M. Fisichella, L.M. Fraile, J. Gomez-Camacho, H. Jeppesen, M. Lattuada, I. Martel, M. Milin, A. Musumarra, M. Papa, M.G. Pellegriti, F. Perez-Bernal, R. Raabe, F. Rizzo, D. Santonocito, G. Scalia, O. Tengblad, D. Torresi, A.M. Vidal, D. Voulot, F. Wenander, M. Zadro, Elastic scattering and reaction mechanisms of the halo nucleus ^{11}Be around the coulomb barrier. Phys. Rev. Lett. **105**, 022701 (2010). https://doi.org/10.1103/PhysRevLett.105.022701
72. M. Fukuda, T. Ichihara, N. Inabe, T. Kubo, H. Kumagai, T. Nakagawa, Y. Yano, I. Tanihata, M. Adachi, K. Asahi, M. Kouguchi, M. Ishihara, H. Sagawa, S. Shimoura, Neutron halo in 11be studied

via reaction cross sections. Phys. Lett. B **268**(3), 339–344 (1991). https://doi.org/10.1016/0370-2693(91)91587-L
73. K. Wang, Y.Y. Yang, J. Lei, A.M. Moro, V. Guimarães, J.G. Li, F.F. Duan, Z.Y. Sun, G. Yang, D.Y. Pang, S.W. Xu, J.B. Ma, P. Ma, Z. Bai, Q. Liu, J.L. Lou, H.J. Ong, B.F. Lv, S. Guo, M.K. Raju, X.H. Wang, R.H. Li, X.X. Xu, Z.Z. Ren, Y.H. Zhang, X.H. Zhou, Z.G. Hu, H.S. Xu, Elastic scattering and breakup reactions of the mirror nuclei ^{12}B and ^{12}N on ^{208}Pb using ab initio structure inputs. Phys. Rev. C **109**, 014624 (2024). https://doi.org/10.1103/PhysRevC.109.014624
74. K. Wang, Y.Y. Yang, A.M. Moro, V. Guimarães, J. Lei, D.Y. Pang, F.F. Duan, J.L. Lou, J.C. Zamora, J.S. Wang, Z.Y. Sun, H.J. Ong, X. Liu, S.W. Xu, J.B. Ma, P. Ma, Z. Bai, Q. Hu, X.X. Xu, Z.H. Gao, G. Yang, S.Y. Jin, Y.H. Zhang, X.H. Zhou, Z.G. Hu, H.S. Xu, Elastic scattering and breakup reactions of the proton dripline nucleus ^{8}B on ^{208}Pb at 238 mev. Phys. Rev. C **103**, 024606 (2021). https://doi.org/10.1103/PhysRevC.103.024606
75. K. Palli, A. Pakou, P.D. O'Malley, L. Acosta, A.M. Sánchez-Benítez, G. Souliotis, A.M. Moro, E.F. Aguilera, E. Andrade, D. Godos, O. Sgouros, V. Soukeras, C. Agodi, T.L. Bailey, D.W. Bardayan, C. Boomershine, M. Brodeur, F. Cappuzzello, S. Carmichael, M. Cavallaro, S. Dede, J.A. Dueñas, J. Henning, K. Lee, W.S. Porter, F. Rivero, W. Seeger, Elastic scattering of ^{8}B+^{nat}Zr at the sub-barrier energy of 26.5 mev. Phys. Rev. C **109**, 064614 (2024) https://doi.org/10.1103/PhysRevC.109.064614
76. P.K. Sahu, A. Saxena, R.K. Choudhury, B.K. Nayak, D.C. Biswas, L.M. Pant, R.G. Thomas, Y.S. Sawant, Investigation of target shell effect in heavy ion induced transfer reactions in ^{11}B+^{208}Pb and ^{11}B+^{209}Bi reactions. Phys. Rev. C **68**, 054612 (2003). https://doi.org/10.1103/PhysRevC.68.054612
77. J.L.C. Ford, K.S. Toth, G.R. Satchler, D.C. Hensley, L.W. Owen, R.M. DeVries, R.M. Gaedke, P.J. Riley, S.T. Thornton, Single-nucleon transfer reactions induced by ^{11}B ions on ^{208}Pb: A test of the distorted-wave born approximation. Phys. Rev. C **10**, 1429–1450 (1974). https://doi.org/10.1103/PhysRevC.10.1429
78. R. Linares, M. Sinha, E.N. Cardozo, V. Guimarães, G.V. Rogachev, J. Hooker, E. Koshchiy, T. Ahn, C. Hunt, H. Jayatissa, S. Upadhyayula, B. Roeder, A. Saastomoinen, J. Lubian, M. Rodríguez-Gallardo, J. Casal, K.C.C. Pires, M. ao, Y. Penionzhkevich, S. Lukyanov, Elastic scattering measurements for the ^{10}C+^{208}Pb system at $E_{\rm lab}$ = 66 mev. Phys. Rev. C **103**, 044613 (2021). https://doi.org/10.1103/PhysRevC.103.044613
79. Y.Y. Yang, J.S. Wang, Q. Wang, D.Y. Pang, J.B. Ma, M.R. Huang, P. Ma, S.L. Jin, J.L. Han, Z. Bai, L. Jin, J.B. Chen, Q. Hu, R. Wada, S. Mukherjee, Z.Y. Sun, R.F. Chen, X.Y. Zhang, Z.G. Hu, X.H. Yuan, S.W. Xu, S.Z. Chen, X.G. Lei, L.X. Liu, W.H. Ma, S.T. Wang, D. Yan, X.H. Zhang, M.H. Zhao, Y. Zhou, Y.J. Zhou, Z.Y. Guo, Y.H. Zhang, H.S. Xu, G.Q. Xiao, Quasi-elastic scattering of ^{10,11}C and ^{10}B from a ^{nat}Pb target. Phys. Rev. C **90**, 014606 (2014). https://doi.org/10.1103/PhysRevC.90.014606
80. S. Santra, P. Singh, S. Kailas, A. Chatterjee, A. Shrivastava, K. Mahata, Coupled reaction channel analysis of elastic, inelastic, transfer, and fusion cross sections for ^{12}C+^{208}Pb. Phys. Rev. C **64**, 024602 (2001). https://doi.org/10.1103/PhysRevC.64.024602
81. A.M. Friedman, R.H. Siemssen, J.G. Cuninghame, Measurements of nuclear radii by heavy-ion scattering. Phys. Rev. C **6**, 2219–2223 (1972). https://doi.org/10.1103/PhysRevC.6.2219
82. J.B. Ball, C.B. Fulmer, E.E. Gross, M.L. Halbert, D.C. Hensley, C.A. Ludemann, M.J. Saltmarsh, G.R. Satchler, Heavy ion elastic scattering survey: (i). 208pb target. Nucl. Phys. A **252**(1), 208–236 (1975). https://doi.org/10.1016/0375-9474(75)90613-2
83. L.R. Gasques, L.C. Chamon, C.P. Silva, D. Pereira, M.A.G. Alvarez, E.S. Rossi, V.P. Likhachev, B.V. Carlson, C. De Conti, Determination of the ^{12}C nuclear density through heavy-ion elastic scattering experiments. Phys. Rev. C **65**, 044314 (2002). https://doi.org/10.1103/PhysRevC.65.044314
84. V.P. Rudakov, K.P. Artemov, Y.A. Glukhov, S.A. Goncharov, A.S. Demyanova, A.A. Ogloblin, V.V. Paramonov, R. M.V., Elastic 12C+208Pb and 16O+208Pb scattering and the form of the potential barrier. Bull.Russian Academy of Sciences - Physics **65**, 57 (2001)
85. J.S. Larsen, J.L.C. Ford, R.M. Gaedke, K.S. Toth, J.B. Ball, R.L. Hahn, Investigation of the 208Pb(12C, 11B)209Bi and 208Pb(12C, 13C)207Pb reactions at high bombarding energies. Phys. Lett. B **42**(2), 205–207 (1972). https://doi.org/10.1016/0370-2693(72)90061-5
86. D.D. Kerlee, H.L. Reynolds, E. Goldberg, Elastic scattering of heavy ions by pb^{206}, pb^{207}, and pb^{208}. Phys. Rev. **127**, 1224–1229 (1962). https://doi.org/10.1103/PhysRev.127.1224
87. S.D. Baker, J.A. McIntyre, Elastic scattering of ^{12}C, ^{14}N, and ^{16}O by ^{208}Pb and of ^{16}O by ^{209}Bi. Phys. Rev. **161**, 1200–1207 (1967). https://doi.org/10.1103/PhysRev.161.1200
88. M.A. Franey, J.S. Lilley, W.R. Phillips, Sub-Coulomb transfer reactions on 208Pb with carbon and oxygen projectiles. Nucl. Phys. A **324**(1), 193–220 (1979). https://doi.org/10.1016/0375-9474(79)90088-5
89. J.D. Ovejas, A. Knyazev, I. Martel, O. Tengblad, M.J.G. Borge, J. Cederkall, N. Keeley, K. Rusek, C. García-Ramos, T. Pérez, L.A. Acosta, A.A. Arokiaraj, M. Babo, T. Cap, N. Ceylan, G.D. Angelis, A.D. Pietro, J.P. Fernández, P. Figuera, L. Fraile, H. Fynbo, D. Galaviz, J.H. Jensen, B. Jonson, R. Kotak, T. Kurtukian, M. Madurga, G. Marquínez-Durán, M. Munch, A.K. Orduz, R. Honório, A. Pakou, L. Peralta, A. Perea, R. Raabe, M. Renaud, K. Riisager, A.M. Sánchez-Benítez, J. Sánchez-Segovia, O. Sgouros, V. Soukeras, P. Teubig, S. Viñals, M. Wolinska-Cichocka, R. Wolski, J. Yang, Study of the scattering of 15c at energies around the coulomb barrier. J. Phys: Conf. Ser. **1643**(1), 012095 (2020). https://doi.org/10.1088/1742-6596/1643/1/012095
90. F. Videbæk, R.B. Goldstein, L. Grodzins, S.G. Steadman, T.A. Belote, J.D. Garrett, Elastic scattering, transfer reactions, and fission induced by ^{16}O ions on ^{181}Ta and ^{208}Pb. Phys. Rev. C **15**, 954–971 (1977). https://doi.org/10.1103/PhysRevC.15.954
91. S.C. Pieper, M.H. Macfarlane, D.H. Gloeckner, D.G. Kovar, F.D. Becchetti, B.G. Harvey, D.L. Hendrie, H. Homeyer, J. Mahoney, F. Pühlhofer, W. Oertzen, M.S. Zisman, Energy dependence of elastic scattering and one-nucleon transfer reactions induced by ^{16}O on ^{208}Pb. Phys. Rev. C **18**, 180–204 (1978). https://doi.org/10.1103/PhysRevC.18.180
92. F.D. Becchetti, D.G. Kovar, B.G. Harvey, J. Mahoney, B. Mayer, F.G. Pühlhofer, Inelastic scattering of ^{16}O from ^{208}Pb. Phys. Rev. C **6**, 2215–2218 (1972). https://doi.org/10.1103/PhysRevC.6.2215
93. D. Torresi, E. Strano, M. Mazzocco, A. Boiano, C. Boiano, P. Di Meo, M. La Commara, C. Manea, M. Nicoletto, J. Grebosz, A. Guglielmetti, P. Molini, C. Parascandolo, D. Pierroutsakou, C. Signorini, F. Soramel, N. Toniolo, D. Filipescu, A. Gheorghe, T. Glodariu, S. Jeong, Y.H. Kim, J.A. Lay, H. Miyatake, A. Pakou, O. Sgouros, V. Soukeras, L. Stroe, A. Vitturi, Y. Watanabe, K. Zerva, Elastic scattering of 17o+208pb at energies near the coulomb barrier. EPJ Web of Conferences **117**, 08027 (2016). https://doi.org/10.1051/epjconf/201611708027
94. E.E. Gross, J.R. Beene, K.A. Erb, M.P. Fewell, D. Shapira, M.J. Rhoades-Brown, G.R. Satchler, C.E. Thorn, Elastic and inelastic scattering of 120 mev 18o from 208pb and the spin alignment of the 2+ state of 18o. Nucl. Phys. A **401**(2), 362–396 (1983). https://doi.org/10.1016/0375-9474(83)90533-X
95. M. Aygun, O. Kocadag, Y.C. Sahin, Phenomenological and microscopic model analysis of elastic scattering reactions of 18O by 24Mg, 28Si, 58Ni, 64Zn, 90Zr, 120Sn, and 208Pb target nuclei. Revista mexicana de física **61**(6), 414–420 (2015)
96. R. Morlock, R. Kunz, A. Mayer, M. Jaeger, A. Müller, J.W. Hammer, P. Mohr, H. Oberhummer, G. Staudt, V. Kölle, Halo proper-

ties of the first $1/2^+$ state in ^{17}f from the $^{16}o(p,\gamma)^{17}f$ reaction. Phys. Rev. Lett. **79**, 3837–3840 (1997). https://doi.org/10.1103/PhysRevLett.79.3837
97. C. Signorini, D. Pierroutsakou, B. Martin, M. Mazzocco, T. Glodariu, R. Bonetti, A. Guglielmetti, M. La Commara, M. Romoli, M. Sandoli, E. Vardaci, H. Esbensen, F. Farinon, P. Molini, C. Parascandolo, F. Soramel, S. Sidortchuk, L. Stroe, Interaction of ^{17}f with a ^{208}pb target below the coulomb barrier. The European Physical Journal A **44**, 63–69 (2010). https://doi.org/10.1140/epja/i2010-10934-x
98. M. Romoli, E. Vardaci, M. Di Pietro, A. De Francesco, A. De Rosa, G. Inglima, M. La Commara, B. Martin, D. Pierroutsakou, M. Sandoli, M. Mazzocco, T. Glodariu, P. Scopel, C. Signorini, R. Bonetti, A. Guglielmetti, F. Soramel, L. Stroe, J. Greene, A. Heinz, D. Henderson, C.L. Jiang, E.F. Moore, R.C. Pardo, K.E. Rehm, A. Wuosmaa, J.F. Liang, Measurements of ^{17}F scattering by ^{208}Pb with a new type of large solid angle detector array. Phys. Rev. C **69**, 064614 (2004). https://doi.org/10.1103/PhysRevC.69.064614
99. J.F. Liang, J.R. Beene, A. Galindo-Uribarri, J. Campo, C.J. Gross, P.A. Hausladen, P.E. Mueller, D. Shapira, D.W. Stracener, R.L. Varner, J.D. Bierman, H. Esbensen, Y. Larochelle, Breakup of ^{17}F on ^{208}Pb near the coulomb barrier. Phys. Rev. C **67**, 044603 (2003). https://doi.org/10.1103/PhysRevC.67.044603
100. J.F. Liang, J.R. Beene, H. Esbensen, A. Galindo-Uribarri, J. Campo, C.J. Gross, M.L. Halbert, P.E. Mueller, D. Shapira, D.W. Stracener, I.J. Thompson, R.L. Varner, Elastic scattering and breakup of ^{17}F at 10 mev/nucleon. Phys. Rev. C **65**, 051603 (2002). https://doi.org/10.1103/PhysRevC.65.051603
101. C.H. Rong, J. Rangel, Y.S. Wu, G.L. Zhang, G.X. Zhang, C.J. Lin, E.N. Cardozo, X.Y. Wang, L. Yang, N.R. Ma, D.X. Wang, L.J. Sun, H.M. Jia, F. Yang, J.S. Wang, Y.Y. Yang, J.B. Ma, P. Ma, Z. Bai, S.W. Xu, F.F. Duan, X.B. Qin, H.M. Zhao, J. Lubian, Study of quasi-elastic scattering of ^{17}f+^{208}pb at energies around coulomb barrier. The European Physical Journal A **57**, 143 (2021). https://doi.org/10.1140/epja/s10050-021-00454-3
102. K. Heo, M.-K. Cheoun, K.-S. Choi, K.S. Kim, W.Y. So, Coulomb breakup reaction of loosely bound ^{17}F with dynamic polarization potentials. Phys. Rev. C **105**, 014601 (2022). https://doi.org/10.1103/PhysRevC.105.014601
103. C.J. Lin, J.C. Xu, H.Q. Zhang, Z.H. Liu, F. Yang, L.X. Lu, Threshold anomaly in the ^{19}F+^{208}Pb system. Phys. Rev. C **63**, 064606 (2001). https://doi.org/10.1103/PhysRevC.63.064606
104. M. Aygun, A Comprehensive Description of ^{19}F Elastic Scattering by ^{12}C, ^{16}O, ^{66}Zn, ^{159}Tb, and ^{208}Pb Target Nuclei. Braz. J. Phys. **49**, 760–771 (2019)
105. M. El-Hammamy, N. El-Nohy, M.E.-A. Farid, S. Diab, M.M. El-Sayed, Systematic analysis of 17,19f and 16,17o elastic scattering on 208pb just below the coulomb barrier. Chin. J. Phys. **73**, 136–146 (2021). https://doi.org/10.1016/j.cjph.2021.03.027
106. J.D. Ovejas, I. Martel, D. Dell'Aquila, L. Acosta, J.L. Aguado, G. de Angelis, M.J.G. Borge, J.A. Briz, A. Chbihi, G. Colucci, C. Díaz-Martín, P. Figuera, D. Galaviz, C. García-Ramos, J.A. Gómez-Galán, C.A. Gonzales, N. Goyal, N. Keeley, K.W. Kemper, T. Kurtukian Nieto, D.J. Malenica, M. Mazzocco, D. Nurkić, A.K. Orduz, A. Ortiz, L. Palada, C. Parascandolo, A. Di Pietro, A.M. Rodriguez, K. Rusek, F. Salguero, A.M. Sánchez-Benítez, M. Sánchez-Raya, J. Sánchez-Segovia, N. Soić, F. Soramel, M. Stanoiu, O. Tengblad, N. Vukman, M. Xarepe, Suppression of coulomb-nuclear interference in the near-barrier elastic scattering of 17ne from 208pb. Phys. Lett. B **843**, 138007 (2023). https://doi.org/10.1016/j.physletb.2023.138007
107. R. Tripathi, K. Sudarshan, A. Goswami, P.K. Pujari, B.S. Tomar, S.B. Manohar, Charge, mass, and angular distributions in ^{20}Ne induced fission of ^{208}Pb. Phys. Rev. C **69**, 024613 (2004). https://doi.org/10.1103/PhysRevC.69.024613
108. K. Heo, M.-K. Cheoun, K.-S. Choi, K.S. Kim, W.Y. So, Suppression of the elastic scattering cross section for the ^{17}Ne+^{208}Pb system. Phys. Rev. C **109**, 024603 (2024). https://doi.org/10.1103/PhysRevC.109.024603
109. E.E. Gross, T.P. Cleary, J.L.C. Ford, D.C. Hensley, K.S. Toth, ^{20}Ne nuclear moments from ^{20}Ne(131 mev) + ^{208}Pb scattering. Phys. Rev. C **17**, 1665–1671 (1978). https://doi.org/10.1103/PhysRevC.17.1665
110. I. Strojek, W. Czarnacki, W. Gawlikowicz, N. Keeley, M. Kisielinski, S. Kliczewski, A. Kordyasz, E. Koshchiy, M. Kowalczyk, E. Piasecki, A. Piorkowska, K. Rusek, R. Siudak, A. Staudt, A. Trzcinska, Structure Effects in ^{20}Ne + ^{208}Pb Quasi-elastic Scattering. Acta Phys. Pol., B **43**, 339–344 (2012)
111. E.E. Gross, T.P. Cleary, J.L.C. Ford, D.C. Hensley, K.S. Toth, F.T. Baker, A. Scott, C.R. Bingham, J.A. Vrba, Nuclear moments of the first excited state of ^{22}Ne from ^{22}Ne(132 mev) + ^{208}Pb scattering. Phys. Rev. C **29**, 459–463 (1984). https://doi.org/10.1103/PhysRevC.29.459
112. S. Bottoni, G. Benzoni, S. Leoni, D. Montanari, A. Bracco, F. Azaiez, S. Franchoo, I. Stefan, N. Blasi, F. Camera, F.C.L. Crespi, A. Corsi, B. Million, R. Nicolini, E. Vigezzi, O. Wieland, F. Zocca, L. Corradi, G. De Angelis, E. Fioretto, B. Guiot, N. Marginean, D.R. Napoli, R. Orlandi, E. Sahin, A.M. Stefanini, J.J. Valiente-Dobon, S. Aydin, D. Bazzacco, E. Farnea, S. Lenzi, S. Lunardi, P. Mason, D. Mengoni, G. Montagnoli, F. Recchia, C. Ur, F. Scarlassara, A. Gadea, A. Maj, J. Wrzesinski, K. Zuber, Z. Dombradi, S. Szilner, A. Saltarelli, G. Pollarolo, Reaction dynamics and nuclear structure of moderately neutron-rich ne isotopes by heavy-ion reactions. Phys. Rev. C **85**, 064621 (2012). https://doi.org/10.1103/PhysRevC.85.064621
113. G. Benzoni, F. Azaiez, G.I. Stefan, S. Franchoo, S. Battacharyya, R. Borcea, A. Bracco, L. Corradi, D. Curien, G. De France, Z. Dombradi, E. Fioretto, S. Grevy, F. Ibrahim, S. Leoni, D. Montanari, G. Mukherjee, G. Pollarolo, N. Redon, P.H. Regan, C. Schmitt, G. Sletten, D. Sohler, M. Stanoiu, S. Szilner, D. Verney, Study of collisions of the radioactive ^{24}Ne beam at 7.9 MeV/u on 208Pb. The European Physical Journal A **45**, 287–292 (2010). https://doi.org/10.1140/epja/i2010-11011-4
114. Y.T. Oganessian, Y.E. Penionzhkevich, V.I. Man'ko, V.N. Polyansky, Elastic scattering of 40ca and 48ca by 208pb nuclei. Nucl. Phys. A **303**(1), 259–264 (1978). https://doi.org/10.1016/0375-9474(78)90054-4
115. S. Szilner, L. Corradi, G. Pollarolo, S. Beghini, B.R. Behera, E. Fioretto, A. Gadea, F. Haas, A. Latina, G. Montagnoli, F. Scarlassara, A.M. Stefanini, M. Trotta, A.M. Vinodkumar, Y. Wu, Multinucleon transfer processes in ^{40}Ca+^{208}Pb. Phys. Rev. C **71**, 044610 (2005). https://doi.org/10.1103/PhysRevC.71.044610
116. J.C. Zamora, V. Guimarães, A. Barioni, A. Lépine-Szily, R. Lichtenthäler, P.N. Faria, D.R. Mendes, L.R. Gasques, J.M.B. Shorto, V. Scarduelli, K.C.C. Pires, V. Morcelle, E. Leistenschneider, R.P. Condori, V.A. Zagatto, M.C. Morais, E. Crema, ^{7,9,10}be elastic scattering and total reaction cross sections on a ^{12}c target. Phys. Rev. C **84**, 034611 (2011). https://doi.org/10.1103/PhysRevC.84.034611
117. L. Jarczyk, B. Kamys, A. Strzałkowski, A. Szczurek, M. Godlewski, J. Lang, R. Müller, J. Sromicki, p−^{11}b spectroscopic factor from the interference of potential scattering and elastic transfer at low energies. Phys. Rev. C **31**, 12–16 (1985). https://doi.org/10.1103/PhysRevC.31.12
118. R.J. Ledoux, M.J. Bechara, C.E. Ordonez, H.A. Al-Juwair, E.R. Cosman, ^{12}C+ ^{12}C elastic scattering excitation functions and phase shift analysis. Phys. Rev. C **27**, 1103–1116 (1983). https://doi.org/10.1103/PhysRevC.27.1103
119. A. Tumino, C. Spitaleri, M. La Cognata, S. Cherubini, G.L. Guardo, M. Gulino, S. Hayakawa, I. Indelicato, L. Lamia, H. Petrascu, R.G. Pizzone, S.M.R. Puglia, G.G. Rapisarda, S.

Romano, M.L. Sergi, R. Spartá, L. Trache, An increase in the 12C + 12C fusion rate from resonances at astrophysical energies. Nature **557**, 687–690 (2018). https://doi.org/10.1038/s41586-018-0149-4

120. C. Beck, A.M. Mukhamedzhanov, X. Tang, Status on 12C + 12C fusion at deep subbarrier energies: impact of resonances on astrophysical S* factors. European Physical Journal. A **56**(3) (2020) https://doi.org/10.1140/epja/s10050-020-00075-2
121. L. Morales-Gallegos, M. Aliotta, L. Gialanella, A. Best, C.G. Bruno, R. Buompane, T. Davinson, M. De Cesare, A. Di Leva, A. D'Onofrio, J.G. Duarte, L.R. Gasques, G. Imbriani, G. Porzio, D. Rapagnani, M. Romoli, F. Terrasi, Direct measurements of the ^{12}C+^{12}C reactions cross-sections towards astrophysical energies. The European Physical Journal A **60**, 11 (2024). https://doi.org/10.1140/epja/s10050-024-01233-6
122. W. Treu, H. Fröhlich, W. Galster, P. Dück, H. Voit, Total reaction cross section for ^{12}C+^{12}C in the vicinity of the coulomb barrier. Phys. Rev. C **22**, 2462–2464 (1980). https://doi.org/10.1103/PhysRevC.22.2462
123. Y. Kondō, M.E. Brandan, G.R. Satchler, Shape resonances and deep optical potentials: A mean-field description of 12c + 12c scattering at low energies. Nucl. Phys. A **637**(2), 175–200 (1998). https://doi.org/10.1016/S0375-9474(98)00212-7
124. C.E. Ordoñez, R.J. Ledoux, E.R. Cosman, Rotational band of 12C + 12C gross-structure resonances and its representation by a double-minimum optical potential. Phys. Lett. B **173**(1), 39–42 (1986). https://doi.org/10.1016/0370-2693(86)91226-8
125. J.J. Kolata, R.M. Freeman, F. Haas, B. Heusch, A. Gallmann, Reaction cross sections for ^{12}C+^{12}C. Phys. Rev. C **21**, 579–587 (1980). https://doi.org/10.1103/PhysRevC.21.579
126. Y.-L. Xu, Y.-L. Han, X.-W. Su, X.-J. Sun, H.-Y. Liang, H.-R. Guo, C.-H. Cai, Global optical model potential describing 12C-nucleus elastic scattering. Chin. Phys. C **44**(12), 124103 (2020). https://doi.org/10.1088/1674-1137/abb4d0

Peter Mohr's area of research is nuclear astrophysics. He received the doctoral degree from University Tübingen in 1995, and he finished his habilitation thesis in 2003 at Technische Universität Darmstadt. His research at Atomki, Debrecen, focuses on α- and γ-induced reactions, the corresponding (α, γ) and (γ, α) reaction rates in explosive stellar environments, and the relevance of the underlying α-nucleus potentials.